Correlations between kinematics, chemistry, and ages of stars in the solar neighbourhood as seen by the RAVE survey

Jennifer Leigh Wojno
Leibniz-Institut für Astrophysik Potsdam (AIP)

Dissertation
zur Erlangung des akademischen Grades
doctor rerum naturalium (Dr. rer. nat.)
in der Wissenschaftsdisziplin Astrophysik

Eingereicht an der Mathematisch-Naturwissenschaftlichen Fakultät
der Universität Potsdam

Potsdam, den 04. Oktober 2017

Cover: Screenshot from a movie flying through stars from RAVE DR5, colour-coded by heliocentric radial velocity. Credit: Kristin Riebe (visualisation), the RAVE Collaboration. Milky Way illustration (top view): R. Hurt (SSC), NASA/JPL-Caltech.
Back cover: A view of the Milky Way disc from Gaia DR1, with TGAS proper motions and RAVE stars overplotted. Credit: Maarten Breddels (stellar density and proper motions), Kristin Riebe (RAVE stars); the RAVE Collaboration.

Betreuer:	Dr. Georges Kordopatis/Prof. Dr. Matthias Steinmetz
1. Gutachter:	Prof. Dr. Matthias Steinmetz Leibniz-Institut für Astrophysik Potsdam (AIP) / Universität Potsdam (UP)
2. Gutachter:	Prof. Dr. Rosemary F. G. Wyse Johns Hopkins University
3. Gutachter:	Prof. Dr. Sofia Feltzing Lund Observatory

Contents

Abstract

Galactic archaeology is the study of the history of galaxies, where stars act as the fossil record. By investigating and characterizing the properties of stellar populations, galactic archaeologists seek to reconstruct a picture of the formation of galaxies and their subsequent evolution. These studies rely on two critical assumptions: first, that the atmosphere of a star is representative of the environment where it formed, and secondly, that stars born in the disc do not venture far from their birthplace. However, evidence has been found to suggest that stars can migrate radially due to interactions with the bar and spiral arms, which complicates the situation considerably.

Within the Milky Way, large-scale stellar spectroscopic surveys are a crucial tool to disentangle this complex picture. Spectra hold information about the chemical composition of stars, and in particular, the abundance of α-elements (such as oxygen, magnesium, and silicon) can also act as a proxy for age. In addition, the radial velocity of stars can be determined from their spectra. Together with data from astrometric and photometric surveys, large-scale spectroscopic surveys can determine multidimensional chemodynamical properties for large samples of disc stars.

In this work, I use samples of extended solar neighbourhood stars from the RAdial Velocity Experiment (RAVE) survey to investigate the chemodynamical history of the Milky Way disc. In paper I, "Chemical separation of disc components using RAVE", for the first time with RAVE data, disc components (the thin, or α-low disc, and the thick, or α-high disc), were identified in chemical space using a probabilistic approach. Unlike high-resolution studies, it is not possible to separate the disc components *a priori* with RAVE, as the uncertainties on the α-abundance measurements are larger than what is needed to recover the gap between the α-low and -high sequences. We find that our chemically separated components are distinct in their kinematics, in agreement with results from high-resolution studies. We conclude that our study supports the scenario that a gap in the star formation history of the disc produced the two sequences we see. In addition, we find evidence that super metal-rich stars from the inner Galaxy migrate outward, although some may just be visiting the solar neighbourhood.

In paper II, "The selection function of the RAVE survey", I led the effort to characterize the selection function of RAVE, knowledge of which is necessary to understand the relationship between the observed and underlying stellar populations, as well as identify potential biases which may affect the interpretation of RAVE for chemodynamical studies of the Milky Way. With the selection function in hand, it was possible to generate a mock-RAVE catalogue by applying the selection function to a model of the Galaxy. This mock catalog was then compared to the parent sample to identify biases resulting from the selection function of RAVE. We found no significant biases induced by the selection function of RAVE in either the velocity or metallicity distributions, verifying the robustness of RAVE for chemodynamical studies in the solar neighbourhood.

Finally, in paper III, "Correlations between age, kinematics, and chemistry as seen by the RAVE survey", a high-quality sample of stars with chemistry and radial velocities from RAVE, proper motions from UCAC5, and parallaxes from TGAS was used to explore the local velocity space as a function of metallicity and age. The sample was separated into two broad age groups: young (typically associated with the thin, α-low disc), and old (typically associated with the thick, α-high disc). Then, kinematics trends as a function of both Galactocentric radius and metallicity were investigated. Both young and old samples show signatures of a negative gradient in mean radial velocity as a function of Galactocentric radius, and show for the first time that young, metal-rich stars have the steepest negative gradient. We conclude, in agreement with previous theoretical studies, that the behavior of these trends reflects the presence of non-axisymmetries in the disc (such as the bar and the spiral arms), and are directly related to the efficiency of radial migration of stars in the disc.

Zusammenfassung

Das noch junge Feld der Galaktischen Archäologie befasst sich mit der Entstehung und Entwicklung von Galaxien. Sterne dienen ihr als Fossilien, in denen Teile der chemischen und dynamischen Geschichte einer Galaxie kodiert sind. Durch genaue Beobachtungen von stellaren Populationen erhalten galaktische Archäologen Aufschluss über die Evolution der jeweiligen Heimatgalaxie. Studien dieser Art beruhen auf zwei wichtigen Grundannahmen: erstens, dass die Atmosphäre eines Sterns die chemische Zusammensetzung seiner Entstehungsregion widerspiegelt, und zweitens, dass Sterne ihre Bewegung nach ihrer Geburt nicht drastisch ändern. In den letzten Jahren haben Beobachtungen und theoretische Arbeiten gezeigt, dass die zweite Annahme nicht streng erfüllt ist: Sterne in Galaxienscheiben können durch Interaktionen mit Spiralarmen und dem galaktischen Balken radial migrieren.

Für die Milchstraße sind insbesondere groß angelegte spektroskopische Himmelsdurchmusterungen ein probates Mittel, um das komplexe Problem der chemodynamischen Geschichte zu lösen. Ein Sternspektrum enthält reiche Informationen über die radiale Geschwindigkeit und die chemische Zusammensetzung eines Sterns, insbesondere über den relativen Gehalt an sogenannten α- Elementen (wie etwa Sauerstoff, Magnesium oder Silizium), welche zusätzlich Aufschluss über das Alter der Sterne geben können. Durch Kombination mit astrometrischen und photometrischen Durchmusterungen lassen sich multidimensionale chemodynamische Eigenschaften für große Stichproben von Sternen in der Milchstraße bestimmen.

In dieser kumulativen Arbeit untersuche ich eine Stichprobe von Sternen der erweiterten Sonnenumgebung, die mit dem RAdial Velocity Experiment (RAVE) beobachtet wurden, um die chemodynamische Geschichte der Milchstraße zu studieren. In Paper I benutze ich einen probabilistischen Ansatz, um α-arme und -reiche Sterne zu definieren und deren kinematische Eigenschaften zu studieren. Diese Studie zeigt, dass eine Lücke in der Sternentstehungsgeschichte der Milchstraße die beiden Scheibenpopulationen produziert hat. Außerdem weisen die Daten darauf hin, dass Sterne mit supersolarer Metallhäufigkeit radial in die Sonnenumgebung migriert sind.

Paper II beschäftigt sich mit der Charakterisierung der Selektionsfunktion der RAVE-Durchmusterung, die bis dahin eine essentielle Unbekannte in Vergleichen zwischen RAVE-Beobachtungen und Milchstraßenmodellen war. Durch die Anwendung der Selektionsfunktion auf ein Modell für der Milchstraßenscheibe wurde es möglich, einen Mock-RAVE-Katalog zu erstellen. Es wurden keine signifikanten systematischen Verzerrungen der Geschwindigkeits- und Metallizitätsverteilungen durch die Selektionsfunktion festgestellt, was den Wert von RAVE für chemodynamische Studien unterstreicht.

Schließlich wurde in Paper III eine hochqualitative Auswahl von Sternen mit chemischen Häufigkeiten und Radialgeschwindigkeiten von RAVE, Eigenbewegungen von UCAC5 sowie Parallaxen aus dem ersten Datenveröffentlichung von Gaia genutzt, um den lokalen Geschwindigkeitsraum als Funktion von Metallizität und Sternalter zu studieren. Dazu wurde die Stichprobe in eine junge und eine alte Population geteilt, die in etwa der klassischen dünnen, α-armen bzw. dicken α-reichen Scheibenpopulation entsprechen.

Beide Gruppen haben einen negativen Geschwindigkeitsgradienten mit wachsendem galaktozentrischem Abstand, und es konnte zum ersten Mal gezeigt werden, dass junge, metallreiche Sterne den steilsten negativen Geschwindigkeitsgradienten aufweisen. Theoretische Studien lassen den Schluss zu, dass dieses Verhalten durch den Einfluss nichtaxisymmetrischer Strukturen in der Sternenscheibe (wie etwa den galaktischen Balken und die Spiralarme) erklärt werden kann und damit eine Messung der radialen Migrationseffizienz ermöglicht.

1 Introduction

1.1 Why study disc galaxies?

Picture a galaxy in your mind. It was probably a disc galaxy[1], with a bright white-yellow central region, swirling spiral arms speckled with blue star forming regions, and thin, dark lanes of dust– an island of light in stark contrast to the dark void surrounding it. Such images of massive spiral galaxies, with their intricate complexity and beauty, are ubiquitous in modern astrophysics, and understanding their formation and evolution has persisted as a fundamental theme of the field for over a century.

Within the framework of the most widely-accepted cosmological model, dark energy (Λ) with cold dark matter (CDM), spiral galaxies like the Milky Way form hierarchically through mergers, with gravity acting as the dominant force to bring them together (for recent reviews see Springel et al. 2006; Frenk & White 2012; Peebles 2012). While this model is incredibly successful at describing the large scale structure of the Universe and the distribution of galaxies within it, predictions made from cosmological simulations in ΛCDM begin to break down at the scale of galaxies and dwarf galaxies (e.g. Bullock & Boylan-Kolchin 2017). In particular, the following discrepancies directly influence our understanding of the formation and evolution of disc galaxies:

- **The missing satellite problem** – Cosmological simulations predict two orders of magnitude more dwarf galaxies than what we observe (Kauffmann et al. 1993; Klypin et al. 1999). Around the Milky Way, thousands of dark matter subhalos are expected to exist, yet we've identified only $\sim$ 50 or so dwarf galaxies to date (e.g. Koposov et al. 2015; Drlica-Wagner et al. 2015).

- **Size and shape of galactic bulges** – In ΛCDM simulations, hierarchical clustering tends to generate disc galaxies with massive, spheroidal (classical) bulges (e.g. Abadi et al. 2003; Scannapieco et al. 2012). However, many disc

[1] If it was an elliptical or irregular galaxy, just bear with me here.

galaxies in the local Universe either lack a central spheroidal component, or their bulge is not as dense as those predicted by models (Shen et al. 2010; Kormendy et al. 2010).

- **Persistence of galactic discs** – Hierarchical structure formation relies on frequent mergers to build up galaxies from smaller components, however, simulations have shown that mergers often thicken or destroy thin, disc-like structures (e.g. Barnes 1992; Walker et al. 1996; Scannapieco et al. 2009). The majority of disc galaxies have thin structures containing old stars, indicating either that they have somehow managed to survive major mergers, or they've had a quiescent recent merger history. Both scenarios seem to be in contention with the merger approach of the ΛCDM framework.

To address these issues, and in particular the fragility of galactic discs, we have to consider two possibilities: either ΛCDM is incomplete, or our description of the other ingredient of cosmological simulations, baryonic physics, is inadequate. ΛCDM succeeds because it is the simplest, most effective theory to accurately reproduce observed large scale structure and primordial elemental abundances (Planck Collaboration et al. 2016), and so there is significant doubt that it would be fundamentally wrong (Binney 2004). However, growth via accretion and mergers is not the only model of Galaxy evolution. Eggen et al. (1962) proposed a model where galaxies form through the monolithic collapse of a large, protogalactic gas cloud. While this scenario has fallen out of favor with the rise of ΛCDM, it can still be used to explain the properties of some galactic components (e.g. the halo, Section 1.2.1.)

As a result, we turn to studies of the baryonic component of galaxies. There is significant evidence in the literature that the key to reconciling discrepancies between theory and observation lies in properly addressing both external and internal mechanisms affecting galactic evolution. Externally, such mechanisms involve ongoing and past accretion through mergers, while internal mechanisms include star formation, enrichment of the interstellar medium (ISM), supernovae feedback, stellar winds, and radial migration, to name a few (e.g., Nath & Silk 2009; Scannapieco et al. 2009; Hopkins et al. 2012; Brook et al. 2012).

There are two distinct approaches to better understanding these evolutionary processes. The first approach is to study galaxies external to our own. With this strategy, it is possible to survey and characterize the wide range of galaxy morphologies, both in the local Universe ($z \sim 0$) as well as at high redshift, especially at the peak of star formation density ($z \sim 2$, e.g. Madau & Dickinson 2014). By comparing the morphology and composition of field galaxies at different points in time, we can construct a comprehensive picture of galaxy evolution from an external perspective. In addition to these broad population studies, external galaxies offer the opportunity to study different galactic components to a greater extent (e.g., the diffuse stellar halo and the entire galactic disc), and from different perspectives (i.e., edge-on vs. face-on). However, despite these advantages, it is not possible to conduct detailed investigations of their internal evolution.

The other approach is to study the evolution and history of the Milky Way (Figure 1.1), where we can study its constituents and internal evolution in much greater detail. In particular, stellar surveys of our Galaxy are particularly valuable,

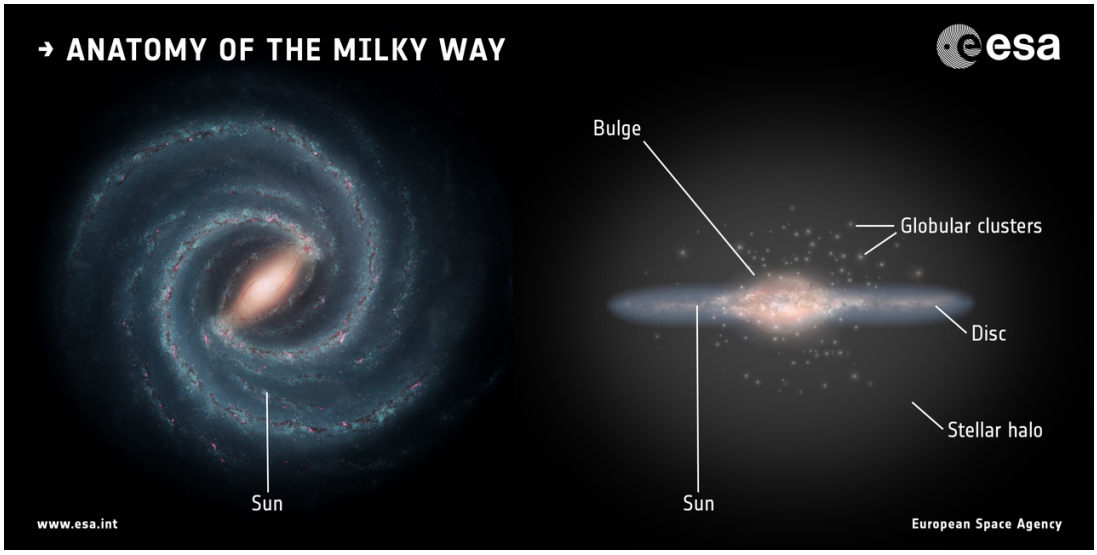

Figure 1.1 — Artist's impression of the Milky Way, a barred spiral galaxy, shown face-on (left), and edge-on (right). The face-on view shows the central bar and spiral structure of the disc and the approximate position of the Sun, about halfway between the centre and the edge of the disc. The edge-on view highlights the three main components of the Milky Way: the stellar halo, which contains globular clusters; the bar/bulge; and the disc. Credit: NASA/JPL-Caltech (left); ESA (right); ESA/ATG medialab (layout).

as stars act as an ideal means for disentangling its evolutionary history. Access to the kinematics, chemistry, and age of individual stars in the Milky Way allows for a distinct advantage over observing external systems: we can identify coeval populations, and therefore quantify the relative proportion of stars born *in situ* from gas present in the early Milky Way versus infalling gas from mergers, or born in dwarf galaxies which have since been accreted.

1.2 The Milky Way

The Milky Way is a barred spiral galaxy (Hubble type Sbc, e.g. Gerhard 2002), and is the second largest spiral galaxy in the local group after Andromeda (M31), with a stellar mass of $\sim 6 \pm 1 \times 10^{10} M_{\odot}$ (e.g. McMillan 2011; Bovy & Rix 2013; Piffl et al. 2014; Binney & Piffl 2015). Both the Milky Way and M31 have satellite galaxies gravitationally bound to them. The number of satellite galaxies associated with the Milky Way remains an open investigation, with new discoveries being made even within the past few years from deep, large-scale photometric surveys (e.g. Koposov et al. 2015; Homma et al. 2016). Some of these satellites are actively interacting with the Milky Way disc (e.g. Belokurov et al. 2006), showing that our Galaxy is still undergoing significant accretion and dynamical evolution.

In this section, we present an overview of the constituent components of the Milky Way, from the perspective of stars and the environments in which they form. From least massive to most massive in terms of baryonic content, these consist of the halo, the bulge, and the stellar disc (itself composed of a thin and thick disc).

1.2.1 The halo

The halo is the largest component of the Galaxy in terms of radial extent, although it hosts only ∼ 1% of the total stellar mass of the Galaxy ($\sim 4-7\times10^8 M_\odot$, Helmi 2008; Bell et al. 2008). It is roughly spheroidal (Jurić et al. 2008) with no net rotation (Ivezić et al. 2008), and no ongoing star formation. However, it is rich in substructure in the form of merger debris such as stellar streams, remnants of accretion events and interactions with dwarf galaxies (e.g. Helmi & White 1999; Belokurov et al. 2006; Helmi 2008; Helmi et al. 2017). Stars found in the halo are typically old ($\gtrsim$ 12 Gyr, Reid 2005; Kalirai 2012; Kilic et al. 2017), kinematically hot, metal-poor, having a metallicity distribution that peaks around ∼ −1.6 in [Fe/H][2](e.g. Ryan & Norris 1991; Carney et al. 1996; Schörck et al. 2009; Allende Prieto et al. 2014) with an extended metal-poor tail (down to [Fe/H] $\lesssim -7$, Keller et al. 2014; Bessell et al. 2015; Nordlander et al. 2017) and are typically enhanced in their α-element abundances (e.g. Wheeler et al. 1989; Nissen et al. 1994; Carretta et al. 2000).

There are two predominant scenarios that attempt to identify the mechanisms responsible for the formation of the halo. The first, presented in Eggen et al. (1962), describes the stellar halo of the Milky Way forming from the rapid, monolithic collapse of gas onto the Galactic plane. The second, by Searle & Zinn (1978), proposes that the halo was built up from numerous mergers and accretion events. This model agrees with predictions from ΛCDM, where the halo was formed hierarchically (Bullock & Johnston 2005). One of the most compelling pieces of evidence supporting this scenario came from the discovery of the Sagittarius dwarf spheroidal galaxy (Ibata et al. 1994), which is still merging with the Milky Way, wrapping around the Galaxy more than once (Chou et al. 2007). The current paradigm holds that both scenarios can be invoked to reproduce the observed properties of the stellar halo, with two overlapping components: an inner- and outer-halo (Carollo et al. 2007). The more metal-rich inner halo, which dominates at Galactocentric distances 10 < r < 15 kpc, likely formed through dissipative processes, while the outer halo, at r $\gtrsim$ 15 kpc, was built up from mergers with smaller subsystems, such as dwarf spheroidal galaxies (e.g. Carollo et al. 2007, 2010; Beers et al. 2012; Helmi et al. 2017; however, cf. Schönrich et al. 2011).

1.2.2 The bar/bulge

Central bars or bulges are a nearly ubiquitous feature of massive ($> 10^9$ $M_\odot$) galaxies in the local group (Fisher & Drory 2011). In the Milky Way, the bar/bulge is heavily obscured by dust from our perspective in the disc. While a few small low-extinction 'windows', such as Baade's Window, provide a relatively clear view for detailed studies of the bulge (Dutra et al. 2002), they are not suited for characterizing bulge demographics as a whole. As a result, much of what we know about the Milky Way bulge comes from observations of red clump giant stars (e.g. Stanek et al. 1994, 1997; Rattenbury et al. 2007; Wegg et al. 2015), which can be seen at large distances and

[2]Defined in the usual way, $[\mathrm{Fe/H}] = \log_{10}\left(\frac{N_\mathrm{Fe}}{N_\mathrm{H}}\right)_* - \log_{10}\left(\frac{N_\mathrm{Fe}}{N_\mathrm{H}}\right)_\odot$, where N_Fe and N_H are the number of iron and hydrogen atoms, respectively, $*$ indicates abundances relative to a given star, and $\odot$ indicates relative to the Sun.

through significant extinction. However, studies utilizing micro-lensing events to observe dwarfs and subgiants in the bulge are now offering supplemental evidence for the formation history and evolution of the central region of the Galaxy (e.g. Bensby et al. 2017).

Currently, there are three dominant scenarios to explain the presence of a central bar/bulge region: dissipative collapse and hierarchical clustering (Athanassoula 2005), clumpy star-forming regions in the disc migrating inward due to dynamical friction (Noguchi 1998), or disc buckling (e.g. Patsis et al. 2003). The first two scenarios produce a 'classical' or spheroidal bulge, while disc buckling produces a bar, also referred to as a 'pseudo-bulge'. Morphologically, the bulge of the Milky Way is 'boxy' or 'peanut-shaped' (e.g. Weiland et al. 1994; Dwek et al. 1995)– a natural consequence of viewing a bar edge-on (e.g. Athanassoula 2008). This bar structure rotates cylindrically as a solid body (Zhao 1996; Beaulieu et al. 2000; Kunder et al. 2012; Ness et al. 2013; Zoccali et al. 2014), with a pattern speed of $\sim 40-50$ km s^{-1}, placing its corotation radius inside the Solar Circle (e.g. Minchev & Quillen 2007; Antoja et al. 2014; Sormani et al. 2015). In addition to this rotating bar, it has been suggested that a fraction of bulge stars ($\lesssim 25\%$) belong to a classical, non-rotating spheroidal component (Shen et al. 2010; Ness et al. 2013; Kunder et al. 2016). The differences between these components, and the fact that they're both present in the bulge, indicates some combination of the formation scenarios listed above, consistent with results from cosmological simulations (Obreja et al. 2013).

Together, these two bulge components comprise $\sim 25\%$ of the baryonic mass budget of the Milky Way ($\sim 2\times10^{10}$ M$_\odot$, Zhao et al. 1994; Dwek et al. 1995; Bissantz et al. 2003; Portail et al. 2015; Valenti et al. 2016). Stars in this region are typically old ($\gtrsim 10$ Gyr, Ortolani et al. 1995; Zoccali et al. 2003), and may even be the most ancient in the Galaxy (Howes et al. 2015). They have a broad metallicity distribution ($-1 \lesssim$ [Fe/H] $\lesssim 1$, e.g. Rich 1988; Zoccali et al. 2008; Bensby et al. 2017) that varies as a function of height above the plane (e.g. Zoccali et al. 2008; Gonzalez et al. 2013).

1.2.3 The stellar disc

The disc of the Milky Way is the largest component in terms of stellar mass ($\sim 5\times10^{10}$ M$_\odot$, e.g. Flynn et al. 2006; McMillan 2011, 2017). The disc itself is comprised of two components: a thin disc and a thick disc (Gilmore & Reid 1983). Estimates of the relative mass of the thick disc to the thin disc range from $\sim 20-50\%$, depending on the tracers and definition of the two disc components (e.g. Snaith et al. 2015; Bland-Hawthorn & Gerhard 2016). The thin disc is comprised of relatively young, kinematically cold stars with a metallicity distribution ($-0.7 <$ [Fe/H] < 0.4, e.g. Navarro et al. 2011; Haywood et al. 2013) peaking around solar, and [α/Fe] $\lesssim 0.2$ (e.g. Bensby et al. 2005; Navarro et al. 2011; Lee et al. 2011). However, this metallicity distribution is not homogenous over the entire disc– it varies both as a function of radius (∂[Fe/H]$/\partial R \sim -0.06$ dex kpc^{-1}, e.g. Gazzano et al. 2013; Boeche et al. 2013; Recio-Blanco et al. 2014; Bergemann et al. 2014; Anders et al. 2014; Genovali et al. 2014), and vertical height above the plane (∂[Fe/H]$/\partial Z \sim -0.1$ dex kpc^{-1}, e.g. Schlesinger et al. 2014). As its name suggests, it is structurally thin, with a scale height of ~ 300 pc (e.g. Kent et al. 1991; Chen et al. 2001; Jurić et al. 2008), and a scale

length of 2.6 ± 0.5 kpc (e.g. Jurić et al. 2008; McMillan 2011). Most of the mass of the MW disc is contained within the thin disc, with a total stellar mass of $3.5 \pm 1 \times 10^{10} M_{\odot}$ (Bland-Hawthorn & Gerhard 2016, and references therein).

The thick disc was first detected in vertical star counts, where two exponential disc components, in addition to the halo, were needed to fit observations (Gilmore & Reid 1983). Using SDSS, Jurić et al. (2008) verified the presence of the thick disc in terms of stellar density. In contrast to the thin disc, the thick disc consists of old ($\gtrsim$ 10 Gyr, e.g. Quillen & Garnett 2001; Fuhrmann 2008) stars with larger velocity dispersions and orbital eccentricities, lagging the LSR by $\sim 50\,\mathrm{km\,s^{-1}}$ (e.g. Ojha et al. 1996; Chiba & Beers 2000; Soubiran et al. 2003; Lee et al. 2011) due to asymmetric drift. As a result, the thick disc vertically thicker (scale height $\sim$ 900 pc, e.g. Chen et al. 2001; Reylé & Robin 2001; Jurić et al. 2008; McMillan 2011). It is also less massive than the thin disc[3] with a stellar mass of ($\sim 6 \pm 3 \times 10^9 M_{\odot}$, e.g. Bland-Hawthorn & Gerhard 2016). The thick disc is more metal-poor than the thin disc, with a metallicity distribution covering a range of $-2 \lesssim$ [Fe/H] $\lesssim 0.4$ dex (e.g. Bensby et al. 2007; Kordopatis et al. 2011, 2013b) that peaks around -0.7 dex in [Fe/H] (e.g. Gilmore et al. 1995; Allende Prieto et al. 2006).

Although the two disc components overlap spatially and kinematically, they can be clearly distinguished in the [Fe/H]-[α/Fe] plane (e.g. Bensby et al. 2005; Fuhrmann 2008; Lee et al. 2011, see Section 1.3.1). The thick disc is typically associated with a metal-poor, α-enriched ([α/Fe] $\gtrsim 0.2$) sequence of stars, while the thin disc stars typically have [α/Fe] $\lesssim 0.2$. When defined using chemical criteria (metal-poor, alpha-rich), the thick disc is more centrally concentrated than the thin disc, with a scale length of $\sim$ 2.0 kpc (e.g. Reylé & Robin 2001; Jurić et al. 2008; Bensby et al. 2011; Bovy et al. 2015). With detailed chemical abundance information available via large-scale spectroscopic surveys, there has been a significant push to disentangle the assembly and star formation histories of each disc component and the relationship and interplay between them. In particular, our understanding of the the origin of the disc is still affected by significant uncertainties.

The presence of radial and vertical metallicity gradients point to a scenario where the disc formed inside out, with the inner regions forming first (e.g. Matteucci & Francois 1989; Bird et al. 2013; Gibson et al. 2013; Minchev et al. 2014a; Miranda et al. 2015; Schönrich & McMillan 2017), and upside down, as the oldest stars are found in the kinematically heated component (e.g. Bird et al. 2013; Schönrich & McMillan 2017). Regarding the origin of this old, thick disc component, formation scenarios generally fit into two broad categories: external, violent events or internal, secular mechanisms (see Ivezić et al. 2012; Feltzing & Chiba 2013, and references therein). External events include formation through monolithic collapse in a similar fashion as the halo (e.g. Eggen et al. 1962; Larson 1974), mergers and accretion of gas clouds (e.g. Brook et al. 2004, 2005) or stars (e.g. Gilmore et al. 2002; Abadi et al. 2003; Navarro et al. 2004; Meza et al. 2005) originating from satellites of the Milky Way, and dynamical heating induced by a minor merger with the early thin disc (e.g. Carney et al. 1989; Quinn et al. 1993; Brook et al. 2007; Villalobos & Helmi 2008; Di Matteo et al. 2011). Proposed internal mechanisms include disc heating via

[3] However, it has also been suggested that the thick disc is as massive as the thin disc (see e.g. Snaith et al. 2014, 2015; Pouliasis et al. 2017).

radial migration (e.g. Roškar et al. 2008; Schönrich & Binney 2009a,b; Loebman et al. 2011)[4], where stellar orbits are affected by disc asymmetries (e.g. the bar and spiral arms), or interactions with giant molecular clouds (Sellwood & Binney 2002); or via turbulent gas clumps in the early disc (Elmegreen & Elmegreen 2006; Bournaud et al. 2007, 2009; Forbes et al. 2012). It is likely that some combination of these scenarios produced the thick disc of our Galaxy, however, it is still unclear what the dominant mechanism is. To explore this open question and others, we turn to studies of trends in the kinematics, chemistry, and age of the most long-lived stars in the Galaxy– a broad field known as Galactic archaeology.

1.3 Galactic archaeology

Galactic archaeology refers to the study of the assembly history of the Milky Way, where long-lived objects (e.g. low-mass stars) act as 'fossils', or tracers, of its chemo-dynamical history. As collisionless systems, stellar streams can help reconstruct the merger history of the Milky Way (e.g. Lynden-Bell & Lynden-Bell 1995; Freeman & Bland-Hawthorn 2002; Abadi et al. 2003; Helmi 2008), and the effect of tidal forces from interactions with dwarf galaxies. Internally, characterizing the kinematics of disc stars allows for a better understanding of large scale perturbations in the disc (caused by the bar and/or spiral arms), as well as radial and vertical flows. While it is possible to identify kinematic structures in action-angle space long after they have been phase-mixed in coordinate space (e.g. McMillan & Binney 2008; Helmi et al. 2017), information can be lost due to kinematic heating processes. In addition, internal dynamical mechanisms such as radial migration (Sellwood & Binney 2002) can move stars from one circular orbit to another due to interactions with transient spiral arms, further complicating the picture.

We then consider the chemical composition of stars, which is typically a more telling indicator of their origin. As the atmospheres of low and intermediate-mass stars ($M \lesssim 1 M_{\odot}$) remain relatively stable throughout their lifetime, they are representative of the environment in which they were born (Freeman & Bland-Hawthorn 2002). In particular, the seminal work by Edvardsson et al. (1993) and many later studies (e.g. Reddy et al. 2003; Tolstoy et al. 2009; Haywood et al. 2013; Bensby et al. 2014) have demonstrated the potential of using the relative abundance of alpha elements (Section 1.3.1) to iron to differentiate stars born in regions with different star formation histories, or those originating in dwarf galaxies with those born in the Milky Way. Finally, with stellar age estimates, it is possible to follow the temporal evolution of these internal mechanisms, and trace the history of star formation in different regions of the Galaxy.

1.3.1 Tools of Galactic archaeology

In Figure 1.2, we outline the essential tools for Galactic archaeology. These tools build on each other, and include positions, distance, 3D space velocities, chemical abundance patterns, and additional astrophysical parameters (such as age), for

[4] However, cf Minchev et al. (2012, 2013).

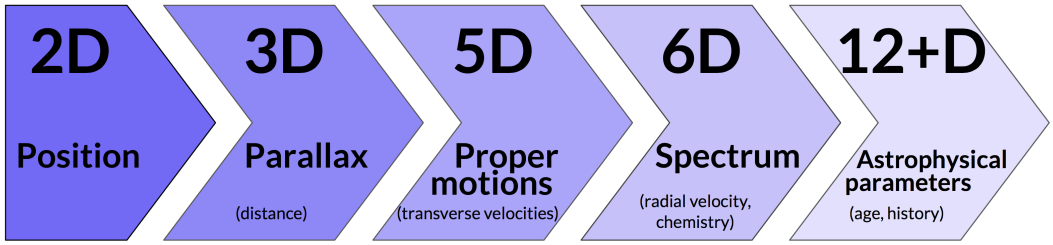

Figure 1.2 — Diagram of the tools of Galactic archaeology, and how they build on each other to provide the multi-dimensional information needed to reconstruct the formation history of the Galaxy. Adapted from Figure 2 of Gilmore et al. (2012).

large samples of stars. In the following sections, we describe what each of these tools can tell us about the history of the Milky Way, and how such data are acquired.

Position and kinematics

One of the most fundamental ways of investigating properties of the Milky Way is to count stars, and measure their relative motions on the sky. Astronomers recognized that the Milky Way contains structures typical of external spiral galaxies by quantifying the relative density of stars as a function of their position, with the main constituents being a stellar disc, comprised itself of a thin and thick disc, a central bulge, and a diffuse halo. To reconstruct the formation history of the Milky Way, it is necessary to identify ancient stars in each Galactic component, and a first approach is to do this by their position and kinematics.

Astrometric catalogues provide position, two-dimensional velocity information (proper motion, or a stars relative transverse motion on the sky), and parallax (distance) measurements. To obtain a stars 3D velocity through space, radial velocity measurements are needed in addition to proper motion and parallax. Stellar radial velocities are obtained by comparing the position of the absorption lines in a stellar spectrum to those measured on Earth, with a shift towards the red or blue indicating, respectively, that the star is moving away or towards us, with the magnitude of this velocity depending on the amount of shift. Obtaining radial velocities was the primary goal of the RAdial Velocity Experiment (RAVE, Steinmetz et al. 2006, see Section 1.3.2), which gathered spectra of approximately half a million extended solar neighbourhood stars. The second data release of Gaia, planned for April 2018, will provide radial velocities for a few million stars down to $G \sim 12$.

Full 6D (position and distance plus 3D space velocity) information for large samples of Milky Way stars allows for the characterization of a number of parameters crucial to accurately modeling the Milky Way, from the solar neighbourhood to the Galaxy as a whole. One such fundamental parameter is the position of the Sun in the plane of the Galaxy (R_0, z_0), and its orbit around the Galactic centre. Recent measurements of these values put the Sun at ~8.3 kpc from the Galactic centre (e.g.

McMillan 2011; Schönrich 2012; Reid et al. 2014), slightly above the plane of the disc ($z_0 \sim 25$ pc, Jurić et al. 2008), with a Galactocentric azimuthal velocity of ~ 240 km s^{-1} (McMillan 2011; Schönrich 2012; Reid et al. 2014), and a solar peculiar motion with respect to the local standard of rest (LSR) of $(U,V,W)_\odot = (11.10, 12.24, 7.25)$ km s^{-1} (Schönrich et al. 2010; Bovy et al. 2012a). Other important constraints to Galactic models directly related to stellar kinematics are the scale length and height of the disc, and the ratio between the thin and thick components (see Section 1.2.3). Finally, the motions of stars can be used to characterize the Milky Way's gravitational potential (e.g. Binney & Tremaine 2008; Binney 2011; Rix & Bovy 2013) and the distribution function of stellar orbits (e.g. Trick et al. 2016), which are crucial for understanding its formation history (e.g. Binney 2013; Sanders & Binney 2015).

Chemistry

To disentangle the assembly history of the Milky Way, in addition to the kinematics of stars, we need an accurate description of how the chemical composition of star-forming gas clouds changed as a function of time. A critical assumption of Galactic archaeology is that the history of star formation and infall events is encoded in the metallicity distributions of stellar populations, since different supernovae mechanisms produce different elemental abundance ratios, and the atmospheres of low-mass stars remain relatively unchanged throughout their lifetime (Freeman & Bland-Hawthorn 2002). Models of the chemical evolution of the Milky Way (e.g. Chiosi 1980; Chiappini et al. 1997; Minchev et al. 2013; Snaith et al. 2015) attempt to reproduce observations by assuming a scenario for how gas falls into the galaxy as a function of time, is transformed into stars (Kennicutt 1998), and is subsequently released back into the ISM. By studying the differences in the chemistry between stellar populations and comparing them to predictions from models, we aim to identify which scenarios are consistent with observed abundance distributions, and quantify the relative importance of external and internal evolutionary processes.

Measurements of the abundance of α-elements (Ne, Mg, Si, S, Ar, Ca, Ti) in stellar populations are fundamental to Galactic archaeology, as they originate from primarily one source with a well-modeled lifetime, and therefore directly correlate to the history of star formation for a given population. α-elements are produced in Type II, or core-collapse, supernovae by massive stars ($M > 8M_\odot$) with short lifespans ($\sim 10^6$ years, e.g. Arnett 1996). The abundance of α-elements in a star is typically compared to its iron abundance, as iron is produced predominately in Type Ia supernovae on much longer timescales ($\sim 10^9$ years, e.g. Smecker-Hane & Wyse 1992; Nomoto et al. 1997). Type Ia supernovae occur when a white dwarf in a binary system accretes enough material from its companion to have a mass greater than the Chandrasekhar mass ($1.44M_\odot$, e.g. Nomoto et al. 2013, and references therein). Stars with a high ratio of α-elements to iron indicate they were formed from gas that was enriched primarily by Type II supernovae, while stars with a low [α/Fe] ratio formed from gas with a much higher iron content, after Type Ia supernovae released their yields back into the ISM. Therefore, the relative abundance of α-elements to iron indicates the proportion of Type II to Type Ia supernovae progenitors present

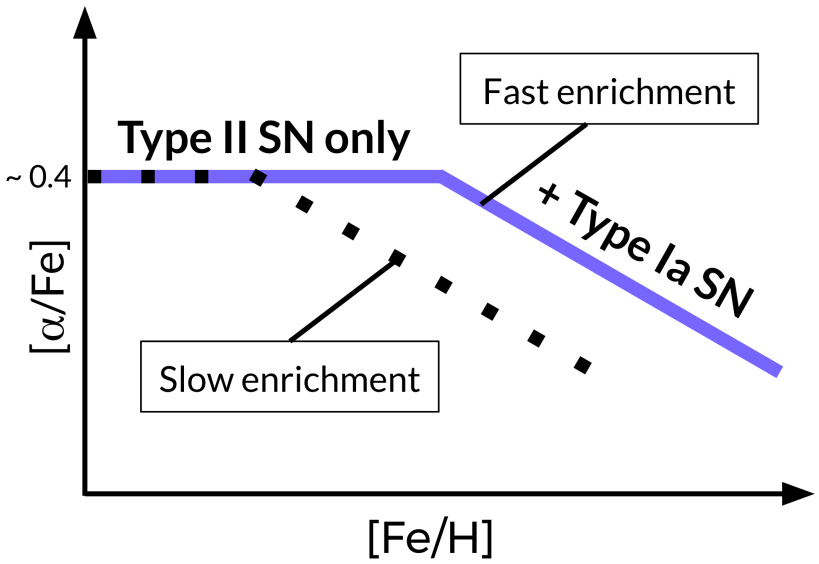

Figure 1.3 — Simplified diagram illustrating how theoretical trends in [α/Fe]-[Fe/H] space change with different star formation histories. Adapted from Figure 2 of Wyse (2016).

in the environment in which a given stellar population formed, and serves as a proxy for the age of a population.

As [α/Fe] can be considered a proxy for age, it can be used to identify different enrichment histories (and therefore star formation histories) in different stellar populations. Figure 1.3 presents an illustration of how [α/Fe] varies as a function of [Fe/H] for populations with different star formation histories. The plateau[5] in [α/Fe] as a function of [Fe/H] is a natural consequence of Type II supernovae dominating the enrichment history of the early Galaxy, and as Type Ia supernovae begin to explode, this ratio gradually decreases. The position of the 'knee', which indicates the onset of Type Ia supernovae, varies as a function of the star formation history of a stellar population, such that a population with a slow enrichment will have a knee at lower values of [Fe/H] compared to a population with a faster enrichment history, which will have a knee at a higher value of [Fe/H]. Figure 1.4 demonstrates this using observational data, showing the difference in trends in this chemical space between dwarf galaxies of the Milky Way (coloured points), and the Milky Way itself (black points). In this way, α-elements can be used as an indicator of accreted populations, as they will show significantly different chemical abundance patterns from stars born *in situ*.

As a result, many recent studies of the evolutionary history of the disc in the solar neighbourhood focus on the distribution of stars in the [α/Fe]-[Fe/H] plane (e.g. Fuhrmann 2008; Bensby et al. 2014; Haywood et al. 2013; Hayden et al. 2015; Recio-Blanco et al. 2014; Kordopatis et al. 2015b). An example of the distribution of nearby ($d \lesssim 25$ pc) solar neighbourhood stars in this chemical space is given in Figure 1.5. The prominence of studies of this chemical space arose from the discovery of two

[5]The value of this plateau varies with the initial mass function and supernovae yields of a given population (e.g. Matteucci 2001; Helmi 2008; Wyse 2016).

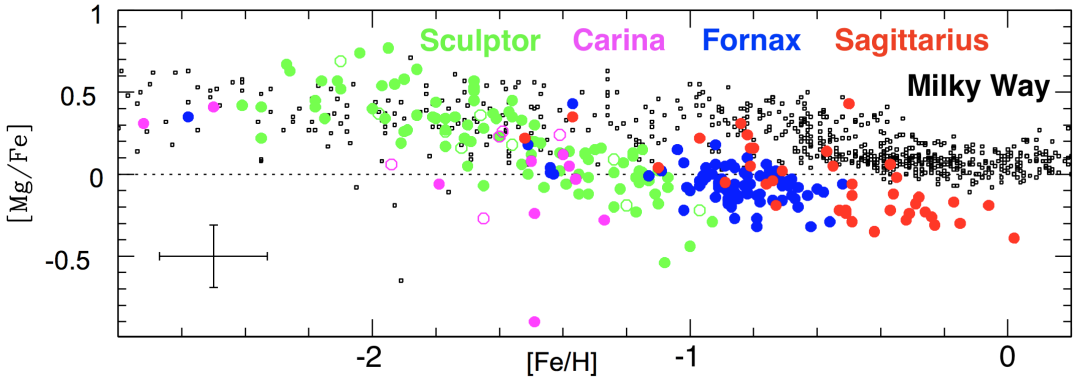

Figure 1.4 — Magnesium (Mg) versus iron (Fe) in four nearby dwarf spheroidal galaxies: Sagittarius (red: Sbordone et al. 2007; Monaco et al. 2005; McWilliam & Smecker-Hane 2005), Fornax (blue: Letarte 2007; Shetrone et al. 2003), Sculptor (green: Shetrone et al. 2003; Geisler et al. 2005; Tolstoy et al. 2009) and Carina (magenta: Koch et al. 2008; Shetrone et al. 2003). Open symbols refer to single-slit spectroscopy measurements, while filled circles refer to multi-object spectroscopy. The small black symbols are a compilation of the MW disk and halo star abundances, from Venn et al. (2004). Adapted from Figure 11 of Tolstoy et al. (2009).

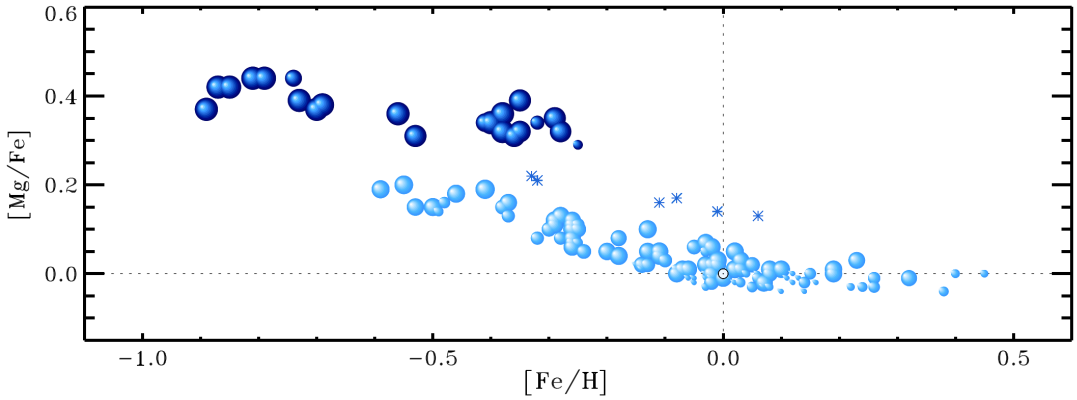

Figure 1.5 — [Mg/Fe]-[Fe/H] plane for a sample of nearby solar neighbourhood stars, showing distinct trends between the α-high sequence (typically associated with the thick disc, dark blue), and the α-low sequence (typically associated with the thin disc, light blue). Transition objects are indicated with asterisks. The diameter of a point is proportional to its age estimate. Adapted from Figure 5 of Fuhrmann et al. (2017).

distinct sequences in [α/Fe]-[Fe/H], indicating significant differences in the star formation and enrichment history of each of these components.

Age

While large-scale surveys continue to expand our knowledge of the kinematics and chemistry of stellar populations, one crucial aspect has proved elusive: individual stellar ages. Currently, the Sun is the only star for which we have an accurate age estimate. We can study firsthand the composition of the material from which the Sun and the solar system were formed (e.g., radioactive dating of meteorites, Bahcall et al. 1995), as well as measure precisely the seismic activity of the Sun (helioseismology, Bonanno et al. 2002), where both methods give a consistent value, 4.57 Gyr. However, for stars other than our Sun, determining ages is much more difficult. While it is possible to obtain some information about the composition of a star via spectroscopy, we cannot directly measure the half-life of long-lived isotopes present in the material from which they formed. And while techniques for measuring the seismic activity in stars (asteroseismology, e.g. Chaplin & Miglio 2013; Davies & Miglio 2016) have vastly improved in the past decade, they are only viable for certain subsets of stars for which these oscillations are measurable (e.g., red giant and variable stars).

To determine ages of stars, and in particular low-mass stars because they have lifespans of the order of the age of the Galaxy, we must rely on models of stellar evolution. The most widely used method[6] to determine ages of stars is to fit a theoretical isochrone to their position in a Hertzsprung-Russell (HR) diagram (e.g. Edvardsson et al. 1993; Chen et al. 2000; Reddy et al. 2003; Pont & Eyer 2004). This method is relatively successful for mono-age populations such as open clusters, as it is possible to identify and statistically fit certain features of the HR diagram (e.g. the turnoff region) of such objects. However, for individual stars, degeneracies due to multiple isochrones fitting a single point increases uncertainties in their age estimate. With the increasing availability of large samples of stars with spectroscopically derived parameters, significant efforts have been made to improve isochrone fitting techniques to utilize all available information via Bayesian methods (e.g. Pont & Eyer 2004; Jørgensen & Lindegren 2005; Burnett & Binney 2010; McMillan et al. 2017). While additional constraints, such as distance and metallicity, can be used to improve Bayesian age estimates, uncertainties are at best of the order of 20% (typically 50-100%). However, significant work has been done with small, local samples, where distances, and therefore ages, of field stars can be determined to a reasonable precision (e.g. Fuhrmann 2008; Haywood et al. 2013; Bensby et al. 2014; Fuhrmann et al. 2017). Below, we highlight some of the most crucial findings utilizing stellar ages, and their implications for Galactic archaeology.

Age and chemistry. Of the relations between stellar properties, one of the most important for understanding the evolution of the Galaxy is the correlation between age and metallicity (age-metallicity relation, AMR). While it is expected that stars at a given Galactic radius generally become more metal-rich as the ISM becomes more enriched with yields from supernovae (Section 1.3.1), this relation can become

[6] For a thorough review of age determination methods, see Soderblom (2010).

blurred as stars can migrate from their birthplace (Sellwood & Binney 2002). One of the first studies to characterize this relation was conducted by Edvardsson et al. (1993), where they derived individual abundances for a sample of 189 nearby stars, and found a large range of metallicities at a given age, indicating at best a weak correlation between age and metallicity. More recently, Bensby et al. (2014) used a sample of 714 FGK stars to explore the relationship between age, metallicity, and kinematics in the solar neighbourhood, and for their kinematically-selected thick disc and young ($\tau < 8$ Gyr) stars in their kinematic thin disc, they find a correlation between age and metallicity.

Age and kinematics. In addition to the age-metallicity relation, acquiring the ages for field stars in the solar neighbourhood also allows us to explore another critical relation in understanding the formation history of the Galactic disc: the relationship between age and velocity dispersion (the age-velocity dispersion relation, AVR). Wielen (1977) measured the space velocities and ages for a small sample of nearby stars, and found that the velocity dispersion increases as a function of age for all velocity components. Holmberg et al. (2007) and Casagrande et al. (2011) used the Geneva-Copenhagen survey (GCS) to investigate heating mechanisms in the disc. Casagrande et al. (2011) found increasing velocity dispersion with age, with $\sigma_U < \sigma_V < \sigma_W < \sigma_{tot}$. The presence of an AVR in the disc has been attributed to evolutionary processes, e.g. a minor merger responsible for the formation of the thick disc (Quillen & Garnett 2001), and remains a crucial comparison for Galactic models.

1.3.2 Facilities: Large-scale surveys of the Milky Way

Astrometry. Catalogues of the positions of stars can be be traced to antiquity (Hipparchus, 190 BC), and remains an active area of modern astrophysics. The Hipparcos mission ushered in a new era of astrometric catalogues, providing positions, parallaxes, and proper motions for over 100 000 nearby ($d \lesssim 200$ pc) stars (Perryman et al. 1997). A few years later, Tycho-2 (Høg et al. 2000) provided a larger catalogue of the brightest 2.5 million stars.

More recently, on 14 September 2016 the first data release of Gaia was made publicly available, providing the positions and G-band magnitudes for over a billion stars brighter than $G > 21$ (Gaia Collaboration et al. 2016; Lindegren et al. 2016). In addition to Gaia DR1, the Tycho-Gaia astrometric solution (TGAS, Michalik et al. 2015) provided parallaxes and proper motions for over 2 million stars contained in the Tycho-2 catalog. At the moment, this catalog provides the greatest number of accurate distance and proper motion measurements for stars out to ~ 2 kpc.

Photometry. While the importance of large-scale astrometric surveys cannot be overstated, they present significant technical challenges which have not been resolvable until relatively recently. Prior to Gaia, photometric (imaging) surveys offered the largest data sets for conducting studies of MW stellar populations. With larger telescopes and coordinated, international efforts, the past two decades saw the rise in large-scale photometric surveys, aiming for deep, full sky coverage. Of these, perhaps the most widely known and used are the Tycho-2 catalogue, which contains two-colour photometric information in addition to astrometric data, the

Sloan Digital Sky Survey (SDSS, Blanton et al. 2017), and the Two Micron All Sky Survey (2MASS, Skrutskie et al. 2006). The SDSS obtained deep photometric imaging across five optical photometric bands for over one third of the sky, with the latest data release containing photometry for over 260 million stars (Blanton et al. 2017). The 2MASS catalogue, released in 2003, provided infrared photometry for $\sim$ 300 million stars, covering over 99% of the sky. With accurate multi-band photometric measurements of stars, it is possible to obtain estimates of individual stellar distances and metallicities, and as a result these surveys often paved the way for higher-resolution, follow-up spectroscopic surveys.

Spectroscopy. Finally, the past decade has seen enormous advances in the number and depth of large-scale spectroscopic surveys. With the advent of multi-object spectrographs obtaining spectra for multiple stars simultaneously, large-scale surveys can obtain homogeneous coverage of large areas of the sky in a systematic and time effective way. From a stars spectrum, it is possible to determine its chemical composition, as well as other fundamental physical characteristics, such as temperature and surface gravity. In addition, spectra can also provide measurements of a stars radial velocity via the Doppler effect. When combined with astrometric measurements (proper motion and parallax), it is then possible to characterize the three dimensional motion of a star through space. There are a number of completed, ongoing and upcoming large-scale spectroscopic surveys (Table 1.1), such as the RAdial Velocity Experiment (RAVE, Steinmetz et al. 2006) survey, the APO Galactic Evolution Experiment (APOGEE, Majewski et al. 2015), the Large Sky Area Multi-Object Fibre Spectroscopic Telescope (LAMOST, Zhao et al. 2012) survey, the Sloan Extension for Galactic Understanding and Exploration (SEGUE, Yanny et al. 2009), the GALactic Archaeology with HERMES (GALAH, De Silva et al. 2015) survey, and the Gaia-ESO (Gilmore et al. 2012) survey. Planned surveys include those part of the 4-metre Multi-Object Spectroscopic Telescope (4MOST, de Jong 2011) and WEAVE (Dalton et al. 2012) spectroscopic facilities (for more details, see Section 5.2). In a sense, these surveys are complementary, exploiting different wavelength ranges or sky coverage to address similar science questions. As all of the work presented within this thesis relies on data available via the RAVE survey, it is described in detail below.

RAVE

The RAVE survey, which ran from 2003-2013, obtained spectra for approximately half a million Southern hemisphere stars (Figure 1.6). A full description of the project and subsequent data products can be found in the data release papers: DR1 (Steinmetz et al. 2006); DR2 (Zwitter et al. 2008); DR3 (Siebert et al. 2011b); DR4 (Kordopatis et al. 2013a), and DR5 (Kunder et al. 2017). The medium-resolution ($R \sim 7500$) spectra, centred on the Ca II-triplet region (8410-8795Å), were observed using the 6dF multi-object spectrograph on the 1.2m UK Schmidt telescope located at the Siding Spring Observatory in Coonabarabran, NSW, Australia. The primary focus of RAVE was to obtain radial velocity measurements for stars in the magnitude range $9 < I < 12$. By measuring the Doppler shift of the strong calcium absorption lines, this was possible for even low signal-to-noise spectra (SNR $\lesssim 10$ per pixel). As

Survey	Spectral range Å	Resolution R = $\lambda/\Delta\lambda$	Magnitude limit	No. stars
RAVE	8410-8795	7500	$9 < I < 12$	$\sim 5 \times 10^5$
LAMOST	3700-9000	1800	$r < 17.8$	$\sim 5.7 \times 10^6$
SEGUE	3900-9000	1800	$14 < g < 20.3$	$\sim 2.4 \times 10^5$
APOGEE	15100-17000	22500	$8 < H < 13.8$	$\sim 1.5 \times 10^5$
GALAH	4713-7887(1)	28000/42000(2)	$V < 14$	$\sim 10^6$
Gaia-ESO	–	18000/47000(2)	$12.5 < J < 17.5$(1)	$\sim 10^5$
Gaia	8450-8720	11200	$G < 16$	$\sim 150 \times 10^6$
4MOST	3700-9500(1)	5000/20000(2)	$r < 19$	$\sim 20 \times 10^6$
WEAVE	4000-9500	5000/20000(2)	$V > 15.5$	$\gtrsim 10^6$

Table 1.1 — Finished, ongoing, and planned large-scale spectroscopic surveys. (1): Coverage is not continuous in this range. (2): Values indicate low/high-resolution modes, respectively.

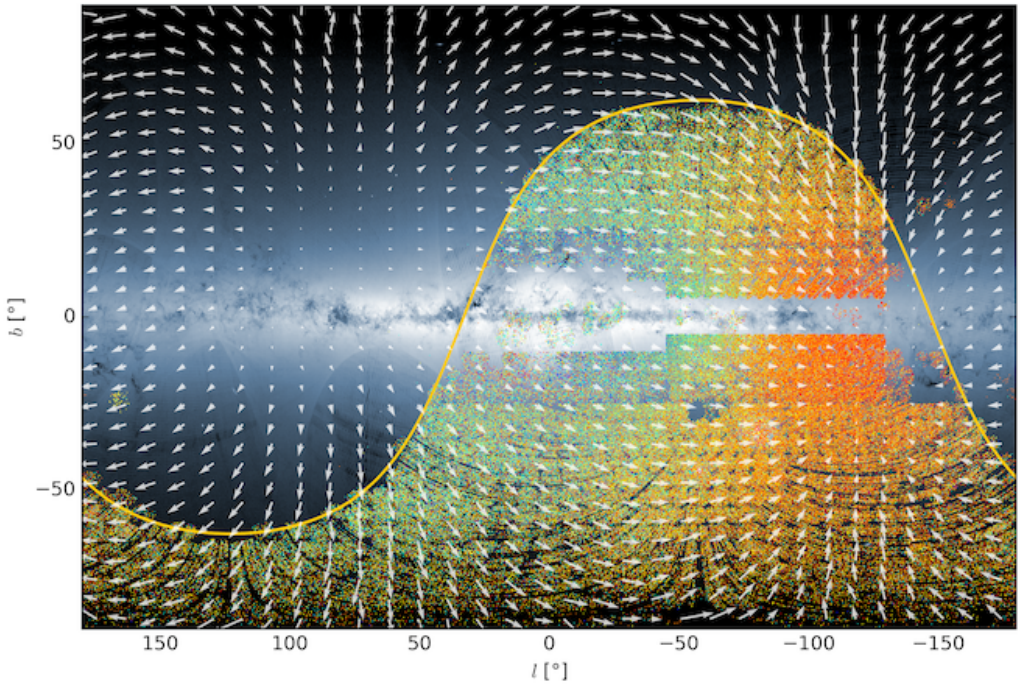

Figure 1.6 — Sky coverage of the RAVE survey in Galactic coordinates. Points are colour-coded by their average heliocentric radial velocity, with red indicating positive values and blue indicating negative values. Overplotted arrows show proper motion values from the TGAS catalogue. Credit: Maarten Breddels (stellar density and proper motions), Kristin Riebe (RAVE stars); the RAVE collaboration.

part of the work done for this thesis, the selection function of the RAVE survey is presented in Chapter 3.

In addition to radial velocities, the latest data release (DR5, Kunder et al. 2017) contains additional stellar parameters derived from the spectra, obtained using the pipeline described in Kordopatis et al. (2013a): effective temperature, surface gravity, and metallicity ([M/H]). In addition, many stars have individual chemical abundances (Mg, Al, Si, Ca, Ti, Fe, and Ni) available, derived using the chemical abundance pipeline presented in Boeche et al. (2011). At the time of writing, out of all of the large-scale spectroscopic surveys, RAVE has the largest overlap with TGAS, with $\sim 215\,000$ stars in common. With radial velocities and stellar parameters from RAVE, and parallax measurements from TGAS, the combined RAVE-TGAS catalogue offers a statistically significant sample of solar neighbourhood stars ($d \lesssim 1$ kpc), suitable for exploring open questions in Galactic archaeology.

1.4 Thesis summary

1.4.1 Open questions

In this work, we address a number of open questions relating to the chemodynamical history of the local stellar disc, using samples of solar neighbourhood stars from the RAVE survey.

How did the thick disc form, and what is its relation to the thin disc?

Formation scenarios of the thick disc are numerous (Section 1.2.3), each with their own successes and flaws. A goal of Galactic archaeology is to determine which effects dominate, and explore the relationship between the formation of the thin and thick discs. These components can be identified as separate sequences in chemical space (Section 1.3.1), indicating distinct star formation histories (e.g. Lee et al. 2011; Adibekyan et al. 2013; Hayden et al. 2015). In Chapter 2, we use a sample of RAVE stars to identify chemically distinct disc components to explore and address these questions.

What is the efficiency of radial migration?

Radial migration is well accepted as a dynamical mechanism affecting disc stars (Sellwood & Binney 2002), however, the strength and efficiency of this process is not well constrained. Radial migration directly influences the observed stellar population at any given radius and therefore possibly radial gradients in kinematics (e.g. Siebert et al. 2011a, 2012; Williams et al. 2013), or chemistry (e.g. Boeche et al. 2013; Gazzano et al. 2013; Genovali et al. 2014; Kordopatis et al. 2015b). In Chapters 2 and 4, we identify observational signatures of radial migration in the solar neighbourhood.

How do non-axisymmetries in the disc affect the local velocity field?

The local velocity field is full of substructure, with the Sirius, Pleiades, Hyades (Eggen 1958; Boss 1908; Zuckerman et al. 2004; Famaey et al. 2007) and Hercules (Famaey et al. 2008) moving groups identified in the solar neighbourhood. From models of the Milky Way disc, these moving groups are ascribed to stars which have orbits trapped by a resonance due to some non-axisymmetric perturbation in the disc (e.g. Kalnajs 1991; Monari et al. 2014), such as spiral arms, or the bar (e.g. Hercules, Dehnen 2000; Famaey et al. 2008). In Chapter 4, we investigate the chemodynamical structure of these populations, to place further constraints on the source of such perturbations, and construct a more complete picture of the Galactic bar and disc.

1.4.2 Paper I: Chemical separation of disc components using RAVE

In Chapter 2, we present a study of the kinematics of chemically separated Milky Way disc components, using a sample of $\sim 20\,000$ solar neighbourhood ($d \lesssim 1$ kpc) stars in RAVE. As the gap in chemical space ([Mg/Fe]-[Fe/H]) is not clearly visible in RAVE, we construct a simple two dimensional probability density function (pdf) based on high-resolution studies (Kordopatis et al. 2015b) in order to identify stars belonging to either the α-high ('thick' disc) or α-low ('thin' disc) in a probabilistic way. After assigning stars as belonging to a given disc component, we investigate kinematic trends as a function of metallicity for each component.

We find distinct differences in the kinematics between our α-low and α-high disc components, most noticeably in the azimuthal velocity component. In particular, measure a negative gradient in $\partial V_\phi/\partial$[Fe/H] for our α-low stars, and a positive gradient for the α-high component. For our α-low stars, as the rotational velocity decreases as metallicity increases, the most metal-rich α-low stars lag the LSR by $\sim 10\,\mathrm{km\,s^{-1}}$, and we measure a gradient of $\partial V_\phi/\partial[\mathrm{Fe/H}] = -11 \pm 1\,\mathrm{km\,s^{-1}dex^{-1}}$. In contrast, the α-high stars all lag the LSR. For this component, as metallicity increases, the rotational velocity increases, giving a positive gradient of $\partial V_\phi/\partial[\mathrm{Fe/H}] = 51 \pm 10\,\mathrm{km\,s^{-1}dex^{-1}}$. While we do expect some contamination of incorrectly assigned stars in both of our disc components, the values that we measure for these gradients are roughly consistent with literature values from both low- and high-resolution studies (e.g. Lee et al. 2011; Kordopatis et al. 2011; Adibekyan et al. 2013; Recio-Blanco et al. 2014).

When we consider the velocity dispersion as a function of [Fe/H] for each component, we also find differing trends. Our α-high sequence shows significantly higher velocity dispersions in each component of velocity, as expected for a 'thick' disc. The α-low stars represent a kinematically cooler population, with velocity dispersions on average $\sim 16\,\mathrm{km\,s^{-1}}$ lower than the α-high stars. As a function of metallicity, we find that the dispersion decreases with increasing metallicity for all components. Finally, with measurements of both the mean rotational velocity and the velocity dispersion, we estimate the scalelength of each disc component, finding the α-high component (chemical thick disc) to be more centrally concentrated than the α-low component.

From these findings, we draw the following conclusions. With RAVE, we are able to find evidence, consistent with results from high-resolution studies, of chemically separated, kinematically distinct disc components in the solar neighbourhood. The positive gradient that we measure for the α-high component can be explained by asymmetric drift: as the rotational velocity increases as a function of metallicity, the velocity dispersion correspondingly decreases, consistent with results from previous studies. For the α-low component, we consider the presence of metal-rich stars lagging the LSR to indicate that some process has brought them from the inner Galaxy from the solar neighbourhood. We consider both the effects of blurring and churning, and conclude the effect we see is likely due to some combination of these processes.

1.4.3 Paper II: The selection function of the RAVE survey

Chapter 3 presents, in detail, the selection function of the RAVE survey. Understanding and characterizing the selection function of spectroscopic surveys is necessary in order to draw robust, unbiased conclusions from their data products. We determine the completeness fraction of RAVE as a function of position on the sky, magnitude, and colour, using 2MASS as a parent sample (i.e., 2MASS contains all stars which could have been observed in RAVE). In order to take into account temporal changes (night-to-night, field-to-field variations), we calculate the completeness of RAVE in two ways: on a field-by-field basis, and on a pixel-by-pixel basis (using HEALPIX (Górski et al. 2005) pixels).

With the selection function in hand, we then use the stellar population synthesis code GALAXIA (Sharma et al. 2011) to construct a mock-RAVE catalogue by applying the selection function to a parent GALAXIA sample. To test whether the selection function of RAVE imposes biases in the kinematic or chemical distributions of the observed stars, we compare our mock-RAVE catalogue to the parent GALAXIA sample. For stars brighter than I=12, we find no significant kinematic or chemical biases with respect to GALAXIA in RAVE stars due to the selection function, indicating that overall, RAVE offers a representative sample of stars to investigate chemodynamical trends in the solar neighbourhood. We note that this result is valid only for the parameter space where the RAVE stellar parameter pipeline produces reasonable results: $4000\mathrm{K} < T_{\mathrm{eff}} < 8000\mathrm{K}$ and $0.5 < \log g < 0.5$. Both versions of the RAVE selection function have been made available on the RAVE website.

1.4.4 Paper III: Correlations between age, chemistry, and kinematics as seen by RAVE

In Chapter 4, we use the updated distance and age estimates presented in McMillan et al. (2017) to fold age information into our chemodynamical studies of the extended solar neighbourhood with RAVE. We first conduct an extensive validation of the age estimates using a RAVE-like sample of stars generated with GALAXIA, and find turnoff stars provide the most reliable age estimates, as the isochrones in this region are relatively well separated. However, we find a significant systematic offset for intermediate age turnoff stars, and therefore consider only two age groups:

young ($0 < \tau < 3$ Gyr) and old ($10 < \tau < 13$ Gyr). We apply this turnoff selection to our RAVE stars, along with additional quality criteria to ensure a robust, high-quality sample of stars with reasonable age estimates. For each age group, we also consider four bins in metallicity, in order to investigate the star formation history of the disc at different epochs.

We then explore kinematic trends as a function of Galactocentric radius (R). We find that our young stars exhibit a significant negative gradient in radial velocity as a function of R, in agreement with previous studies (Siebert et al. 2011a; Williams et al. 2013). However, the gradient that we measure is much steeper than previously found, and varies as a function of metallicity. While old stars also indicate the presence of a radial velocity gradient, the signature is much weaker, and does not seem to depend as strongly on metallicity. To understand why this gradient is stronger in young stars, we consider the source of this effect. Siebert et al. (2011a) conclude that the observed gradient is a result of a non-axisymmetry in the Galactic potential, due to either the bar, spiral arms, the warp of the disc, a triaxial dark matter halo, or some combination of these components. As we find a stronger gradient in young stars, which are typically kinematically colder, we limit our discussion to dominant features of the stellar disc: the bar and spiral arms. When we explore the kinematics of our age groups in the $V_R - V_\phi$ plane, we find contributions from the Hercules moving group (associated with the bar) for both old and young populations, while the Hyades moving group (associated with the spiral arms) affects primarily young stars.

This result is also reflected in the flattening of the radial velocity gradient for our young stars as a function of [Fe/H]. The most metal-rich stars, coming from the inner Galaxy, are sensitive to perturbations from both the bar and spiral arms. As we move to successively metal- poor samples, we find less of a contribution from the Hercules stream in the $V_R - V_\phi$ plane, corresponding to the fact that on average, metal-poor stars having guiding radii at greater distances from the Galactic centre compared to metal-rich stars.

Finally, we also find differences between our young and old samples in the mean azimuthal velocity as a function of Galactocentric radius. For our young sample, we find a slight positive gradient for our metal-rich stars, which flattens and inverts for metal-poor stars. Inward of the solar neighbourhood ($R < 8.0$ kpc), metal-rich stars lag the LSR more than at larger Galactocentric radii. For our young metal-poor stars, we find that inward of the solar neighbourhood, they have rotational velocities greater than the LSR. This finding correlates with the scenario that the young metal-rich stars originate from the inner Galaxy, while young metal-poor stars are more likely to be born in the outer Galaxy. Their presence in the solar neighbourhood indicates that their orbits have been affected by some dynamical processes (e.g. blurring or churning) to bring them to the local vicinity. When we consider the eccentricity distributions of these stars, we find that while some young stars have eccentric orbits, the majority have orbits which are relatively circular. In addition, the trends we find are not as strong as what we would expect from blurring alone, and therefore we conclude that some of these stars must have been affected by churning, in agreement with previous studies (e.g. Kordopatis et al. 2015a).

2 Chemical separation of disc components using RAVE

Jennifer Wojno, Georges Kordopatis, Matthias Steinmetz, Paul McMillan, Gal Matijevič, James Binney, Rosemary F. G. Wyse, Corrado Boeche, Andreas Just, Eva K. Grebel, Arnaud Siebert, Olivier Bienaymé, Brad K. Gibson, Tomaž Zwitter, Joss Bland-Hawthorn, Julio F. Navarro, Quentin A. Parker, Warren Reid, George Seabroke, Fred Watson

— Published as J. Wojno et al., 2016, MNRAS 461, 4246 —

ABSTRACT

We present evidence from the RAdial Velocity Experiment (RAVE) survey of chemically separated, kinematically distinct disc components in the solar neighbourhood. We apply probabilistic chemical selection criteria to separate our sample into α-low ('thin disc') and α-high ('thick disc') sequences. Using newly derived distances, which will be utilized in the upcoming RAVE DR5, we explore the kinematic trends as a function of metallicity for each of the disc components. For our α-low disc, we find a negative trend in the mean rotational velocity (V_ϕ) as a function of iron abundance ([Fe/H]). We measure a positive gradient $\partial V_\phi / \partial$[Fe/H] for the α-high disc, consistent with results from high-resolution surveys. We also find differences between the α-low and α-high discs in all three components of velocity dispersion. We discuss the implications of an α-low, metal-rich population originating from the inner Galaxy, where the orbits of these stars have been significantly altered by radial mixing mechanisms in order to bring them into the solar neighbourhood. The probabilistic separation we propose can be extended to other data sets for which the accuracy in [α/Fe] is not sufficient to disentangle the chemical disc components *a priori*. For such datasets which will also have significant overlap with Gaia DR1, we can therefore make full use of the improved parallax and proper motion data as it becomes available to investigate kinematic trends in these chemical disc components.

2.1 Introduction

In recent years the study of the history of our Galaxy through detailed observations of stellar populations has developed into the field known as Galactic archaeology. From our position within the Milky Way, we have the unique opportunity to study stellar dynamics and chemistry in great detail. Large-scale spectroscopic surveys such as RAVE (Steinmetz et al. 2006), SEGUE (Yanny et al. 2009), APOGEE (Majewski et al. 2015), Gaia-ESO (Gilmore et al. 2012), LAMOST (Zhao et al. 2012), and GALAH (De Silva et al. 2015) now make it possible to disentangle the history of star formation and chemical enrichment, and thus to reconstruct the development of the Galaxy as a whole.

Stars hold chemical information about their birth environment in the composition of their atmospheres, which remain relatively constant over their main-sequence lifetime (Freeman & Bland-Hawthorn 2002). If stars remained at their birth radii throughout their entire lives, and the metallicity of the ISM increased monotonically, we would expect to observe a tight correlation between stellar metallicity and age; however, in the solar neighbourhood, a range of metallicities has been observed at a given age (e.g. Edvardsson et al. 1993; Haywood 2008; Bergemann et al. 2014). For the oldest stars ($\tau > 8$ Gyr) a correlation between age and metallicity *is* observed (Haywood et al. 2013), and a variety of mechanisms have been proposed to reconcile the lack of correlation for stars younger than 8 Gyr. The mechanisms include a non-monotonic increase in metallicity (e.g. inhomogeneities in the early turbulent interstellar medium (ISM) Haywood et al. 2013; Bournaud et al. 2009; Brook et al. 2004), and dynamics of stars such that they are sometimes observed far from their birth radii.

Sellwood & Binney (2002) discussed the impact of orbital dynamics on age-metallicity relations in terms of two processes. As a star ages, the eccentricity of its orbit increases, widening the radial band within which the star may be observed. This process they called "blurring". Sellwood & Binney (2002) showed that from time to time a star's guiding centre can shift fairly abruptly to a smaller or larger radius following an interaction with a transient non-axisymmetric perturbation of the disc. They dubbed this process "churning". Whereas blurring on its own is not powerful enough to account for the wide range of metallicities present near the Sun at a given age, Schönrich & Binney (2009b) argued that churning and blurring working together account rather nicely for the data from the Geneva-Copenhagen Survey (Nordström et al. 2004; Holmberg et al. 2007).

Of particular interest in the context of radial mixing are stars with super-solar metallicity, or super metal-rich (SMR)[1] stars (Kordopatis et al. 2015a). The presence of these metal-rich stars in the solar neighbourhood has long been problematic for the theory of Galactic chemodynamics (e.g. Grenon 1972; Israelian & Meynet 2008). The ISM in the solar neighbourhood is expected now to be as metal-rich as it has ever been, and is now around solar metallicity and relatively homogeneous (Cartledge et al. 2006). If we assume a monotonic metallicity gradient in the disc, for SMR stars we infer birth radii $R \lesssim 3$kpc (Kordopatis et al. 2015a).

[1] For our sample, we define SMR stars as those with [Fe/H] $\gtrsim$ 0.15.

For lower metallicities, we consider the chemodynamical history of the thick disc. While the mechanisms by which the thick disc formed are hotly debated, the thick disc consists mostly of old, metal-poor ($\sim -1.5 <$ [Fe/H] < 0.1), α-enhanced stars on kinematically hotter orbits than thin-disc stars (Chiba & Beers 2000; Bensby et al. 2003). Although Bovy et al. (2012b), using low-resolution spectra, argued that the thin and the thick discs blend continuously into one another, a trough in the density of stars in the space of α-abundance versus metallicity leads the majority of authors to suppose that the thin and thick discs have experienced different evolutionary histories (e.g. Lee et al. 2011; Fuhrmann 2011; Adibekyan et al. 2013; Haywood et al. 2013; Bensby et al. 2014; Recio-Blanco et al. 2014; Guiglion et al. 2015; Hayden et al. 2015; Kordopatis et al. 2015b). Indeed, Aumer et al. (2016) show that in N-body models scattering of stars by the inevitable non-axisymmetric features in a disc generates structures remarkably like the thin disc, but do not generate significant thick discs (see also Minchev et al. 2012, but also Schönrich & Binney 2009a,b; Loebman et al. 2011 for how thick discs may be formed due to radial migration). They conclude that the thick disc was present before the thin disc started to form. By assigning stars as belonging to either the thin or thick disc according to their chemical properties, we can explore the possible differences in the chemodynamical properties of these populations.

In this paper, we aim to identify chemically distinct thin and thick disc components using the medium resolution ($R \sim 7500$) RAdial Velocity Experiment (RAVE) survey (Steinmetz et al. 2006). The magnitude-limited ($9 < I < 12$) RAVE survey offers a kinematically unbiased sample of stars, ideal for investigating stellar dynamics. The fourth data release (DR4), presented in Kordopatis et al. (2013a, hereafter K13), provides radial velocities, stellar parameters, abundance measurements (Boeche et al. 2011), and distance estimates (Binney et al. 2014a) for 425 561 stars, making it one of the largest spectroscopic surveys with unique statistical strengths. Combining these radial velocity data and distance estimates with proper motions, full 6D (position and velocity) information is available for the majority of stars.

The paper is organized as follows: Section 2.2 briefly describes the quality criteria and parameter cuts applied to obtain the final working sample, improvements on the data set, and methods to derive stellar kinematic properties used in the analysis. Section 2.3 describes the method used to disentangle the chemical disc components. Section 2.4 presents the kinematic trends for each component. We characterize the trends in mean V_ϕ velocity for both the α-low and α-high populations, and discuss trends observed in the dispersions of all three velocity components. We also estimate the scale lengths of our chemically selected discs. In Section 2.5 we discuss implications for these findings, and in particular discuss possible origins of our metal-rich, α-low stars. Finally, Section 2.6 summarises our results.

2.2 RAVE data sample and kinematics

To ensure a high quality sample of stars in the extended solar neighbourhood, we use a subsample of RAVE DR4 that meets a number of quality criteria. First, we

select stars with signal-to-noise (SNR) per pixel > 80. We remove stars that emerge from the chemical abundance pipeline (Boeche et al. 2011) with CHISQ_c > 2000, so retaining only stars with a good fit between template and observed spectra. In addition, we require the quality flag on the convergence of the DR4 pipeline to be Algo_Conv_K ≠ 1.[2] Finally, we utilize stellar classification flags described in Matijevič et al. (2012) to exclude a small fraction of stars with spectra for which the learning grid contains no template – e.g. stars with chromospheric emission (Žerjal et al. 2013), spectra with wavelength calibration problems, carbon stars, and binary stars.

After these quality cuts have been applied, we remove all stars with line-of-sight distances greater than 1 kpc. We focus our investigation on the kinematics of stars in the extended solar neighbourhood because the global properties in this domain have been extensively studied, and the metallicity gradient $\partial[\mathrm{M/H}]/\partial R \sim -0.06 \mathrm{km\,s^{-1}kpc^{-1}}$, (e.g. Genovali et al. 2014; Boeche et al. 2013), and velocity gradient $\partial V_{R,\phi,Z}/\partial R \sim \pm 3 \mathrm{km\,s^{-1}kpc^{-1}}$, (e.g. Siebert et al. 2011a; Monari et al. 2014) are such that changes in mean velocity and metallicity across this volume are small. In addition, we require that the total space velocity, V_{tot}, is less than the Galactic escape speed, V_{esc}, where we adopt the lower limit $V_{\mathrm{esc}} \geq 492 \mathrm{km\,s^{-1}}$ determined by Piffl et al. (2014). Our sample is further reduced because not all RAVE stars have abundance measurements in DR4. After these cuts, we are left with a sample of 20 751 stars, which is evenly split between 10 384 dwarfs and 10 367 giants.

Galactocentric space velocities in a right-handed cylindrical coordinate system were determined using the equations summarised in Appendix A of Williams et al. (2013). First, to transform the observed velocities into a Galactocentric coordinate system, we adopt values for the solar peculiar motion with respect to the Local Standard of Rest (LSR) of $(U,V,W)_\odot$ = (11.10, 12.24, 7.25) km s^{-1} from Schönrich et al. (2010). In addition, we take the location of the Sun to be (R_0, z_0) = (8.3, 0) kpc and the LSR speed to be $V_{LSR} \sim 240$ km s^{-1} (Schönrich 2012). When calculating the Galactocentric space velocities, we use radial velocity measurements from DR4, Galactic coordinates (ℓ, b) from 2MASS (Cutri et al. 2003) and proper motion measurements from UCAC4 (Zacharias et al. 2013)[3]. Distances have been provided using a version of the RAVE distance pipeline (Binney et al. 2014a) that has been updated to include an extended range of Padova isochrones (Bertelli et al. 2008) down to [Fe/H] = −2.2, while it was previously limited to −0.9 dex. These improved distances only systematically affect the results for the most metal-poor stars.

2.3 Chemical separation of the disc

We separate our sample into two populations using a chemical criterion: the star's position in plane spanned by α-abundance ([Mg/Fe]) versus iron abundance ([Fe/H]). While the thin (D) and thick disc (TD) overlap spatially and kinematically,

[2] A flag of 1 indicates that the pipeline failed to converge (for more details see K13).

[3] While DR4 also provides a number of sources for proper motion measurements, we find no substantial difference in our results between two of the most recent catalogues (UCAC4 and PPMXL (Roeser et al. 2010)). We chose to use UCAC4 values, as this catalog is less affected by potential systematic uncertainties (Vickers et al. 2016).

several studies have shown that it is possible to disentangle the two components in the [α/Fe]-[Fe/H] plane. These studies include surveys of nearby stars (Fuhrmann 1998, 2004, 2008, 2011), a low-resolution study of extended solar neighbourhood G-dwarfs (Lee et al. 2011), and a number of recent high-resolution studies (Reddy et al. 2006; Adibekyan et al. 2013; Haywood et al. 2013; Bensby et al. 2014; Recio-Blanco et al. 2014; Guiglion et al. 2015; Hayden et al. 2015; Kordopatis et al. 2015b). RAVE DR4 provides abundance measurements for six elements derived from the RAVE chemical pipeline, which includes the α elements Mg, Si, and Ti. K13 suggested that Ti is not reliably measured for dwarfs, and dwarfs make up half our sample, so we use the Mg abundance measurement only.

The precision of [Mg/Fe] abundances determined with RAVE (~ 0.2 dex) is lower than that required to recover the gap between the two populations in the [α/Fe]-[Fe/H] plane: using Eq. 3 of Lindegren & Feltzing (2013), which describes the minimum separation at which two populations can be distinguished in a given sample size, we find that with our sample of 20 751 stars we could distinguish populations separated by 1.5 times the standard error in [Mg/Fe]. Hence given our error of ~ 0.2 dex in [Mg/Fe], the separation between populations needs to be at least 0.3 dex, whereas high-resolution data indicate that the separation is $\lesssim 0.2$ dex (Recio-Blanco et al. 2014; Haywood et al. 2013; Bensby et al. 2014; Kordopatis et al. 2015b). Therefore, we turn to a probabilistic approach to the separation of the α-low and α-high stars.

We write the 2D probability density function (pdf) of stars in the α-low or the α-high component as

$$f([\mathrm{Fe/H}], [\alpha/\mathrm{Fe}]) = f_{[\mathrm{Mg/Fe}]} \times f_{[\mathrm{Fe/H}]}. \tag{2.1}$$

We will refer to $f_{[\mathrm{Mg/Fe}]}$ as the α distribution function, and $f_{[\mathrm{Fe/H}]}$ as the metallicity distribution function (MDF) for a given component. The α distribution is taken to be a Gaussian with a mean and dispersion that depends on [Fe/H]:

$$f_{[\mathrm{Mg/Fe}]} = \frac{1}{\sigma_{\mathrm{Mg}}\sqrt{2\pi}} \exp\left(-\frac{([\mathrm{Mg/Fe}] - \mu_{\mathrm{Mg}})^2}{2{\sigma_{\mathrm{Mg}}}^2}\right). \tag{2.2}$$

For the thin disc, μ_{Mg} and σ_{Mg} are given by Kordopatis et al. (2015b):

$$\mu_{\mathrm{Mg,D}} = -0.2 \times [\mathrm{Fe/H}] \tag{2.3}$$

$$\sigma_{\mathrm{Mg,D}} = -0.031 \times [\mathrm{Fe/H}] + 0.07. \tag{2.4}$$

For the thick disc, μ_{Mg} and σ_{Mg} are given by:

$$\mu_{\mathrm{Mg,TD}} = \begin{cases} 0.4 & \text{for } [\mathrm{Fe/H}] < -1.0 \\ -0.25 \times [\mathrm{Fe/H}] + 0.15 & \text{otherwise} \end{cases} \tag{2.5}$$

$$\sigma_{\mathrm{Mg,TD}} = 0.075. \tag{2.6}$$

In the lower panel of Fig. 2.1 the linear dependences of μ_{Mg} on [Fe/H] are shown by the dashed lines (blue for the α-low and red for the α-high component), while the widths of the blue and red shaded regions around these lines indicate the values of σ_{Mg} for both the α-low and -high components.

Table 2.1 — Parameters for Eq. 2.7 for both thin (D) and thick (TD) disc components.

	D	TD
a_1	0.8	0.9
$\mu_{\mathrm{Fe},1}$	-0.2	-0.5
$\sigma_{\mathrm{Fe},1}$	0.18	0.2
a_2	0.15	0.08
$\mu_{\mathrm{Fe},2}$	-0.4	-0.8
$\sigma_{\mathrm{Fe},2}$	0.2	0.4
a_3	0.05	–
$\mu_{\mathrm{Fe},3}$	0.2	–
$\sigma_{\mathrm{Fe},3}$	0.5	–
X	0.85	0.14

The MDFs are too skew to be satisfactorily represented by a single Gaussian, so we represent them as weighted sums of multiple Gaussians,

$$f_{[\mathrm{Fe/H}]} = \sum_{i=1}^{n} \frac{a_i}{\sigma_{\mathrm{Fe},i}\sqrt{2\pi}} \exp\left(-\frac{([\mathrm{Fe/H}]-\mu_{\mathrm{Fe},i})^2}{2{\sigma_{\mathrm{Fe},i}}^2}\right), \tag{2.7}$$

where $n = 3$ for the thin disc and $n = 2$ for the thick disc. The means, dispersions, and weights a_i of these Gaussians for both the thin and thick disc can be found in Table 2.1. These values were extracted using the high-resolution measurements of Kordopatis et al. (2015b) as a starting point, but the shapes of the distribution were slightly modified because the shape of the MDF in any survey is affected by the survey's selection function. The top panel of Fig. 2.1 shows the adopted model MDF, using the values from Table 2.1. We do not consider a metal-rich tail for the thick disc due to ambiguity regarding the mixture of populations in the α-high, metal-rich region of the $[\alpha/\mathrm{Fe}]-[\mathrm{Fe/H}]$ plane (more details regarding potential complications due to α-high, metal-rich stars can be found later in this section as well as in Sec. 2.6).

The pdfs given by Eq. (2.1) are normalised to unity. Since there are believed to be more stars in the thin disc than the thick disc (Bland-Hawthorn & Gerhard 2016), we multiply these normalised pdfs by factors X_{TD} and X_{D} equal to the probabilities that a randomly chosen star in the sample belongs to the thick or thin disc. The values of X_{TD} and X_{D} are not accurately known. RAVE is kinematically unbiased, and as a magnitude-limited survey that extends much further than one thin-disc scale height, we expect thin and thick disc stars to enter the survey roughly in proportion to the local surface densities of the two discs. Our adopted values are based on the results of Soubiran et al. (2003), who separated the thin and thick disc populations in velocity-metallicity space. They give an estimate of $15 \pm 7\%$ for the local normalization of the thick disc and $85 \pm 7\%$ for the thin disc, where the median distance of their sample is 400 pc from the Galactic plane. The median distance of our sample is similar, so we find it appropriate to adopt these values, modifying

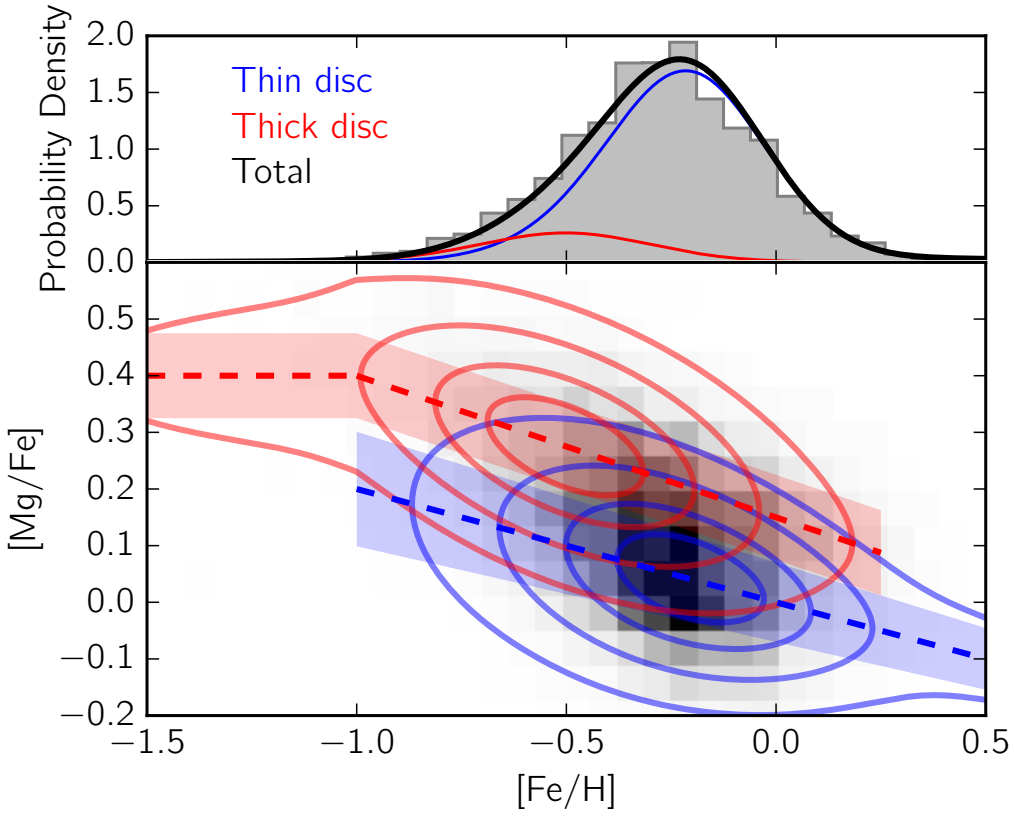

Figure 2.1 — *Top panel*: adopted metallicity distribution function (MDF). The grey-shaded histogram represents the MDF of our final sample. The thin and thick disc MDFs are shown in blue and red, respectively, and the thick black line is the sum of both disc components. *Bottom panel*: 2D histogram of our sample in [Mg/Fe]-[Fe/H] space. Contours show 33, 67, 90, and 99% of thin disc (blue) and thick disc (pink) 2D pdfs. The over-plotted dashed blue line shows the assumed mean ($\mu_{\rm Mg}$) variation as a function of [Fe/H], where the filled area represents the assumed variation in the $\sigma_{\rm Mg}$ as a function of [Fe/H], for the thin disc (Eqs. 2.3 and 2.4). Similarly, the over-plotted dashed red line shows the adopted thick disc relations (Eqs. 2.5 and 2.6).

them slightly. We use $X_{\rm TD} = 0.14$ and $X_{\rm D} = 0.85$ (see Table 2.1)[4]. Thus we assume that $\sim 1\%$ of the stars in the extended solar neighbourhood belong to the halo. We do not explicitly calculate the probability of a star belonging to the halo, however. Chen et al. (2001) note the degeneracy between local normalization and surface density ratio due to the uncertain nature of the scale heights of the discs. However, our chosen value is also a conservative estimate when considering the overall relative thin/thick disc surface density ratio (see Bland-Hawthorn & Gerhard 2016).

In order to include realistic errors for our [Fe/H] and [Mg/Fe] measurements (of the order of 0.17 dex and 0.2 dex, respectively), we generate 500 realizations of each

[4] As these values are widely disputed, we explore the effects of removing the $X_{\rm TD}$ and $X_{\rm D}$ factors from our probability computations (i.e., giving both disc components equal weight). The corresponding results can be found in Sections 2.4.1 and 2.4.2.

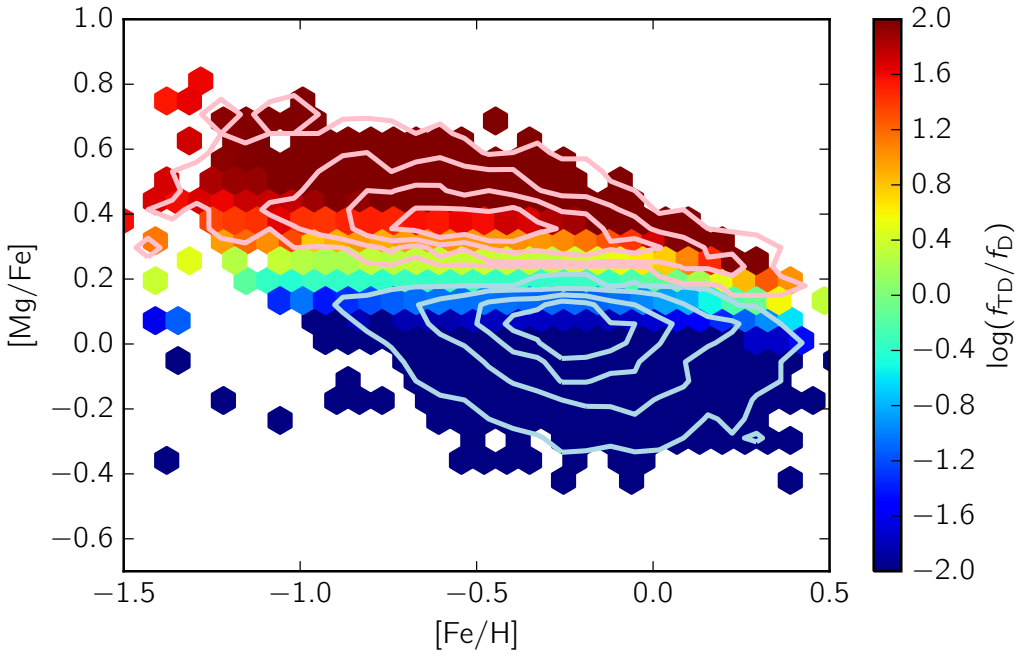

Figure 2.2 — [Mg/Fe] v. [Fe/H], where the colour of the bins represent the logarithm $\log_{10}(f_{\rm TD}/f_{\rm D})$ of the average relative probability of stars in that bin belonging to either the thick or the thin disc. Stars with a relative probability between 0.1 and 10 are not subsequently used but are included here to demonstrate the gradient in probability. The contours show 33, 67, 90, and 99% of the selected thin disc (blue) and thick disc (pink) distributions, to illustrate the gap between the two components.

star assuming a Gaussian error distribution for both measurements. The ratio of the thick disc probability to the thin disc probability ($f_{\rm TD}/f_{\rm D}$) is calculated for each realization, and the median is taken as the final $f_{\rm TD}/f_{\rm D}$ value. We assign a star as belonging to the thin disc when $f_{\rm TD}/f_{\rm D} < 0.1$. Similarly, we assign a star as belonging to the thick disc when $f_{\rm TD}/f_{\rm D} > 10$. We note that we still expect some overall contamination of incorrectly assigned stars in both disc components, of the order of 10%, due to our selection criterion ($f_{\rm TD}/f_{\rm D}$), and this contamination increases towards both ends of our metallicity distribution. This contamination may have a number of sources. Stars may be incorrectly assigned to the thick disc due to the substantial overlap in the MDF of the thin and thick disc at the metal-rich end. In addition, the precision of our abundance measurements may affect the assignment accuracy at both tails of the distribution.

Despite this contamination, we consider that the α-low component corresponds to what would typically be described as the 'thin disc', and the α-high similarly corresponds to the 'thick disc'. In the remainder, we refer to the 'thin disc' as the α-low component and the 'thick disc' as the α-high component. We adopt this definition due to certain limitations when considering the tails of [Fe/H] distribution for both the 'thin' and 'thick' disc components, where more complex population mixtures may exist (Nissen & Schuster 2010; Masseron & Gilmore 2015;

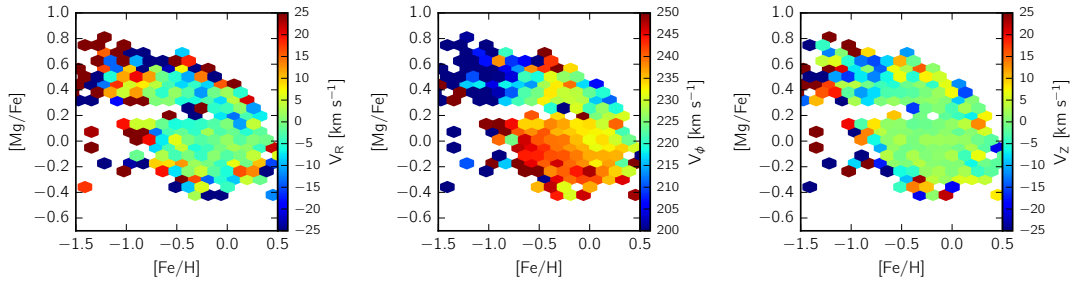

Figure 2.3 — [Mg/Fe] vs. [Fe/H], where the colour of the bins represent the average velocity of the stars in that bin, for each of the three velocity components. Here, we show only the selected stars, i.e., all stars with $0.1 < (f_{\rm TD}/f_{\rm D}) < 10$ have been removed.

Chiappini et al. 2015; Martig et al. 2015). Specifically, for the metal-rich tail of the α-high component, it is unclear if the distribution flattens (e.g. Bensby et al. 2014), or continues with a linear trend similar to our adopted distribution, eventually joining the α-low sequence. In either case, disentangling these complex population mixtures in the metal-rich tail is not possible when considering the precision of our α-abundance measurements, and therefore we consider only a conservative range of metallicities where a two-component model is viable.

Our final sample consists of 11 440 stars assigned to the α-low component and 2 251 stars assigned to the α-high component. In Fig. 2.2, we show [Mg/Fe] versus [Fe/H], with bins colour-coded according to the average probability of stars in that bin to belong to either component. The contours enclose 33, 67, 90, and 99% of the selected α-low (blue) and α-high (pink) components, to illustrate the gap between the two components.

2.4 Results

Each pixel of the [Fe/H] – [Mg/Fe] planes of Fig. 2.3 is coloured to encode the mean value of V_R, V_ϕ or V_Z for the stars in our selection that are assigned to that pixel. A clear distinction is evident between the kinematics of our selected α-low and α-high components, especially in V_ϕ.

To explore further the different kinematic trends in our chemical components, in Fig. 2.4 we show for each component the averages of V_R, V_ϕ and V_z as a function of metallicity. In the case of V_ϕ we have fitted by least-squares lines to the data points, excluding bins with less than ten objects to avoid drawing conclusions from low-number statistics. For the α-low sequence, the most metal-poor bins are also excluded as there we expect some contamination from the α-high component (see Sec. 2.3). For the α-high disc (bottom row of Fig. 2.4), we exclude the two most metal-rich bins, due to contamination from α-low stars. Bins excluded from the linear fits are plotted as open circles.

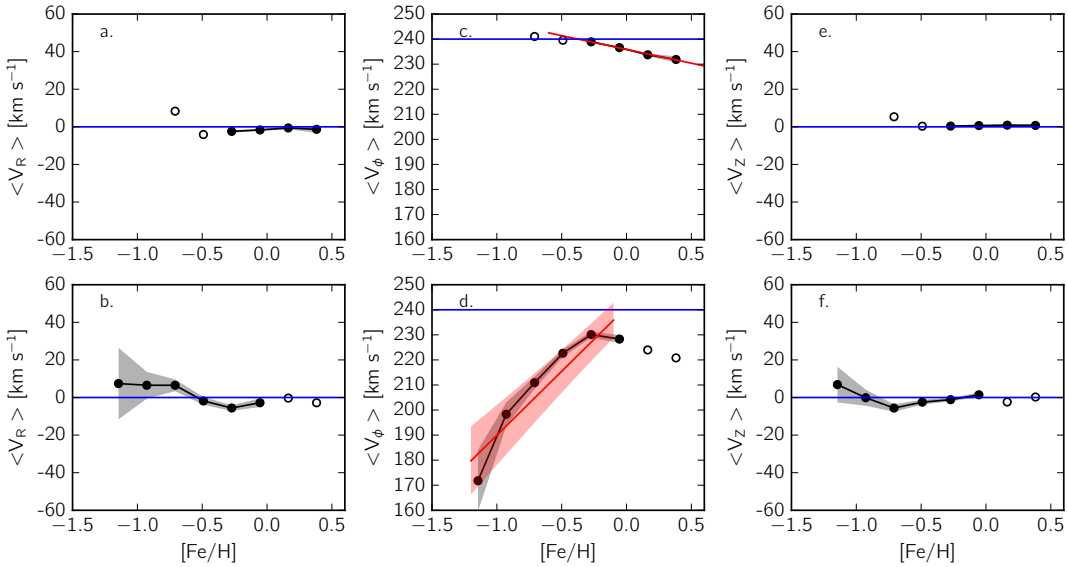

Figure 2.4 — Mean velocity as a function of [Fe/H] for the α-low component (top row), and the α-high component (bottom row). See Section 2.3 for a detailed description on how these populations are selected. Trend lines are computed by binning the data into ~0.2 dex wide [Fe/H] bins. The shaded regions correspond to the average errors for a given metallicity bin. Bins with less than 10 stars are not shown, and are not used to calculate the linear fit. Open circles denote bins which are not used in determining the linear fit in panels c and d. The red lines in panels c and d show the linear fits for the α-low and -high sequences, respectively, with the shaded red region corresponding to the error on the fit.

2.4.1 Mean rotational velocity trends for the thin and thick disc components

We find $\partial V_\phi/\partial$[Fe/H] < 0 for the α-low component but $\partial V_\phi/\partial$[Fe/H] > 0 for the α-high component. Quantitatively, for α-low stars, we find

$$\frac{\partial V_\phi}{\partial[\mathrm{Fe/H}]} = (-11 \pm 1)\,\mathrm{km\,s^{-1}\,dex^{-1}}. \tag{2.8}$$

This slope is significantly shallower than those of Lee et al. (2011) and Adibekyan et al. (2013), but using high-resolution data from *Gaia*-ESO Recio-Blanco et al. (2014) find, $\partial V_\phi/\partial$[M/H] $= (-17 \pm 6)$ km s^{-1} dex^{-1}, which lies within 1σ of our value.

For the α-high population, we measure

$$\frac{\partial V_\phi}{\partial[\mathrm{Fe/H}]} = (51 \pm 10)\,\mathrm{km\,s^{-1}\,dex^{-1}}. \tag{2.9}$$

This slope is in agreement with recent literature values. Lee et al. (2011) report a tight correlation with slope (43.4 ± 1.8) km s^{-1} dex^{-1} in their subsample of thick-disc G-dwarfs, while Kordopatis et al. (2011) find $\partial V_\phi/\partial$[M/H] $= (43 \pm 11)$ km s^{-1} dex^{-1}. Similarly, Adibekyan et al. (2013) find $\partial V_\phi/\partial$[M/H] ~ 42 km s^{-1} dex^{-1} for thick disc stars in a sample of FGK solar neighbourhood dwarfs. Our value also agrees with the

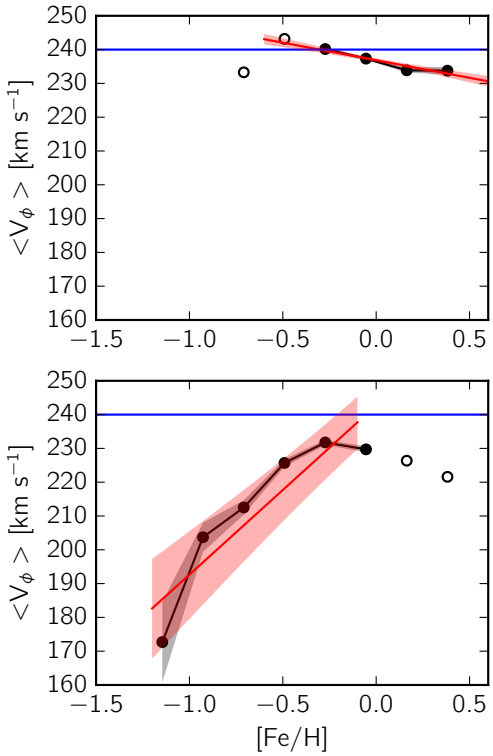

Figure 2.5 — Same as panels c and d of Fig. 2.4, but with no prior factors used in the determination of the probabilities (i.e., equal weight given to both disc components, cf. to the $X_{\rm TD}$ and $X_{\rm D}$ factors given in Table 2.1).

findings of Recio-Blanco et al. (2014), $\partial V_\phi/\partial[{\rm M/H}] = (43 \pm 13)$ km s^{-1} dex^{-1}, from a high-resolution sample of FGK stars from the *Gaia*-ESO survey.

Fig. 2.5 shows the average V_ϕ velocity as a function of [Fe/H] for the case where both discs are given equal weight (compare with panels c and d of Fig. 2.4). We measure similar trends in $\partial V_\phi/\partial$[Fe/H] as when the $X_{\rm TD}/X_{\rm D}$ prior is included, for both disc components. This further strengthens our result that we successfully determine distinct kinematics for each disc component.

2.4.2 Velocity dispersion trends

Fig. 2.6 shows for the α-low and α-high components the variation with [Fe/H] of the dispersions of V_R, V_ϕ and V_z corrected for observational uncertainties in the standard way:

$$\sigma_{\rm R,\phi,Z} = \sqrt{\sigma^{*2}_{\rm R,\phi,Z} - \langle {\rm e}_{V_{\rm R,\phi,Z}} \rangle^2} \tag{2.10}$$

where $\sigma_{\rm R,\phi,Z}$ is our corrected velocity dispersion, $\sigma^*_{\rm R,\phi,Z}$ is the measured velocity dispersion, and ${\rm e}_{V_{\rm R,\phi,Z}}$ is the error on the velocity component. In both chemical subgroups velocity dispersion tends to decrease with increasing [Fe/H], so the most metal-poor stars have the highest dispersions and SMR stars have low dispersions.

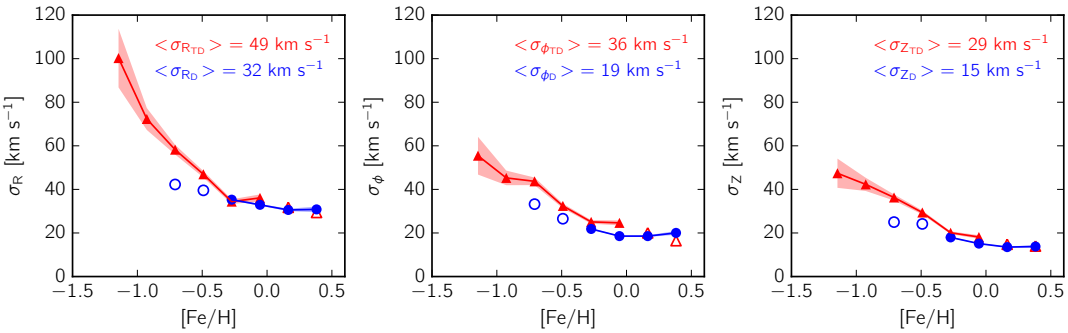

Figure 2.6 — Velocity dispersion as a function of metallicity for the α-low component (blue circles), and the α-high component (red triangles). See Section 2.3 for a detailed description on how these populations are selected. Trend lines are computed by binning the data into ~0.2 dex width bins. The shaded regions correspond to average errors for a given metallicity bin. Bins with less than 10 stars are not shown. The average $\sigma_{R,\phi,Z}$ values are given in the top right corner, for both disc components. These averages are determined using only bins with filled symbols.

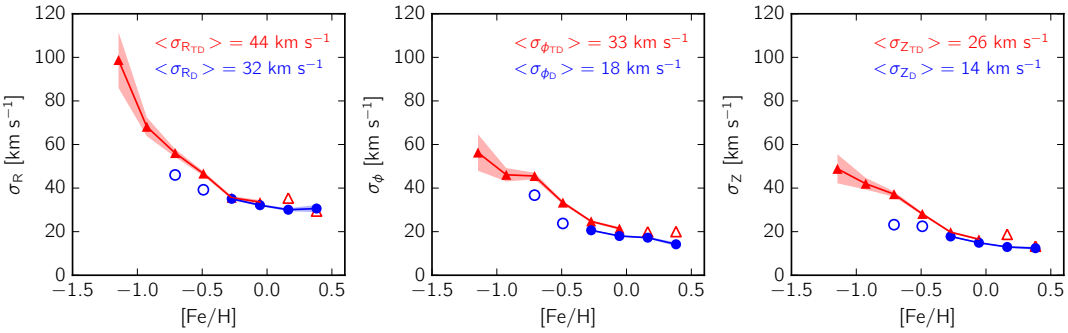

Figure 2.7 — Same as Fig. 2.6, but with no prior factors used in the determination of the probabilities (i.e., equal weight given to both disc components).

In the region $-0.2 <$ [Fe/H] < 0.0 the trends for the α-low and α-high components overlap substantially: their dispersions differ little in the two overlapping bins where both the α-low and α-high components are free of significant contamination. However, at [Fe/H] < -0.2 the values for each chemical subgroup are clearly separated. While we assume some contamination of the α-low sample in the most metal-poor bins, these bins follow approximately the same linear relation as the more metal-rich bins. We find the ratio of σ_R/σ_ϕ to be relatively constant (~ 1.6 for both components), independent of metallicity.

At the top right of each panel in Fig. 2.6 we give the mean velocity dispersion for each chemical component, calculated using only the bins that we consider free of significant contamination (i.e., avoiding the two most metal-poor bins for the α-low component, and the two most metal-rich bins for the α-high component). This gives an effective range of $-0.27 <$ [Fe/H] < 0.38 for the α-low component, and an effective range of $-1.15 <$ [Fe/H] < -0.05 for the α-high component.

For both components, our mean velocity dispersions conform to the familiar relations $\sigma_R > \sigma_\phi > \sigma_Z$ and $\sigma_Z \simeq 0.5\sigma_R$ (Quillen & Garnett 2001; Holmberg et al. 2007). In addition, we find a constant offset $\sim 16\,\mathrm{km\,s^{-1}}$between the average dispersions of the α-low and α-high sequences. This offset is consistent with the observed values of Bensby et al. (2005), which were determined using a kinematically-selected high-resolution sample of FGK dwarfs in the solar neighbourhood. As in Section 2.4.1, we consider the velocity dispersion as a function of [Fe/H] for the case where we remove the $X_{\rm TD}/X_{\rm D}$ prior from the probability calculation. The results are shown in Fig. 2.7. While the outcome is similar, we do note that the thick disc has a consistently lower mean velocity dispersion compared to the case where we include the prior. In addition, the separation between the two chemical disc components is also consistently less ($\sim 13\,\mathrm{km\,s^{-1}}$compared to when the prior is included $\sim 16\,\mathrm{km\,s^{-1}}$, cf. Figs. 2.6 and 2.7).

While the removal of the $X_{\rm TD}/X_{\rm D}$ factor does not significantly alter our results, the ratio of stars assigned to the α-high and -low components is affected adversely. The ratio of α-high to α-low stars for our final selected sample is $2251/11440 \sim 0.20$, which is within the range of conservative estimates of the thick disc fraction. In contrast, if we remove the prior, we find a ratio of $4436/7785 \sim 0.60$, which is above the high end of the range of estimates. In order to better represent physical reality as it is currently understood, we find the application of this prior desirable.

Combining the mean and dispersion of each of velocity component with the Jeans equation, we can estimate the radial scale lengths (h_R) of our chemical disc components. If we assume that the Galactic potential is dominated by a centrally concentrated mass distribution (Gilmore et al. 1989), and that the velocity ellipsoid always points toward the Galactic centre (Siebert et al. 2008; Pasetto et al. 2012; Binney et al. 2014b), we have:

$$h_R = \frac{2R\sigma_R^2}{V_c^2 - \langle V_\phi \rangle^2 + 2\sigma_R^2 - \sigma_\phi^2 - \sigma_Z^2} \ . \tag{2.11}$$

By this reckoning our α-low component has scale length $h_{R_{\rm D}} = 4.8 \pm 0.2\,\mathrm{kpc}$, and our α-high component has $h_{R_{\rm TD}} = 3.4 \pm 0.1\,\mathrm{kpc}$. Our estimates are consistent with the finding of Bovy et al. (2012c) from a sample of local dwarfs from SEGUE, that the scale length of the thin disc is more extended than that of the thick disc. When we consider the scale lengths of the discs as functions of metallicity, for the α-low component $\partial h_R/\partial[\mathrm{Fe/H}] < 0$ (i.e., the most metal-poor bins have the longest scale lengths). The scale length of the α-high component proves relatively constant, with only a slight negative trend, with increasing metallicity.

While the scale length of our α-low component is longer than that determined by Robin et al. (2003) and Jurić et al. (2008) from star counts, it lies within 2σ of high-end estimates, such as that, $h_R = (4.3 \pm 0.2)\,\mathrm{kpc}$, of Bovy et al. (2012c), who used a sample of dwarfs with [Fe/H] ~ 0. Our value of h_R for the α-high component is also larger than literature values. Using a handful of red giant stars Bensby et al. (2011) obtain $h_R \sim 2\,\mathrm{kpc}$ for the thick disc, and Bovy et al. (2015) find $h_R = (2.2 \pm 0.2)\,\mathrm{kpc}$ for an α-high population. However, we note that the values of our scale lengths depend sensitively on the adopted value for the peculiar motion of the Sun ($V_\odot$). A smaller

$V_\odot$ (e.g., the classical value of 5.25 $\mathrm{km\,s^{-1}}$(Aumer & Binney 2009)) would result in much smaller scale lengths for both discs. For a detailed discussion see Golubov et al. (2013).

Many of the previous studies cited use either dwarfs or giants for their samples, with a tendency to select only dwarfs for chemodynamical studies, as their atmospheres stay relatively constant until they leave the main sequence. Giants, on the other hand, can experience a significant amount of mixing in their atmospheres, which makes them less desirable for studies involving long dynamical timescales. As we have an equal number of dwarfs and giants in our original sample before the chemical disc selection, we investigated if these observed trends are affected when considering only dwarfs, or only giants. For both the mean velocity and velocity dispersion trends, we find no significant differences in our conclusions.

2.5 Discussion

The primary difference in the kinematics of our α-low and α-high components are the trends in mean rotational velocity as a function of [Fe/H]. We find opposite signs for $\partial V_\phi/\partial$[Fe/H] for our two chemical disc components: positive for the α-high component, and negative for the α-low component (see panels c and d of Fig. 2.4).

The α-high component exhibits the expected characteristics of asymmetric drift: as [Fe/H] and rotational velocity increase, the velocity dispersion decreases. On account of asymmetric drift, the 'thick' disc lags the LSR significantly – Bensby et al. (2005) find a lag of $46\,\mathrm{km\,s^{-1}}$ for the kinematically selected thick disc. While the value of the thick disc's lag is uncertain (cf. Chiba & Beers 2000; Fuhrmann 2004; Lee et al. 2011), positive values for $\partial V_\phi/\partial$[Fe/H] have also been observed in a number of previous studies (Lee et al. 2011; Kordopatis et al. 2011; Adibekyan et al. 2013; Recio-Blanco et al. 2014). Recio-Blanco et al. (2014) suggest that this positive trend is in agreement with the scenario described in Haywood et al. (2013) and Haywood et al. (2016): each subsequent stellar generation in the thick disc is kinematically cooler than the previous one, such that the dispersion (and therefore lag behind the LSR) decreases with increasing [Fe/H].

Haywood et al. (2013) then propose that the inner disc is formed with the properties of the most metal-rich thick disc 'layer', with quenching of star formation causing the corresponding gap found in the [α/Fe]-[Fe/H] plane. What could have caused star formation to pause at the end of the formation of the thick disc is still debated, although a few scenarios have been proposed (e.g., the formation of the bar (Haywood et al. 2016) and depletion of gas in the disc (Chiappini et al. 1997)). Star formation is then assumed to resume, albeit at a lower rate, in the thin disc (Just & Jahreiß 2010).

Our α-low component also lags the LSR, but with $\partial V_\phi/\partial$[Fe/H] negative. We propose that the SMR stars ([Fe/H] $\gtrsim 0.15$) in our α-low component have undergone significant changes in their orbital kinematics. The origin of these metal-rich stars is not immediately obvious, but it is likely that they did not form locally. In order to explain the presence of such stars, we consider various Galactic evolution mechanisms.

It has been suggested by Haywood et al. (2013) that a turbulent ISM (Brook et al. 2004; Bournaud et al. 2009) in the inner Galaxy could allow gas enrichment to reach solar metallicity within a few Gyr. SMR stars born in the inner Galaxy would then experience interactions with inhomogeneities in the primitive disc to bring them to the solar neighbourhood. However, Kordopatis et al. (2015a) note that stars formed in the early turbulent ISM would now be on highly eccentric orbits, which is not the case for most SMR stars in RAVE (see their Figs. 9 and 10). It is also possible that these stars were formed in gas clouds on non-circular orbits (e.g., from gas being accreted from outside the disc), and therefore the stars would, from birth, be on kinematically hotter orbits themselves. However, such gas is typically of sub-solar metallicity (Wakker 2001; Richter et al. 2001; Richter 2006) and therefore would most likely not give rise to the metal-rich population that we see.

Now consider the possibility that the SMR stars were born kinematically cold. If these stars were scattered onto more eccentric/inclined orbits by either the Lindblad resonances of the spiral arms or by giant molecular clouds ('blurring'), then these SMR stars in the α-low component would be visitors from the inner galaxy at the apocentres of their orbits. On this account they would lag the LSR as we observe. We find that our most metal-rich stars ([Fe/H] $\gtrsim 0.3$) lag the LSR by ~ 10 km s^{-1}. Golubov et al. (2013) argue that this asymmetric drift should also be reflected in increasing radial velocity dispersion, i.e., increasing σ_R with decreasing $\langle V_\phi \rangle$. For our α-low component, we find the trends of $\sigma_{R,\phi,Z}$ with [Fe/H] to be flat – Fig. 2.6 shows just a hint of increasing σ_R and σ_ϕ.

Although blurring may influence the relationship between chemistry, kinematics and position that we find, we still need to explain the finding of Kordopatis et al. (2015a) that SMR stars in RAVE (defined as [Fe/H] > 0.1) follow roughly circular orbits, with approximately half of these metal-rich stars having eccentricities below $e \sim 0.15$. On the other hand, churning involves an increase in angular momentum and thus guiding radius without any increase in eccentricity. As a large fraction of these SMR stars have circular orbits, we consider it likely that these stars have been brought to the solar neighbourhood largely by churning.

A number of high-resolution studies find the SMR stars in the α-low component have a relatively small spread in [Mg/Fe] (Recio-Blanco et al. 2014; Bensby et al. 2014; Kordopatis et al. 2015b; Haywood et al. 2013) and we find a slight indication of this at the SMR tail of our α-low component. This scenario is consistent with the model presented in Nidever et al. (2014), according to which the α-low component arises by superposition of populations with differing star formation histories. This manifests as a relatively narrow sequence of α-low stars over a large [Fe/H] range. Nidever et al. (2014) note that a possible origin of this effect is described in Schönrich & Binney (2009a), where the superposition of populations is caused by radial migration of stars from the inner Galaxy with different birth radii and enrichment histories. While they find that stars may experience both blurring and churning, the effect of churning is stronger in the inner regions of the galaxy, where SMR stars were most likely born. Therefore, we also consider that both mechanisms may be at work. If a star is first blurred such that it is at larger Galactic radii, it is possible that it may then experience a change in guiding radius due to an interaction with a varying non-axisymmetric potential at corotation, such as transient spiral arms (Sellwood

& Binney 2002), or transient overdensities at the bar-spiral interface (Minchev et al. 2013). While it is possible for both mechanisms to alter the kinematics of a given star, Minchev et al. (2013) note that stars on circular orbits are more likely to be affected by churning.

2.6 Summary and conclusions

We have explored the relationship between kinematics and elemental abundances for a sample of extended solar neighbourhood stars obtained by RAVE. Since high-resolution studies (e.g. Recio-Blanco et al. 2014; Haywood et al. 2013; Bensby et al. 2014; Kordopatis et al. 2015b) have shown that the trough in the [Fe/H]$-$[α/Fe] plane between the α-low and α-high components of the Galactic disc is narrower than the uncertainties in [α/Fe] in the RAVE survey, we have identified the RAVE stars that are most and least likely to be members of the α-low component. Specifically, a star enters our α-low sample if its location in the [Fe/H] $-$ [α/Fe] plane is made ten times more probable by the hypothesis that it belongs to the α-low component than the hypothesis that it belongs to the α-high component. Conversely, the locations of our α-high stars are ten times more probable under the hypothesis that they belong to the α-high component than under the hypothesis that they belong to the α-low component. With this probabilistic separation criterion, we successfully determine separate kinematics for the α-low and -high populations, for a conservative metallicity range where a two-component model is plausible. In addition, we find cool, thin-disc-like kinematics for the majority of our sample above solar metallicity.

For the α-low sequence, we find a negative trend in the mean rotational velocity as a function of metallicity: $\partial V_\phi/\partial$[Fe/H] = (-11 ± 1) km s^{-1} dex^{-1}, which is a shallower gradient than those measured by high-resolution studies of the solar neighbourhood. For the α-high component, we find a positive correlation of mean rotational velocity with metallicity: $\partial V_\phi/\partial$[Fe/H] = (51 ± 10) km s^{-1} dex^{-1}, which agrees with results from both low- and high-resolution surveys.

Although a faint signature of this trend can be seen in the metal-rich bins of α-high sequence (open symbols in panel d of Fig. 2.4), we note that this may be due to contamination by α-low stars arising from the large errors in [Fe/H]. Also at the high-[Fe/H] end we notice a relative overabundance of α-high stars. A similar population of α-high, metal-rich stars was detected by Gazzano et al. (2013), who concluded that these objects probably belong to the thin disc. By contrast, Masseron & Gilmore (2015) consider it uncertain whether these stars should be assigned to the thin or thick disc on the grounds that these stars may have a variety of origins. Furthermore, it is possible that some of these α-high stars are young (Chiappini et al. 2015; Martig et al. 2015), which suggests that they are part of the thin disc (however, see Jofré et al. 2014 for a discussion on the existence of this population). For these reasons, we do not consider the kinematics of the SMR ([Fe/H] $\gtrsim 0.15$) stars in the α-high component.

The α-low and α-high components follow different trends for all three components of the velocity dispersion. While the velocity dispersions of the chemical disc

components are similar in the metallicity regime $-0.2 < [Fe/H] < 0.0$, there are significant differences at the metal-poor end. The mean dispersion of a given velocity component is $\sim 16 km\,s^{-1}$less for α-low stars than α-high stars. Notwithstanding some contamination of one component by the other, our chemically separated components exhibit markedly different kinematics, which are consistent with the trends found using higher resolution data.

RAVE offers a unique statistical opportunities to constrain theories of Galaxy evolution. While high-resolution surveys will have a very small overlap with Gaia DR1, $\sim 3 \times 10^5$ RAVE stars are expected to be in Gaia DR1. Hence RAVE data combined with more accurate parallaxes and proper motions from Gaia DR1 should significantly sharpen, and hopefully confirm, the chemodynamical trends reported here and enable us to track more securely the extent and effect of radial migration in the Galactic discs.

Acknowledgements. We thank the referee for their thorough comments and suggestions which have helped improve the quality of the manuscript. We also thank Philipp Richter, Ivan Minchev, Friedrich Anders, Cristina Chiappini, and Else Starkenburg for their comments and helpful discussions, which have improved the quality and clarity of the text. Funding for this work and for RAVE has been provided by: the Australian Astronomical Observatory; the Leibniz-Institut für Astrophysik Potsdam (AIP); the Australian National University; the Australian Research Council; the European Research Council under the European Union's Seventh Framework Programme (Grant Agreement 240271 and 321067); the French National Research Agency; the German Research Foundation (SPP 1177 and SFB 881); the Istituto Nazionale di Astrosica at Padova; The Johns Hopkins University; the National Science Foundation of the USA (AST-0908326); the W. M. Keck foundation; the Macquarie University; the Netherlands Research School for Astronomy; the Natural Sciences and Engineering Research Council of Canada; the Slovenian Research Agency; the Swiss National Science Foundation; the Science & Technology Facilities Council of the UK; Opticon; Strasbourg Observatory; and the Universities of Groningen, Heidelberg and Sydney. The RAVE web site is at https://www.rave-survey.org.

3 The selection function of the RAVE survey

Jennifer Wojno, Georges Kordopatis, Tilmann Piffl, James Binney, Matthias Steinmetz, Gal Matijevič, Joss Bland-Hawthorn, Sanjib Sharma, Paul McMillan, Fred Watson, Warren Reid, Andrea Kunder, Harry Enke, Eva K. Grebel, George Seabroke, Rosemary F. G. Wyse, Tomaž Zwitter, Olivier Bienaymé, Kenneth C. Freeman, Brad K. Gibson, Gerry Gilmore, Amina Helmi, Ulisse Munari, Julio F. Navarro, Quentin A. Parker, Arnaud Siebert

— Published as J. Wojno et al., 2017, MNRAS 468, 3368 —

ABSTRACT

We characterize the selection function of RAVE using 2MASS as our underlying population, which we assume represents all stars which could have potentially been observed. We evaluate the completeness fraction as a function of position, magnitude, and colour in two ways: first, on a field- by-field basis, and second, in equal-size areas on the sky. Then, we consider the effect of the RAVE stellar parameter pipeline on the final resulting catalogue, which in principle limits the parameter space over which our selection function is valid. Our final selection function is the product of the completeness fraction and the selection function of the pipeline. We then test if the application of the selection function introduces biases in the derived parameters. To do this, we compare a parent mock catalogue generated using GALAXIA with a mock-RAVE catalogue where the selection function of RAVE has been applied. We conclude that for stars brighter than I = 12, between 4000K < $T_{\rm eff}$ < 8000K and 0.5 < $\log g$ < 5.0, RAVE is kinematically and chemically unbiased with respect to expectations from GALAXIA.

3.1 Introduction

In any statistical analysis it is fundamental to understand the relation between the objects for which data were obtained, and the underlying population from which the sample was drawn. This relation is called the selection function of the sample. Without this knowledge, it is difficult to accurately infer the general properties of a population.

Many large-scale astronomical surveys of Milky Way stars with data releases currently or soon available make some effort to characterize their selection function. The explicit quantification of the selection function of a stellar survey has been demonstrated by Schönrich & Binney (2009b) for the Geneva-Copenhagen survey (GCS; Nordström et al. 2004), Bovy et al. (2012c) for a sub-sample of the Sloan Extension for Galactic Understanding and Exploration survey (SEGUE; Yanny et al. 2009), Nidever et al. (2014) for the APO Galactic Evolution Experiment (APOGEE; Majewski et al. 2015), and Stonkutė et al. (2016) for the Gaia-ESO survey (Gilmore et al. 2012). A number of factors such as changes to the observing strategy, limitations due to instrumentation, or including different input catalogues can all affect the final resulting catalogue, so it is crucial to consider each of these aspects when characterising the selection function.

In this article we present a study of the selection function of the RAdial Velocity Experiment (RAVE) survey based on its most recent data release (DR5; Kunder et al. 2017), to facilitate the wider and more robust use of this publicly-available catalogue. This survey was among the first surveys in Galactic astronomy with the explicit purpose of producing a homogeneous and well-defined data set. To achieve this goal, the initial target selection was based purely on the apparent I-band magnitudes of the stars.

Based on the simplicity of the selection function a number of recent studies using RAVE data, reviewed in Kordopatis (2015), assumed the RAVE survey to be a kinematically unbiased sample to investigate models of our Galaxy. In particular, Sharma et al. (2014) briefly addressed the selection function with respect to ensuring their subsample was unbiased, by mimicking the target selection of RAVE directly using Monte Carlo realisations of their Galaxy models. However, here we aim to characterize the selection function of all stars available in DR5.

We present a short overview on the RAVE survey in Section 3.2, summarising the history of the survey with respect to the target selection and observing strategy. Our reduced sample for evaluating the selection function is described in Section 3.3. In Section 3.4 we present our results for two different ways of evaluating the selection function: field-by-field and by HEALPIX pixel. Then in Section 3.4.3 we incorporate the effects of the spectral analysis pipeline on the final catalogue. In Section 3.5, we present the method for generating our mock-RAVE catalogue, and compare it to a sample of RAVE DR5 stars. We then test for biases due to the selection function of RAVE, by comparing our mock-RAVE catalogue with a parent GALAXIA sample. Finally, we discuss the implications of these findings and our conclusions in Section 3.6.

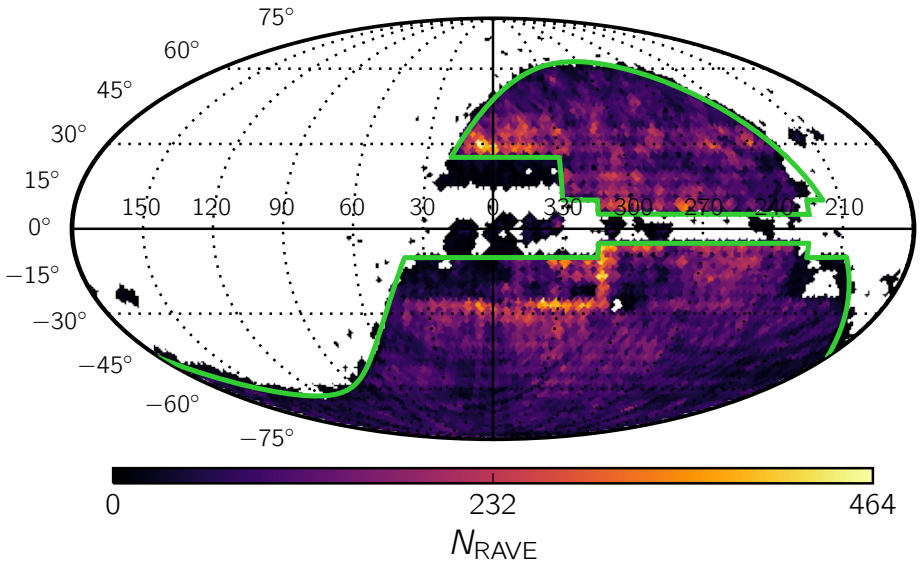

Figure 3.1 — All RAVE DR5 targets in Galactic coordinates, colour-coded by number of stars in a given HEALPIX pixel (NSIDE = 32, area $\simeq 3.31\,\mathrm{deg}^2$, see also Sec. 3.4.2). The adopted footprint (described in Sec. 3.2.3) is shown in green. In this study we only consider stars within the footprint.

3.2 The RAVE survey

RAVE is a large-scale spectroscopic stellar survey of the Southern hemisphere conducted using the 6dF multi-object spectrograph on the 1.2-m UK Schmidt Telescope at the Siding Spring Observatory in Australia, and completed in 2013. A general description of the project can be found in the data release papers (DR1; Steinmetz et al. 2006; DR2; Zwitter et al. 2008; DR3; Siebert et al. 2011b; DR4; Kordopatis et al. 2013a) as well as in the most recent data release paper (DR5; Kunder et al. 2017). We show the distribution of targets available in RAVE DR5 in Figure 3.1.

The spectra were taken in the Ca II-triplet region (8410 – 8795 Å) with an effective spectral resolution of $R \approx 7500$. The strong calcium absorption lines allow a robust determination of the line-of- sight velocities via the Doppler effect even with low signal-to-noise ratio (SNR) ($\lesssim 10$ per pixel). This region was explicitly chosen to coincide with the spectral range of Gaia's Radial Velocity Spectrometer (RVS) (Prusti 2012; Bailer-Jones et al. 2013; Recio-Blanco et al. 2016). While Gaia will release radial velocity and stellar parameters in forthcoming data releases, at present Gaia offers only position and magnitude information for approximately a billion stars (Gaia Collaboration et al. 2016). The Tycho-Gaia astrometric solution (TGAS; Michalik et al. 2015) provides parallax and proper motion data for ~ 2 million stars which were observed by Tycho-2 (Høg et al. 2000). As RAVE contains 215 590 unique TGAS stars,

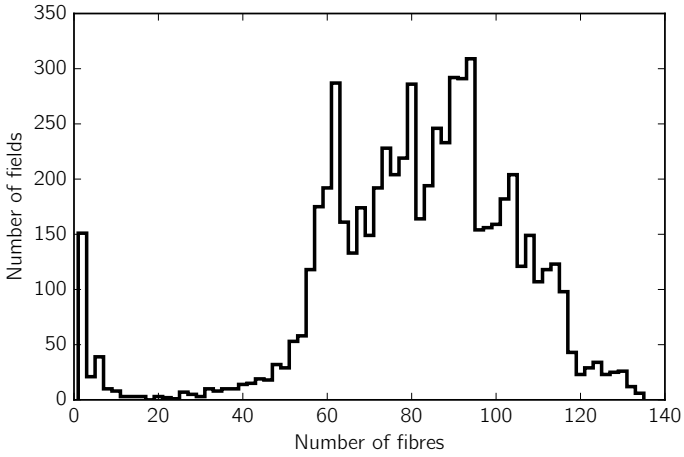

Figure 3.2 — Histogram of the number of fibres placed for each pointing (bin width = 2), for the entire duration of the RAVE survey (2003-2013). For each pointing, at least one fibre was placed.

it offers a unique advantage of providing stellar parameters for stars with improved parallax and proper motion data from TGAS.

3.2.1 Input catalogue

When observations for the RAVE survey started in 2003 there was no comprehensive photometric infrared survey available to serve as an input catalogue. Instead, approximate I-band magnitudes were calculated from the Tycho-2 catalogue and the SuperCOSMOS Sky Survey (SSS; Hambly et al. 2001), and used to construct an initial input catalogue of ~300 000 stars. In May 2005, the DENIS catalogue (Epchtein et al. 1999) became available which provided Gunn I-band photometry, however, it did not provide sufficient sky coverage to serve as the sole basis for the input catalogue. RAVE DR1, DR2, and DR3 were sourced from the original input catalogue (Kordopatis et al. 2013a).

The fourth data release, DR4 (Kordopatis et al. 2013a), incorporated observations drawn from a new input catalogue, using DENIS DR3 (DENIS Consortium 2005) as the basis, which had been cross-matched with the 2MASS point source catalogue (Skrutskie et al. 2006). The new input catalogue also extended the RAVE footprint to include lower Galactic latitudes ($5^\circ < |b| < 25^\circ$), where a colour cut using 2MASS photometry ($J-K > 0.5$ mag) was applied to preferentially select giants (Kordopatis et al. 2013a). This input catalogue is also used for the most recent data release (DR5; Kunder et al. 2017).

3.2.2 Target selection and observing strategy

Here we summarise the target selection and observing strategy described in the first data release (DR1, Steinmetz et al. 2006), as the selection function of a survey depends explicitly on how the observations are conducted.

From the input catalogue described in the previous section, 400 targets were selected for a given field of view. This selection was then split into two field files consisting of 200 stars each, to allow for two separate pointings. The 6dF instrument, used to conduct RAVE observations, consists of three fibre plates with 150 fibres each. These fibres were assigned to science targets according to a field configuration algorithm developed for the 2dF spectrograph (Lewis et al. 2002). However, for various reasons such as inaccessible areas on the fibre plate and fibre breakage, on average approximately 90 science fibres were allocated per pointing. Each observation consisted of a minimum of 3 (average 5) exposures, which were then stacked to improve the SNR per pointing. Figure 3.2 shows the distribution of fibres placed on science targets present in DR5 for all fields in the master list of RAVE field centres (see Sec. 3.4.1).

During the first year and a half of observations, no blocking filter was used on the spectrograph, so spectra were contaminated with second order diffraction (i.e., flux from the $\sim 4200-4400$Å wavelength range entered the primary wavelength range). Therefore, in DR5 the automated stellar parameter pipeline does not give stellar parameters for observations made before 6 April 2004.

A problem with fibre cross-talk due to bright ($I \sim 9$) stars adjacent to fainter stars was also identified in the period before DR1, and corrected for in the first iteration of the data reduction pipeline (Steinmetz et al. 2006). Therefore, in March 2006, the observing strategy was modified to observe stars only in a given magnitude bin for each pointing. These magnitude bins are illustrated in Figure 3.3 as vertical dashed lines. In addition to reduced fibre cross-talk, this change in the observing strategy had the added benefit of optimizing exposure times (e.g. bright fields could be observed in nominal conditions, while faint fields were preferentially observed when conditions were excellent), increasing the SNR per spectrum, and therefore resulting in more accurate stellar parameters. For fields in which interlopers or stars with variable brightness affected the fibres despite the magnitude selection, assessment and data reduction was conducted on a case-by-case basis to minimise the probability that problematic stars would enter the final catalogue.

3.2.3 Survey footprint

A simple footprint was imposed for observations: pointings were restricted to the Southern hemisphere and $|b| > 25°$. RAVE generally avoided regions on the sky with large extinction, i.e., close to the Galactic disc and towards the bulge. The primary reason for avoiding low Galactic latitudes was to prevent multiple stars entering a fibre, which had a spatial extent of $7''$ on the sky. Exceptions were a number of calibration fields around $|b| = 0°$ and several targeted observations of open clusters in the Galactic plane. In addition, there are a few fields in regions at the northern side of the bulge that originate from an interim input catalogue. We exclude these

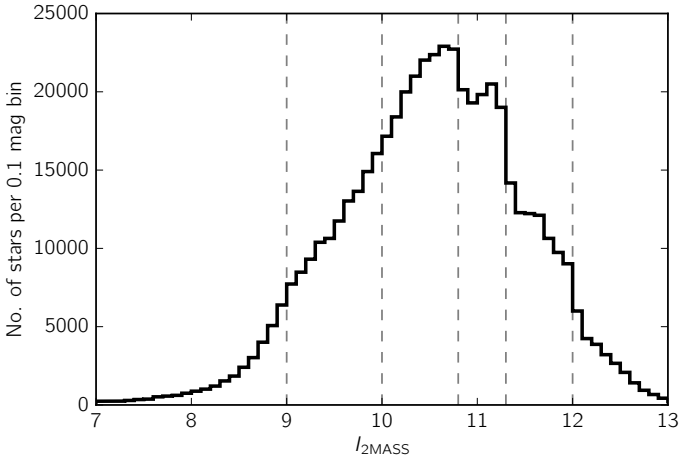

Figure 3.3 — Distribution of I-magnitudes in the full RAVE DR5 catalogue. Dotted lines mark the border of the magnitude bins used for observing runs after March 2006. The histogram shows I_{2MASS} magnitudes which are computed from the 2MASS J and K_s magnitudes, but present a homogeneous database.

fields when evaluating the completeness of RAVE, as the target selection in these fields differed from the general selection procedure.

In addition, we note the impact of utilizing DENIS DR3 as an input catalogue. The DENIS survey was observed in strips of 30° in declination and 12 arcmin in right ascension, with an overlap of 2 arcmin between consecutive strips. This observing pattern is embedded in the formulation of the selection function as a function of position (Eq. 3.1), and therefore is considered when evaluating both the completeness and selection function.

Figure 3.1 shows the adopted survey footprint for this study, which differs from the original footprint used for observations, as well as the distribution of individual stars in DR5.

3.2.4 RAVE Data Release 5

The latest public data release, DR5, contains information from 520 781 measurements of 457 588 individual stars. The distribution on the sky of these stars can be found in Figure 3.1. In addition to obtaining precise line-of-sight velocities $V_{\rm los}$ (typical uncertainties $\sim$ 2 km s^{-1}), RAVE DR5 provides several other stellar parameters derived from the spectra: effective temperature ($T_{\rm eff}$), surface gravity ($\log g$), an overall metallicity ([M/H]), and individual abundances for six elements: magnesium, aluminium, silicon, titanium, iron, and nickel.

Line-of-sight distances for RAVE stars have been estimated using a number of methods, including red-clump giants (e.g. Siebert et al. 2008; Veltz et al. 2008; Williams et al. 2013), isochrone fitting (e.g. Zwitter et al. 2010; Breddels et al. 2010), and a robust Bayesian analysis method described in Burnett & Binney (2010). RAVE DR5 provides distances derived using the method described in Binney et al.

(2014a), where stellar parameters, along with known positions, are used to derive spectrophotometric distance estimates for a large fraction of the stars in the survey.

In addition, Matijevič et al. (2012) performed a morphological classification of the spectra to allow for the identification of spectroscopic binaries and other peculiar stars in the catalogue. All targets in DR5 were also cross-matched with a number of other data sets: Tycho-2 (Høg et al. 2000), UCAC4 (Zacharias et al. 2013), PPMXL (Roeser et al. 2010), 2MASS (Cutri et al. 2003), WISE (Wright et al. 2010), APASS (Munari et al. 2014), and Gaia DR1 (Gaia Collaboration et al. 2016) to provide additional information such as proper motions, as well as apparent magnitudes in other filter passbands.

3.3 Catalogue description and quality flags

The RAVE survey was designed to have as simple a selection function as possible, to ensure that any biases could be accurately quantified. The initial target selection was based only on the apparent I-band magnitude ($9 \lesssim I \lesssim 12$) and sky position. An I-band selection was chosen as the most appropriate for efficient use of the spectral range of the 6dF instrument. In Figure 3.3 we show the distribution of I-band magnitudes in RAVE DR5. This distribution extends past the initial apparent magnitude limits due to uncertainties in the SSS photometry used for the first input catalogue (see Figure 4 of Steinmetz et al. 2006). During 2006, the angular footprint was expanded to include regions close to the Galactic disc and bulge (Galactic latitude $5° < |b| < 25°$) as a result of the new input catalogue (see Section 3.2.1), and in these new regions a colour criterion ($J - K_s \geq 0.5$) was imposed to select for cool giant stars over more prevalent dwarfs (Kordopatis et al. 2013a). We can thus assume that the probability, S, of a star being observed by the RAVE survey is

$$S \propto S_{\rm select}(\alpha, \delta, I, J - K_s), \tag{3.1}$$

with α and δ denoting the equatorial coordinates of stars in a given region on the sky, within the defined footprint (see Figure 3.1).

Due to its complex history, and owing to observational constraints and actual atmospheric conditions on the respective day, the input catalogue for RAVE carries some inhomogeneity, and it is therefore not straightforward to construct a valid parent sample from this variety of data sets. However, one data set in particular, 2MASS, offers complete coverage of both the survey area and the magnitude range of RAVE. Therefore, we adopt the 2MASS photometry in order to compare our RAVE targets with as homogenous a sample as possible.

2MASS provides accurate J, H and K_s photometry for nearly all RAVE targets and, equally important, also for all other stars which could have potentially entered the input catalogue. Unfortunately, 2MASS does not provide I-band photometry, which is needed to construct our selection function (Eq. 3.1)[1], but we can compute

[1] Recently, data from the APASS survey (Munari et al. 2014) became available which provides SDSS i magnitudes, but this survey also suffers some saturation problems for bright stars. Currently, APASS is being extended to brighter magnitudes, so in the future this could be a valuable alternative to 2MASS.

Table 3.1 — Quality criteria for the 2MASS parent sample.

Criterion	Requirement	Description
`ph_flag`$_J$	A,B,C or D	good J-photometry
`ph_flag`$_{K_s}$	A,B,C or D	good K_s-photometry
`cc_flag`$_J$	0	no artifact/confusion
`cc_flag`$_{K_s}$	0	no artifact/confusion
`gal_contam`	0	not contaminated by extended source
`pm_flag`	0	not associated with asteroid/comet

an approximate $I_{\rm 2MASS}$ magnitude via the following formula:

$$I_{\rm 2MASS} - J = (J - K_s) + 0.2 \exp \frac{(J - K_s) - 1.2}{0.2} + 0.12 \tag{3.2}$$

Eq. 3.2 is derived by a direct comparison of 2MASS J and K_s magnitudes with DENIS I magnitudes. This transformation is determined by a polynomial fit in $I - J$ versus $J - K_s$, and is an evolution of Eq. 24 in Zwitter et al. (2008), with an improved fit for very cool stars. The distribution of $I_{\rm 2MASS}$ magnitudes for RAVE DR5 is shown in Figure 3.3. Here, we find a significant number of RAVE stars which have $I_{\rm 2MASS} < 9$. We note that this is due to the fact that both DENIS and SuperCOSMOS saturate around $I_{\rm DENIS} \sim 9$, and the conversion of their cross-matched 2MASS magnitudes gives magnitudes brighter than $I_{\rm 2MASS} \sim 9$.

In addition, there are a number of other factors which also have an influence on the final selection function, which we will describe in the following sections.

3.3.1 Sample selection

RAVE quality criteria

To asses the completeness $S_{\rm select}$ (Eq. 4.1), we remove fields which were reprocessed during the course of data reduction (indicated in DR5 with either 'a','b', or 'c' appended to the `RAVE_OBS_ID`). After removing these stars, we are left with a sample of 518 079 entries in DR5, corresponding to 455 626 individual spectra.

2MASS quality criteria

We compute an $I_{\rm 2MASS}$ value (Eq. 3.2) for each 2MASS star and clean the data from spurious measurements. Our requirements for a 'valid' measurement are given in Table 3.1.

Table 3.2 — Completeness fraction of RAVE on a field-by-field basis, for 0.1 mag width bins.

							Completeness Fraction (I_{2MASS})					
RAVE Field Index	Field Centre (α, δ)	Observation Date YYYYMMDD	Fibres Placed N	Spectra N	2MASS N	0.0	...	9.9	10.0	10.1	...	14.0
0	(143.20, -8.75)	20030412	124	121	14170	-		0.0	0.0	0.0		0.00017
...												
1077	(181.67, -7.27)	20060418	93	93	7915	-		0.333	0.391	0.273		0.0
1078	(209.60, -26.43)	20060418	96	96	16382	-		0.167	0.156	0.156		0.0
...												
6430	(222.48, -44.90)	20130404	86	85	69564	-		0.0	0.0	0.0		0.0

Table 3.3 — Completeness fraction of RAVE on a pixel-by-pixel basis, for 0.1 mag width bins. Here, the nested scheme is used to determine a given pixel ID.

	Completeness Fraction (I_{2MASS})						
HEALPIX Pixel ID Index (Nested)	0.0	...	9.9	10.0	10.1	...	14.0
0	-		0.200	0.667	0.600		0.0
⋮							
10000	-		0.250	0.462	0.500		0.0
10001	-		0.571	0.500	0.250		0.0
⋮							
12287	-		0.333	0.333	0.600		0.0

3.4 The selection function

3.4.1 Field-by-field

We first consider the selection function of RAVE on a field-by-field basis, in order to account for changes in the observing strategy as a function of time.

First, the observation date and position for each individual pointing is identified from a master list of RAVE field centres and their corresponding given `RAVE_OBS_ID`. In order to make the most accurate comparison between RAVE and our parent 2MASS sample, we must utilize accurate field centre positions. We identify 6593 individual pointings from this master list, corresponding to 1598 unique field centres. Next, we compare this list with a table containing information about the placement of fibres for each pointing. For each pointing, we count the number of fibres placed on science targets, as well as how many fibres were assigned to the sky, or simply not used. As shown in Figure 3.2, out of the 150 available fibres on 6dF, at maximum approximately 130 fibres were placed per field pointing, with an average of approximately 90 fibres per RAVE pointing. From the fibres placed on science targets, we then consider how many of these observations obtained spectra for which stellar parameters are published in DR5, and characterize the I_{2MASS} distribution by counting the number of stars per 0.1 dex magnitude bin. Then, for each RAVE pointing we determine the number of 2MASS stars available in each magnitude bin, with the quality criteria described in Sec. 3.3.1 applied. For the final table (Table 3.2), we include only those fields which have stars parametrized and published in DR5.

An excerpt of the resulting completeness fraction on a field-by-field basis can be found in Table 3.2. The completeness fraction for a field centred on (α, δ) is given by

$$S_{\rm select}({\rm field}_{\alpha,\delta}) = \frac{\sum\sum {\rm N_{RAVE}}({\rm field}_{\alpha,\delta}, {\rm I}, {\rm J}-{\rm K_s})}{\sum\sum {\rm N_{2MASS}}({\rm field}_{\alpha,\delta}, {\rm I}, {\rm J}-{\rm K_s})}, \tag{3.3}$$

where the double sum is over a given I_{2MASS} range and the total $J-K_s$ range in that field.

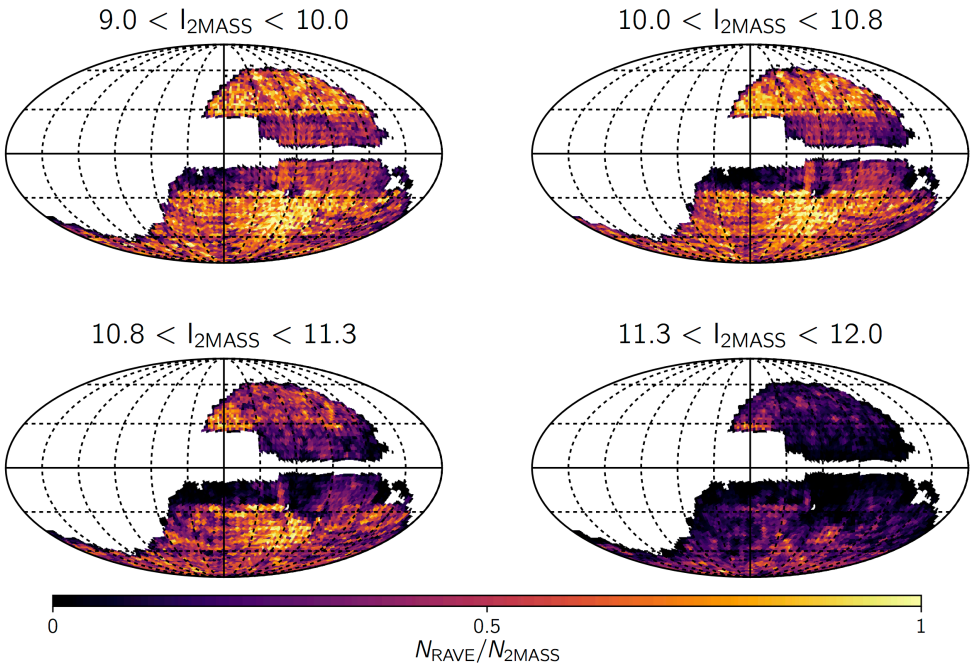

Figure 3.4 — Completeness of RAVE DR5 in Galactic coordinates as a function of observed magnitude bins (compare with similar plot for completeness fraction of DR4, Figure 3 of Kordopatis et al. 2013a). The HEALPIX pixels are colour-coded by the fractional completeness, ($N_{\rm RAVE}/N_{\rm 2MASS}$).

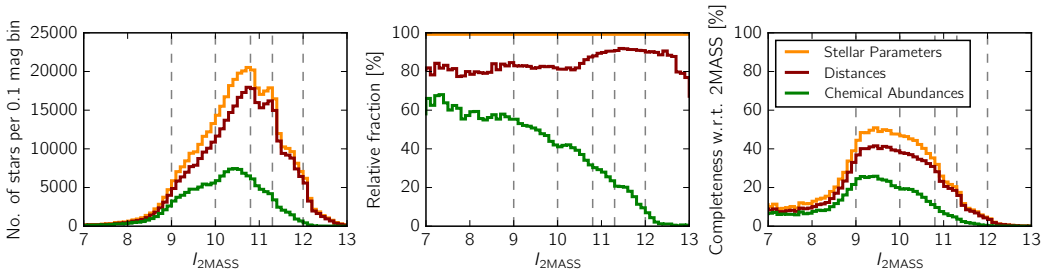

Figure 3.5 — *Left:* Histogram of stellar parameters, chemical abundances, and distance measurements in RAVE DR5 which satisfy the quality criteria and parameter limits given in Section 3.4.3, as a function of magnitude ($S_{\rm pipeline}$, Eq. 3.6). Stars with stellar parameters are indicated in orange, distances in red, and chemical abundances in green. Observed magnitude bins are indicated with dashed lines. *Middle:* relative fraction of stars with derived parameters as a function of magnitude. We use radial velocity as a baseline for comparison, as all stars satisfying the criteria given in Section 3.4.3 have radial velocity measurements. As all stars with radial velocities in this sample also have stellar parameters, the completeness of stellar parameters is 100 per cent. *Right:* completeness fraction of derived parameters, relative to the number of 2MASS stars, as a function of magnitude. This represents the complete selection function with respect to 2MASS (see Eq. 3.7).

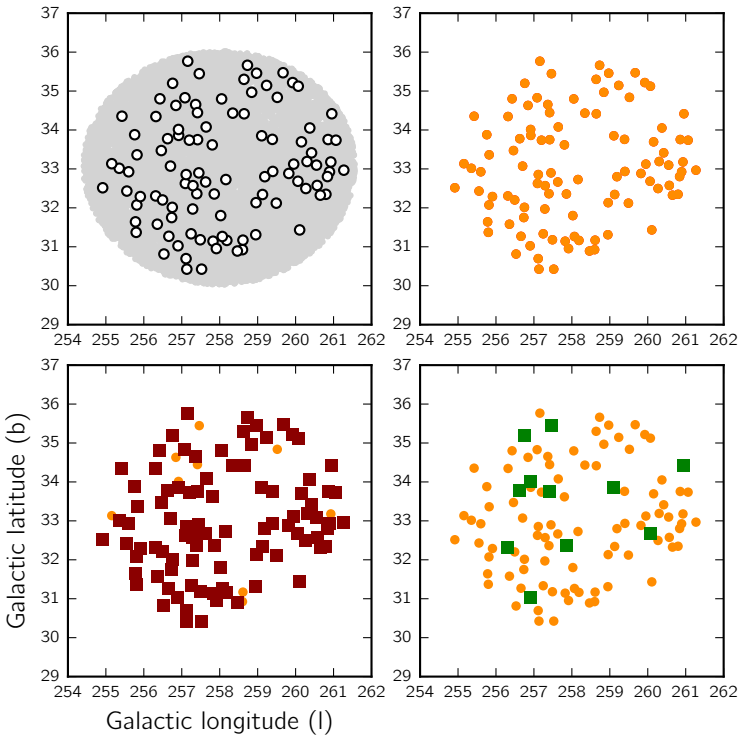

Figure 3.6 — Distribution of RAVE stars (open circles) and 2MASS (grey) stars on the sky, for a given RAVE pointing. Orange indicates that a given RAVE star has spectral parameters from the spectral parameter pipeline ($T_{\rm eff}$, log$g$, [M/H]), red squares indicate stars which have distance estimates from the distance pipeline, and green squares indicate stars which have all abundance measurements from the chemical abundance pipeline.

It is important to note that there exists substantial overlap between RAVE pointings, and therefore it is not appropriate to combine the data given in Table 3.2 to construct a selection function for the entire RAVE survey. In order to facilitate this, we must consider the completeness of RAVE for equal, discrete areas on the sky. We do note however, that on scales below the size of the field plate ($\simeq 28.3\,{\rm deg}^2$), we expect inhomogeneities due to certain technical constraints with fibre positioning on the field plates used for RAVE observations (see Figure 3 of Steinmetz et al. 2006).

3.4.2 Equal area on the sky (HEALPIX)

To construct our parent RAVE sample for considering equal areas on the sky, we first remove all repeat observations and keep for each star only the observation with the highest SNR. This is in contrast to Section 3.4.1, where we do not remove duplicates. Here, the goal is not to conserve the temporal information, but to accurately reconstruct the sky coverage and completeness of RAVE, so any given star is counted only once, even if it was observed multiple times. In addition, for the rest of the study we will only consider stars within the adopted footprint (Fig. 3.1). This

excludes ~ 7000 stars available in RAVE DR5. These specific stars are documented in the RAVE DR5 catalogue with `FootPrint_Flag`.

We then divide the sky into equal area pixels using the HEALPIX algorithm (Górski et al. 2005). As described in the previous section, using the RAVE fields directly would cause additional complications for certain applications because some fields are overlapping. We use 12 288 pixels for the whole sky (NSIDE = 32) which results in a pixel area of $\simeq 3.36\,\mathrm{deg}^2$, much smaller than the size of a RAVE field ($\simeq 28.3\,\mathrm{deg}^2$). We note that we use the 'nested'[2] scheme and equatorial coordinates (α,δ) to determine the corresponding pixel ID for any given star. We count the number of RAVE stars, N_{RAVE}, in each pixel (centred on α and δ) as a function of I_{2MASS} in 0.1 dex magnitude bins. To estimate the completeness we follow the same procedure for all stars in our 2MASS sample to obtain N_{2MASS} and then compute

$$S_{\mathrm{select}}(\mathrm{pixel}_{\alpha,\delta}) = \frac{\sum\sum \mathrm{N_{RAVE}}(\mathrm{pixel}_{\alpha,\delta}, \mathrm{I}, \mathrm{J}-\mathrm{K_s})}{\sum\sum \mathrm{N_{2MASS}}(\mathrm{pixel}_{\alpha,\delta}, \mathrm{I}, \mathrm{J}-\mathrm{K_s})}, \tag{3.4}$$

where the double sum is over a given I_{2MASS} range and the total $J-K_s$ range in that pixel. Table 3.3 gives an excerpt of the completeness fraction for HEALPIX pixels, in 0.1 magnitude width bins. Full versions of Tables 3.2 and 3.3 are available as part of the online-only materials, and also via the RAVE website.

The resulting completeness as a function of magnitude and sky position has already been shown in the fourth RAVE data release paper (Figure 3 of Kordopatis et al. 2013a), and we replicate it here for DR5 in Figure 3.4[3]. Overall, as in DR4, we find the completeness is highly anisotropic on the sky for any given magnitude bin, and drops off significantly for fainter magnitudes.

3.4.3 Impact of the analysis pipeline

Until now we have only investigated effects that originate from the RAVE target selection. However, when considering certain applications, there is another important issue: namely, the effects of the automated pipelines. RAVE DR5 contains output from a number of pipelines which provide additional information for observed stars. As described in Sec. 3.2, in addition to line-of-sight velocities, RAVE provides estimates of stellar parameters such as effective temperature, surface gravity, elemental abundances, as well as distance and age estimates.

Here we consider the completeness fraction of stars with assigned stellar parameters from the stellar parameter pipeline, following the recommendations given by Kordopatis et al. (2013a), selecting all stars that have

- SNR ≥ 20,
- $|$`correctionRV`$| < 10\,\mathrm{km\,s^{-1}}$,

[2] The nested, or tree structure, scheme refers to the way that HEALPIX pixels are numbered (see Figure 4 of Górski et al. 2005). The hierarchical structure of the nested scheme allows for degrading the resolution of a HEALPIX map from the base resolution, and is the same scheme used for Gaia DR1.

[3] We note that the completeness fraction can, in some very rare cases, be null or greater than one. This is due to the fact that we remove stars from our parent 2MASS sample that do not meet the specified quality criteria.

- $\sigma(V_{\rm los}) < 8\,{\rm km\,s^{-1}}$,
- `correlationCoeff` > 10 (Tonry & Davis (1979) correlation coefficient).

In addition, this pipeline yields reliable results only in a restricted region in stellar parameter space (Kordopatis et al. 2013a). We explicitly implement this by using only stars with

$$\begin{array}{rcccl} 4000{\rm K} & < & T_{\rm eff} & < & 8000{\rm K}, \\ 0.5 & < & \log g & < & 5\,. \end{array} \tag{3.5}$$

These limits are based on the range of parameters for the spectra used for the learning grid of the analysis pipeline (Kordopatis et al. 2011, 2013a), as well as unphysical or highly unlikely combinations of derived parameters.

These restrictions have to be taken into account when comparing observed data with specific Galaxy models. They can be expressed as an additional selection function

$$S_{\rm pipeline} = S_{\rm pipeline}(T_{\rm eff}, \log g, [{\rm Fe/H}]) \tag{3.6}$$

and hence the complete selection function S is

$$S = S_{\rm pipeline} \times S_{\rm select}. \tag{3.7}$$

We give examples of this effect in Figures 3.5 and 3.6, for the selection function evaluated with HEALPIX pixels, and field-by-field, respectively. Figure 3.5 shows the distribution of the number of stars satisfying these criteria that have derived parameters (stellar parameters, distance, and chemical abundances) available in RAVE DR5 as a function of $I_{\rm 2MASS}$ magnitude (left and middle panels represent $S_{\rm pipeline}$, see Eq. 3.6), as well as the completeness fraction of these parameters in RAVE with respect to 2MASS (right panel represents the complete selection function, see Eq. 3.7). We find that the number of stars having a given parameter in DR5 varies as a function of magnitude, with the brightest magnitude bin ($9 < I_{\rm 2MASS} < 10$) having the highest number of stars with stellar parameters, distances, and chemical abundances. When we consider the relative fraction of stars with a given parameter (using radial velocity as a baseline, as all stars satisfying the quality criteria have radial velocity measurements), we find stellar parameters are derived for all stars with radial velocities, while distances are derived for ~ 80 per cent of these stars. The relative fraction of stars with chemical abundance estimates is calculated for stars which have all six element abundances derived from the chemical abundance pipeline (Boeche et al. 2011). We find that ~ 40 – 60 per cent of stars brighter than 10th magnitude have chemical abundance information available in DR5. Finally, when we consider the completeness of a given derived parameter in RAVE with respect to 2MASS, we find that stars in the brightest magnitude bin ($9 < I_{\rm 2MASS} < 10$) have the highest completeness. This panel represents the complete selection function (see Eq. 3.7).

In Figure 3.6, we characterize the completeness fraction of derived parameters for a typical RAVE pointing. RAVE stars are shown in black, purple, and orange, with the underlying 2MASS parent sample shown in grey. For this particular pointing, we find all stars have estimated stellar parameters, ~ 90 per cent have distances, and ~ 10 per cent have chemical abundance estimates.

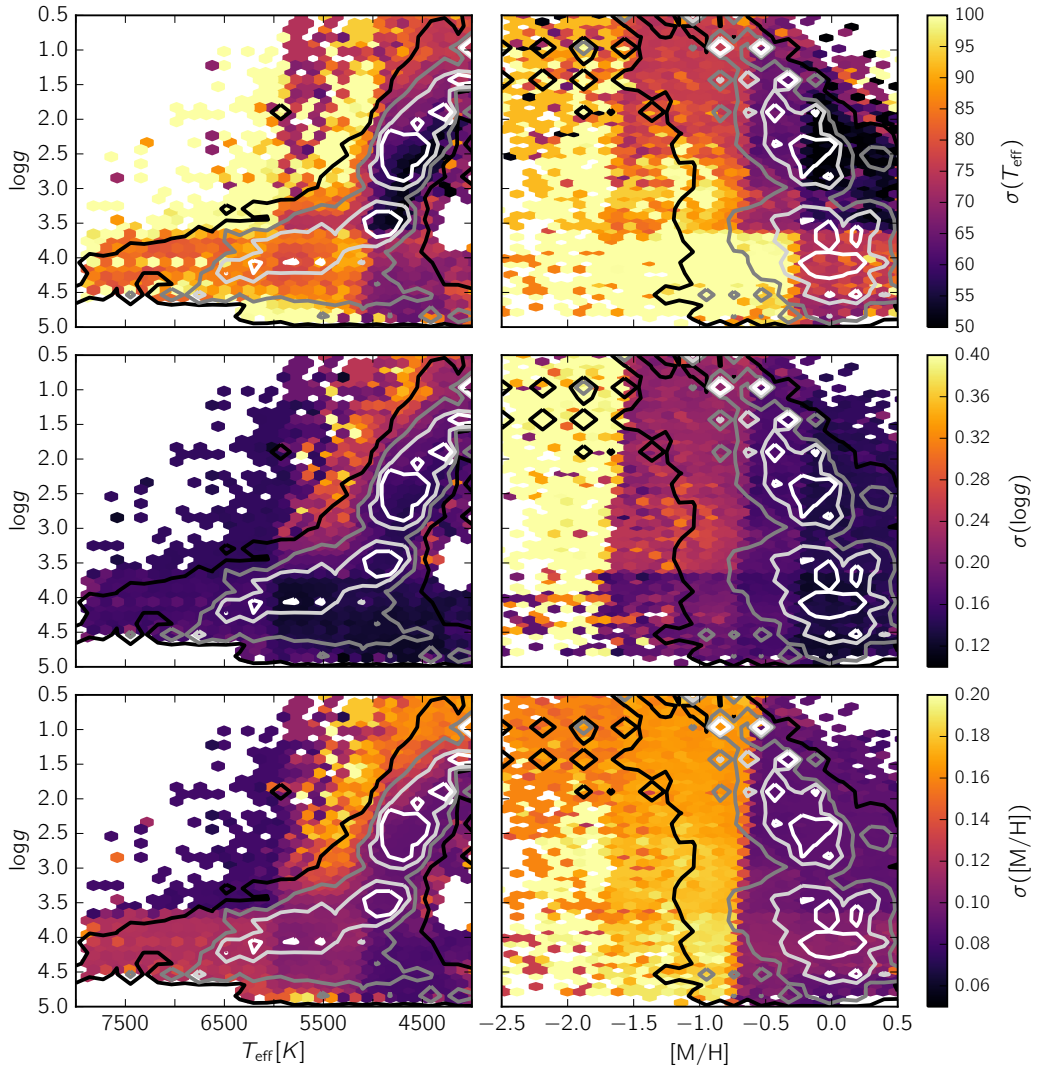

Figure 3.7 — Mean uncertainties as a function of stellar parameters available in RAVE DR5. The left column shows the distribution of uncertainties in $T_{\rm eff}$- log$g$ space, and the right column shows the same but in [M/H]-log$g$ space. Each row shows the distribution of the uncertainties of a different parameter as indicated by the colour bars on the far right. The contours indicate 33, 67, 90, and 99 per cent of all RAVE DR5 stars.

3.5 Comparison with a Galactic model

We now explore the potential influence of the selection function with respect to inducing biases in the stellar parameter distributions of our RAVE DR5 stars compared with what we expect from models of the Galaxy. For this comparison, we utilize the stellar population synthesis code GALAXIA[4] (Sharma et al. 2011).

GALAXIA is a tool which uses a given Galactic model to conduct synthetic observations, generating a catalogue which imitates any given survey of the Milky Way. Here, we use the default provided in GALAXIA, a modified version of the

[4]http://galaxia.sourceforge.net/

Besançon model (Robin et al. 2003). Details on the extent of these modifications can be found in Sharma et al. (2011). The Besançon model within the GALAXIA framework has been found to agree quite well with Besançon star counts (Sharma et al. 2011). The input parameters for GALAXIA are very simple, and correspond well to our adopted form of RAVE's selection function (Eq. 3.1).

The catalogue may be generated for a given circular area on the sky, as well as for the whole sky. In order to compare these mock observations with our two methods of characterising the selection function of RAVE, we generate two catalogues: one on a field-by-field basis, and one full-sky, which is then divided into HEALPIX pixels. For each of these catalogues, we allow GALAXIA to generate stars with apparent I-band magnitude $0 < I < 13$, and no colour restriction. We then perturb the output from GALAXIA with a simple noise model to imitate observational uncertainties present in RAVE, and apply the RAVE selection function. We refer to this modified catalogue as our 'mock-RAVE' catalogue. The mock-RAVE catalogue can then be compared to our parent GALAXIA sample (where the RAVE selection function has not been applied), to evaluate the effect that the selection function has on fundamental distributions such as kinematics and chemistry.

3.5.1 Applying uncertainties to generate a mock-RAVE catalogue

GALAXIA provides stellar parameters and magnitudes with infinite precision and accuracy. This does not reflect our observational data, where each of the derived parameters has intrinsic uncertainties associated with its measurements. In order to facilitate an accurate comparison between the mock catalogue and real RAVE data, we perturb J, K_s, $T_{\rm eff}$, log g, and [Fe/H] available in our GALAXIA catalogue based on the uncertainty distributions of 2MASS magnitudes and RAVE stellar parameters before applying the selection function of RAVE. We then apply the selection function of RAVE using both methods described in Sec. 3.4: field-by-field and HEALPIX pixels. In addition to scattering the GALAXIA distributions with our simple noise model, we slightly modify the metallicity distribution of the thick disc and the halo of our GALAXIA output, for better agreement with observations.

2MASS apparent magnitude uncertainties

First, we modify the output GALAXIA 2MASS J and K_s magnitudes by a simple noise model, derived from the observational uncertainties in 2MASS. To do this, we characterize the observational uncertainty for a given 0.1 magnitude bin as a function of magnitude. We model the distribution of uncertainties in each bin as a Gaussian, and draw from this Gaussian to obtain an 'observational uncertainty' on our GALAXIA output. Typical 2MASS J magnitude uncertainties are of the order of 0.025 dex. From the modified J and K_s values, we obtain an $I_{\rm 2MASS}$ for each GALAXIA star using Eq. 3.2.

Applying RAVE-like uncertainties to stellar parameters

In order to compare the stellar parameters available in this mock catalogue with those derived from the RAVE DR5 stellar parameter pipeline, we must first modify

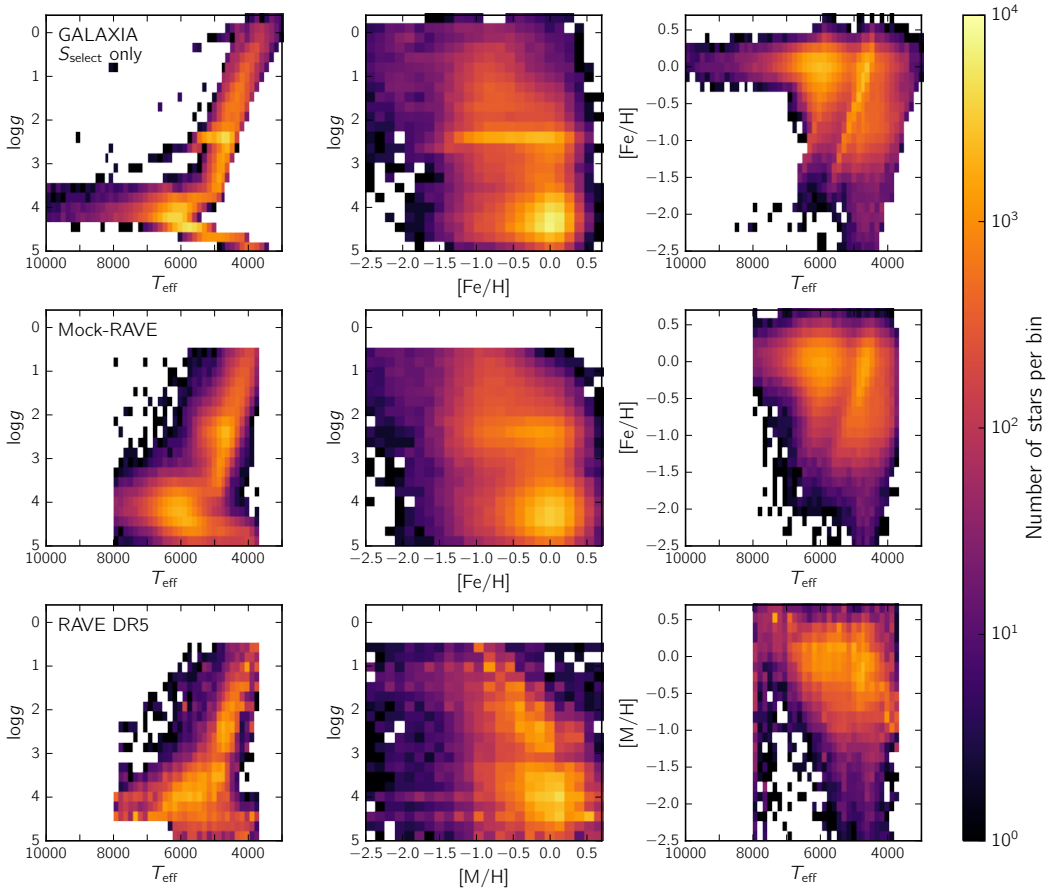

Figure 3.8 — 2D histograms of three stellar parameter spaces: log$g$-$T_{\rm eff}$ (left), log$g$-abundance ([Fe/H] for GALAXIA, [M/H] for RAVE) (middle), and abundance-$T_{\rm eff}$(right). The top row shows these 2D histograms for our GALAXIA sample with the RAVE selection function applied. In the middle row we show our GALAXIA sample which has had both the RAVE selection function and RAVE-like uncertainties applied. The bottom row shows our RAVE DR5 sample. The colour scale is log normalized.

the output from GALAXIA with the uncertainty distributions of RAVE stellar parameters. The RAVE DR5 stellar parameter pipeline provides individual uncertainties for each star, and we can use the distribution of these uncertainties to modify our initial GALAXIA catalogue by RAVE-like uncertainties, similar to the process used in the previous section, but in a higher-dimensional space due to correlations between the uncertainties.

In Figure 3.7, we show the correlation of uncertainties as a function of position in different planes of stellar parameters. Here, we colour-code the mean uncertainty as a function of the stellar parameters in $T_{\rm eff}$- log$g$ and $T_{\rm eff}$-[M/H] space. The highest uncertainties are found primarily in hot, giant stars in the $T_{\rm eff}$- log$g$ plane, and metal-poor stars in the [M/H]-log$g$ plane (see also Table 4, Kunder et al. 2017). However, comparing these regions to the density contours, we find that these regions are sparsely populated, and therefore should not significantly affect the mean uncertainty. The abrupt jumps, visible at e.g. $T_{\rm eff} \sim 5000\,$K and [M/H] ~ -0.7,

result from discrete coverage of the stellar parameter space by model atmospheres that are compared to the observed spectra by the pipeline. We find that the majority of RAVE stars have similar uncertainties in spectral parameters, with $\langle\sigma(T_{\rm eff})\rangle \sim 50-75\,$K, $\langle\sigma(\log g)\rangle \sim 0.1-0.2$ dex, and $\langle\sigma([{\rm M/H}])\rangle \sim 0.1$ dex.

In addition to an anisotropic distribution of uncertainties in in $T_{\rm eff}$- log$g$ and $T_{\rm eff}$-[M/H] space, it has been well documented that these uncertainties in the derived atmospheric parameters are also correlated (see Figure 6 of Kordopatis et al. (2011) and Figure 23 of Kordopatis et al. 2013a). Due to these correlations, it is not sufficient to simply model the uncertainties as individual Gaussians and draw from them. Instead, we consider the distribution of uncertainties to have the form of a multivariate Gaussian, and estimate the covariance between uncertainties in $T_{\rm eff}$,log$g$, and [M/H]. We then draw from this multivariate Gaussian to obtain simultaneously uncertainties for these three respective parameters. Note that in this way we can introduce only the internal uncertainties of the analysis pipeline, but not systematic shifts coming from inaccuracies of the stellar atmosphere models.

Finally, we apply $S_{\rm pipeline}$ by setting weights to zero for all stars that do not fulfill the criteria given in Eq. 3.5. We refer to the result as the mock-RAVE catalogue. The effect of this step is model dependent as, for example, the number of super-solar metallicity stars varies between different Galaxy models. Using the version of the Besançon model in GALAXIA, we find that approximately 9 per cent of stars fall outside of our $T_{\rm eff}$ and log$g$ limits.

The effect of applying these observational uncertainties as well as $S_{\rm pipeline}$ is shown in Figure 3.8. The top row shows 2D histograms of stellar parameters for our GALAXIA sample (without the application of $S_{\rm pipeline}$). RAVE-like uncertainties and the selection function are applied to obtain the panels in the middle row. Our RAVE sample is shown on the bottom row. Overall, we find good agreement in the distribution of these stellar parameters between the observations and the mock-RAVE catalogue.

3.5.2 Impact of the selection function

We now turn to the implications of the observed stellar populations due to the selection function of RAVE. While RAVE targets within the footprint were selected on purely photometric grounds, it remains to be seen if changes to the observing strategy as well as the applied colour cut at low latitudes have induced biases in the observed characteristics of the sample. In order to test if RAVE is a kinematically unbiased survey, we compare the Galactocentric cylindrical velocity distributions of the parent GALAXIA sample with those of the mock-RAVE catalogue. We also examine potential biases in the metallicity distribution of the sample, as abundance measurements are highly correlated with other derived values, such as effective temperature and surface gravity, as well as external characteristics such as kinematics. Hence, biases in either velocity or metallicity are potentially harmful if undetected, for both chemical evolution and dynamical modeling.

We take a uniformly selected subsample of our full GALAXIA catalogue in the footprint of RAVE as our expected 'parent' sample (i.e., what we consider to be the 'truth' for the purpose of this exercise), and compare it to our mock-RAVE

catalogue. Any considerable deviations between the two distributions may indicate a bias in RAVE due to the selection function. We note that for this exercise, we do not apply RAVE-like uncertainties to the velocities or metallicities in our mock-RAVE catalogue (i.e., here we use the true GALAXIA output). In addition to a GALAXIA subsample limited to $I < 13$, we also investigate the effects of limiting our GALAXIA subsample to $I < 12$, as it has been shown in Figure 3.3 that RAVE is not complete at $I_{2MASS} = 13$. Quantitatively, in order to characterize the skewness of each distribution we compute quartile values (Q_1, Q_2, Q_3), which represent the 25^{th}, 50^{th}, and 75^{th} percentiles, respectively.

We investigate these potential biases in three subsamples: giants ($\log g < 3.5$), the main sequence region ($\log g > 4.0, T_{eff} < 5500$K), and the turnoff region ($\log g > 3.5, 5500\text{K} < T_{eff} < 7000\text{K}$). The boundaries of these subsamples have been determined from the $T_{eff}-\log g$ plane of our parent GALAXIA sample (see top row of Figure 3.8). For these comparisons we also consider the distance $|z|$ from the Galactic plane by dividing our subsamples into 3 bins of height above the plane. The size of these bins varies between our subsamples, as these populations probe different distance distributions.

Velocity distribution comparison

We first examine the effect of our selection function on distributions of the cylindrical Galactocentric velocity components in our mock-RAVE catalogue. Our results are shown in Figures 3.9, 3.10, and 3.11, with the GALAXIA distribution shown as dashed black curves, and the mock-RAVE catalogue shown in green. A GALAXIA distribution limited to $I < 12$ is shown as solid black curves. Quartile values are given in each panel.

For our giant and main sequence region samples (Figures 3.9 and 3.10), we find nearly identical distributions for all distance bins when comparing our mock-RAVE catalogue with the respective parent GALAXIA distributions. We consider the distributions to agree if we find all three quartiles to agree within $5\,\text{km}\,\text{s}^{-1}$. Using this criterion, we confirm that the selection function does not impose kinematic biases for these populations as a whole. We note that when we consider only low-latitude fields ($5^\circ < |b| < 25^\circ$), the colour criterion that was imposed to select preferentially for giants (see Section 3.3.1) reflects to a small bias in age. Further comparisons with the model have shown that this age bias does not introduce a significant kinematic bias, however, we urge some caution when considering the velocity distributions for these low-latitude fields.

We also find good agreement in most height bins for each velocity component of our turnoff region sample (Figure 3.11). However, for the most distant bin ($0.30 < |z| < 0.60$ kpc), there is a slight difference between the distributions in the low-V_ϕ tail. Specifically, the application of the selection function leads to an underrepresentation of stars with $V_\phi \lesssim 150\,\text{km}\,\text{s}^{-1}$ in our mock-RAVE catalogue. Bias is present in all components of the velocity, but we find it most clearly in V_ϕ, as the velocity distribution functions for the thin disc, thick disc, and halo do not have the same mean for this component.

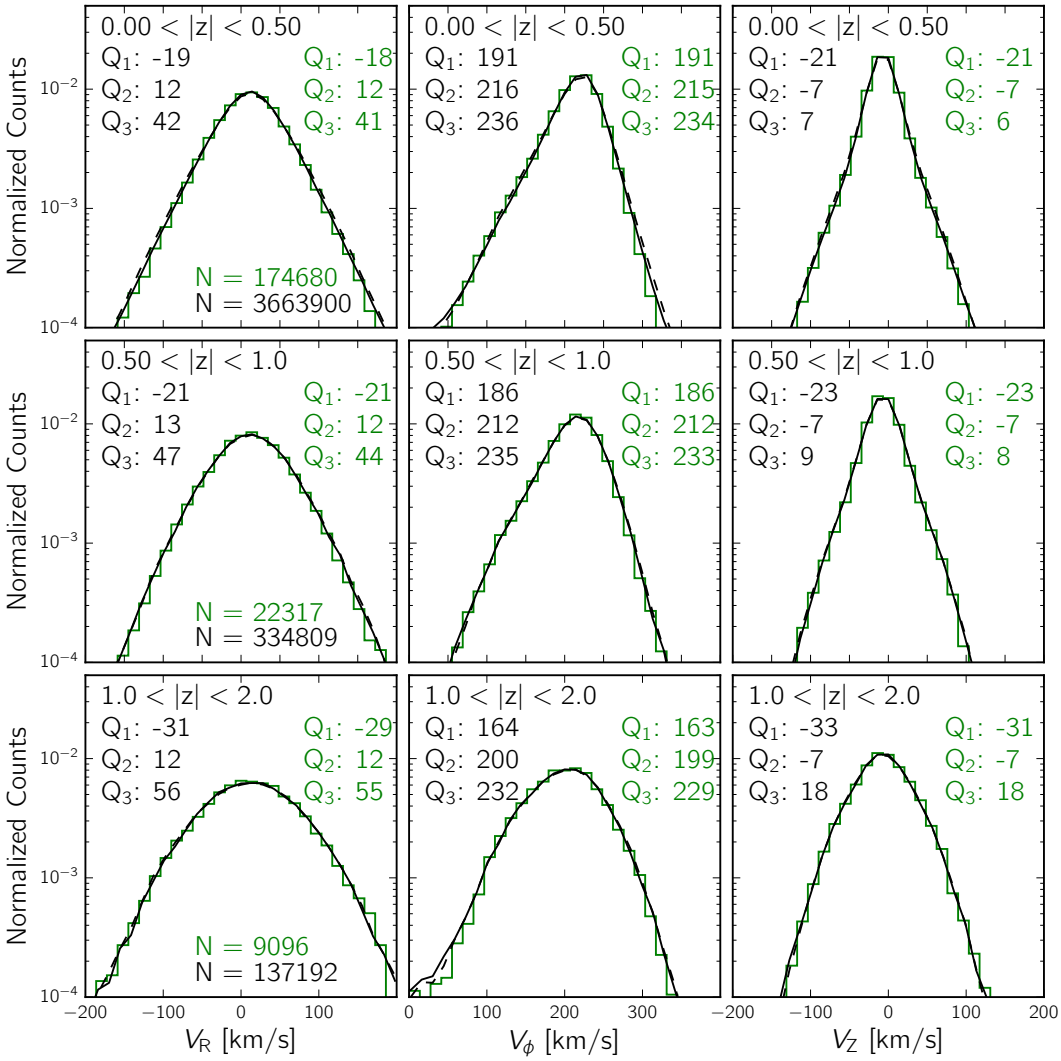

Figure 3.9 — Distributions of Galactocentric cylindrical velocity components for samples of giant stars (log$g$ < 3.5) at different distances from the Galactic plane as indicated in the panels. The green histograms show the velocity distributions in the mock-RAVE catalogue, while the black-dashed curves show the distributions for our parent GALAXIA subsample of giants. Solid black curves show the distribution for a parent GALAXIA sample limited to $I < 12$. Quantile values (Q_1, Q_2, Q_3) for both distributions are given in each panel, which represent the 25$^{\text{th}}$, 50$^{\text{th}}$, and 75$^{\text{th}}$ percentiles, respectively. The sample size (N) for the distributions are shown in green and black, representing the mock-RAVE sample and the parent GALAXIA sample limited to $I < 12$, respectively. The y-axis is plotted on a logarithmic scale.

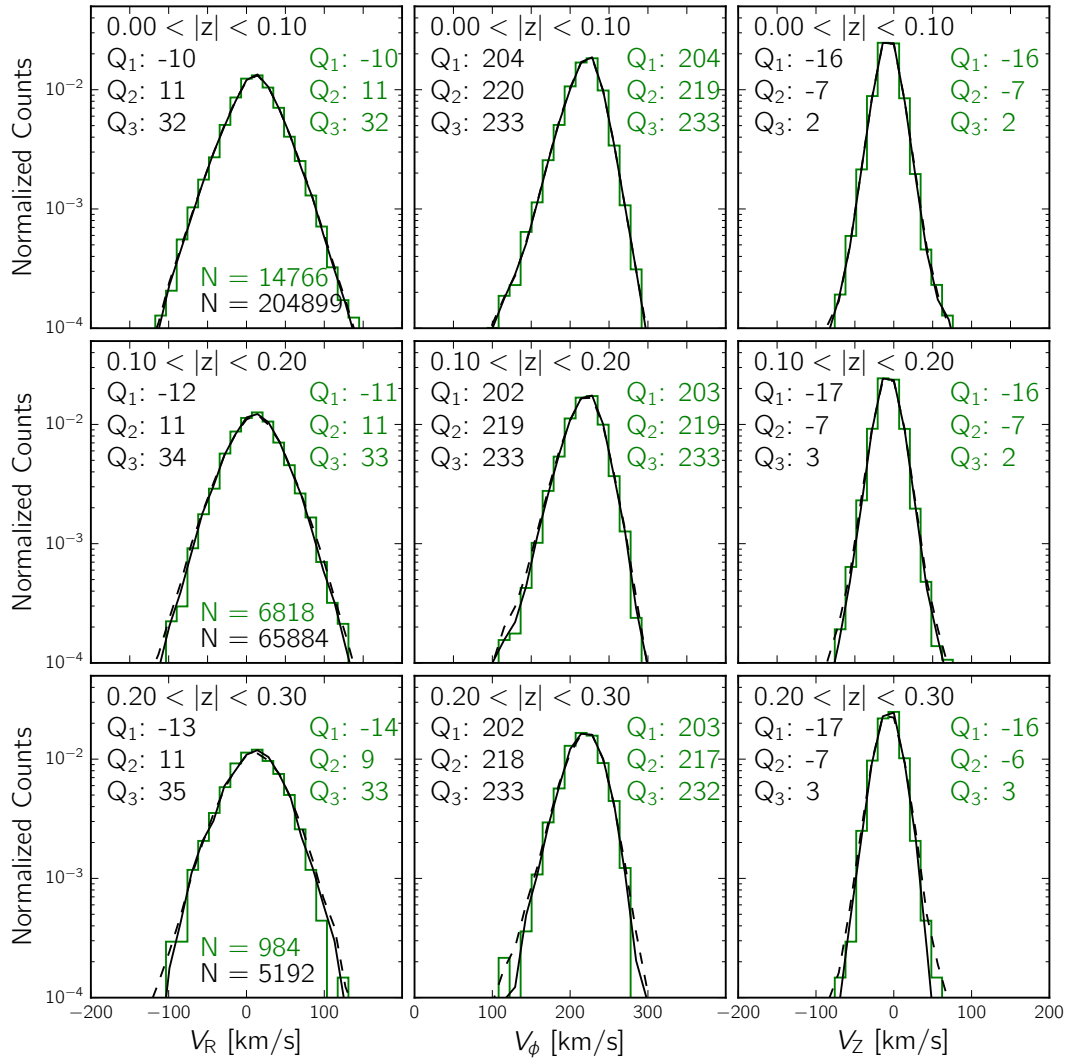

Figure 3.10 — Same as Figure 3.9 but for the main sequence region ($\log g > 4.0$, $T_{\rm eff} < 5500$K) sample.

The difference that we find can be explained by the difference in magnitude distributions between our two samples: our parent GALAXIA sample extends to $I_{\rm 2MASS} \sim 13$ (see Section 3.5), whereas our mock-RAVE sample follows the I-magnitude distribution of RAVE (see Figure 3.3), by the definition of the selection function. As a consequence, there are relatively few stars observed in RAVE with $12 < I < 13$ compared to those present in our parent GALAXIA sample. By having a larger fraction of stars at fainter magnitudes, the parent GALAXIA sample probes more of the thick disc and halo compared to our mock-RAVE sample. This effect also is reflected in differences that we see between the metallicity distributions (see Section 3.5.2 and Figure 3.12). This discrepancy is small (and indeed disappears if we limit our parent GALAXIA sample to $I_{\rm 2MASS} < 12$), and overall the distributions meet our criterion (all three quartiles agree within 5 km s^{-1}), so we consider the turnoff region stars to also be kinematically unbiased.

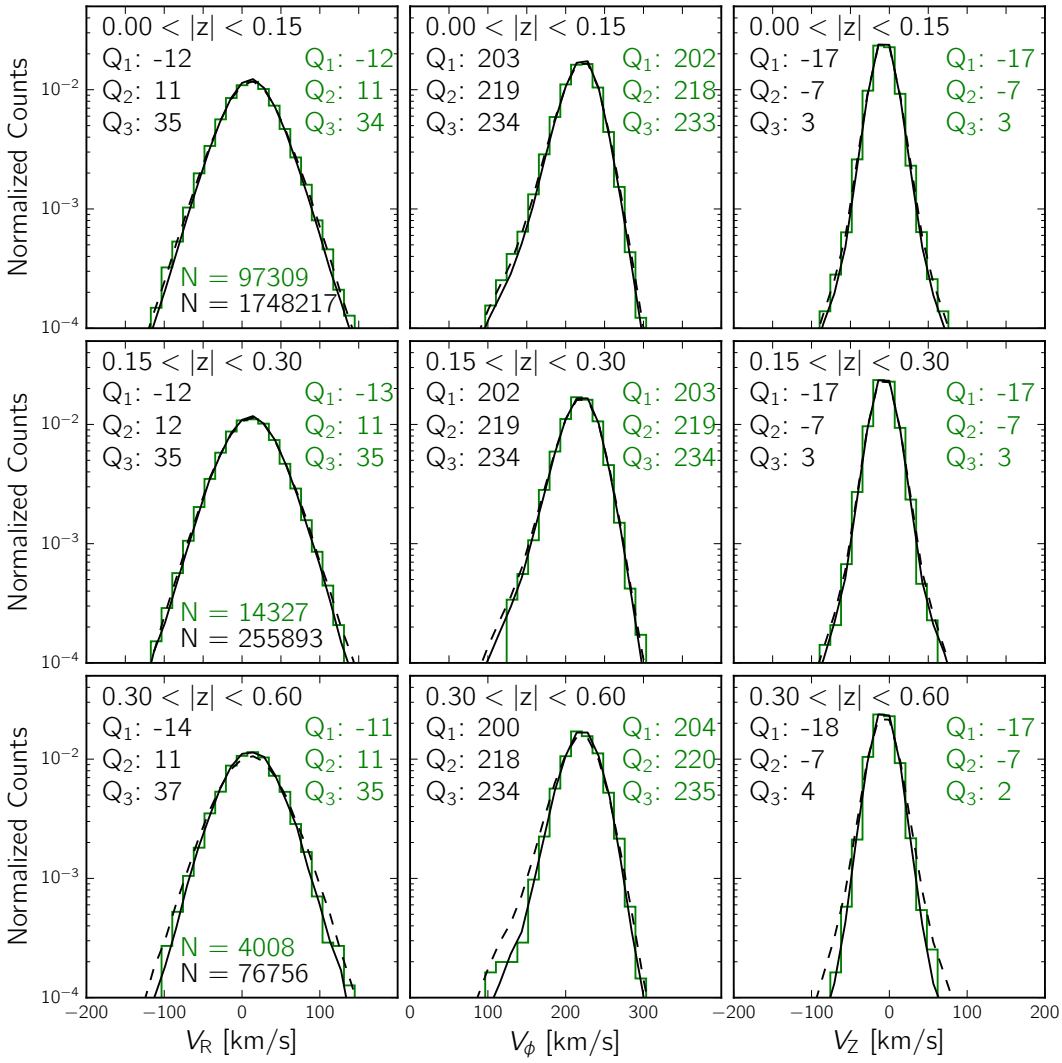

Figure 3.11 — Same as Figure 3.9 but for the turnoff region ($\log g > 3.5, 5500\,\mathrm{K} < T_{\mathrm{eff}} < 7000\,\mathrm{K}$) sample.

Similar tests were done for a sample of hot dwarf stars ($\log g > 3.5$, $T_{\mathrm{eff}} > 7000$K), but are not shown here. As with the our turnoff region sample, we find our sample of hot dwarfs to also be unbiased for $I < 12$.

Metallicity distribution comparison

Next, we examine the metallicity distributions of the GALAXIA samples and our mock-RAVE catalogue. The metallicity distributions for each subsample in different slices in distance $|z|$ from the Galactic plane are shown in Figure 3.12. Here, we consider the distributions to agree if all three quartiles agree within 0.1 dex.

For giants (left column of Figure 3.12) and stars in the main sequence region (middle column of Figure 3.12), we find very good agreement between the GALAXIA and mock-RAVE metallicity distributions for all distance bins. For stars in the main

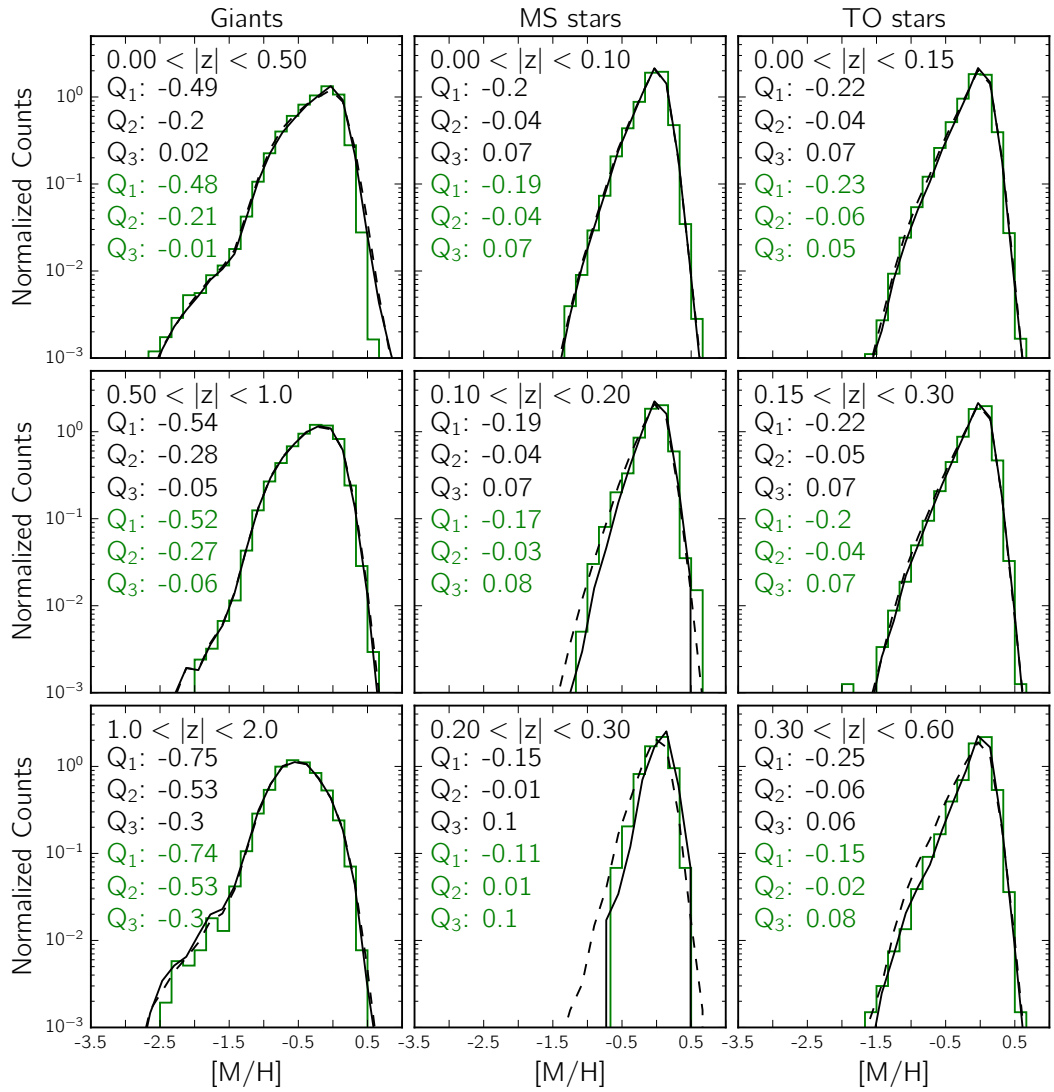

Figure 3.12 — Metallicity distributions for each sample in different distances from the Galactic plane as indicated in the panels. The left column shows the distributions for giants, the middle shows main sequence region stars, and the right shows turnoff region stars. The black-dashed curves indicate the underlying distributions for our GALAXIA parent sample, while the green histograms show the metallicity distributions in the mock-RAVE catalogue. Solid black curves show the distribution for a parent GALAXIA sample limited to $I < 12$. Quartile values (Q_1, Q_2, Q_3) for both distributions are given in each panel. The y-axis is plotted on a logarithmic scale.

sequence region and the most distant bin ($0.20 < |z| < 0.30$ kpc), we find that in our mock-RAVE sample the metal-poor tail of the metallicity distribution is slightly underrepresented, compared to the GALAXIA sample. However, this difference can be explained by small number statistics, as our mock-RAVE sample would need only one star below [M/H] ~ -0.6 to reconcile the difference between the two distributions. Again, despite this small discrepancy, the quartile values satisfy our criterion, and therefore we consider our main sequence region sample to be chemically unbiased. We conclude that for giants and stars in the main sequence region, our metallicity distribution is minimally affected by our selection function.

Similarly, for the turnoff region sample (right column of Figure 3.12), we find good agreement for the two closest distance bins, with differences between the two distributions found only in the furthest distance bin ($0.30 < |z| < 0.60$ kpc). For this bin, we find that our criterion is barely met, with Q_1 differing by ~ 0.1 dex. This discrepancy between the two distributions is explained by the difference in magnitude limits as described in Section 3.5.2. That is, as our parent GALAXIA sample includes a larger fraction of faint ($12 < I < 13$) stars compared to our mock-RAVE sample, it probes a larger volume, and therefore more of the thick disc and halo. This effect is less prominent for our giant sample, as the relative fractional increase of thick disc and halo stars is much less for giants, compared to our dwarf sample. We conclude that our turnoff region sample is unbiased for $I_{2\mathrm{MASS}} < 12$. As with the velocity comparisons, we also test the [M/H] distributions for a sample of hot dwarf stars ($\log g > 3.5$, $T_{\mathrm{eff}} > 7000$K), and find them to also be chemically unbiased.

3.6 Discussion and conclusions

We have described, in detail, how to evaluate the selection function S of the RAVE survey in two different ways: field-by-field, and HEALPIX pixels. In addition, we discussed the uncertainty distributions of RAVE DR5 and illustrated that these uncertainties depend heavily on the position in stellar parameter space. We then generated a mock-RAVE catalogue by applying the detailed selection function to the model output, and modified the raw GALAXIA output by RAVE-like uncertainties.

To investigate that RAVE is a kinematically and chemically unbiased survey, we tested the impact of S on the resulting velocity and metallicity distributions using a modified version of the Besançon model available in the GALAXIA framework. The velocity and metallicity distributions of our mock-RAVE catalogue were compared with the distributions of the underlying GALAXIA populations. We find that, for $I < 12$, our selection function does not intrinsically induce biases in the kinematics or chemistry of stars within the stellar parameter space covered in RAVE ($4000\mathrm{K} < T_{\mathrm{eff}} < 8000\mathrm{K}$ and $0.5 < \log g < 5.0$), with respect to expectations from the Besançon model available in GALAXIA. We do find some small biases when we consider a parent sample extending to $I = 13$, however, it has been shown that the completeness of RAVE falls off for fainter magnitudes (due to the magnitude limit imposed from the input catalogues), and therefore our conclusion stands for the magnitude range where we consider RAVE to provide a representative sample of stars ($9 < I < 12$).

Under these criteria, and within this parameter space, RAVE stars provide unbiased samples in terms of kinematics and metallicities that are well suited for kinematic modeling without taking into account the detailed selection function via volume corrections.

For our giant and main sequence region samples, we find good agreement between the parent GALAXIA sample and our mock-RAVE catalogue. We find similar trends for our sample of turnoff region stars, with small differences in the velocity distributions for the most distant stars, and the metal-poor tail of the [M/H] distribution. However, we explain this bias due to the fact that our GALAXIA sample includes a larger number of stars at fainter magnitudes compared to our mock-RAVE catalogue. The parent GALAXIA sample therefore probes a larger volume than our mock-RAVE catalogue, and consequently more of the thick disc and halo populations. As we are able to account for the source of these differences, we consider our turnoff region sample to also be kinematically and chemically unbiased for $I_{2\mathrm{MASS}} < 12$.

Recently, a number of studies used RAVE data, and in particular subsamples of giant stars, for kinematic modeling (e.g. Binney et al. 2014a; Piffl et al. 2014; Minchev et al. 2014b; Williams et al. 2013; Kordopatis et al. 2013b; Bienaymé et al. 2014). Here we confirm that the giant stars in RAVE can indeed be used as an unbiased sample. Piffl et al. (2014) fitted a full dynamical model of the Milky Way to the kinematics of the RAVE giants. They then tested if the resulting model would also correctly predict the kinematics of a sample of hot dwarf stars from RAVE and found a number of discrepancies. Their conclusion was that the thick disc distribution function in their model was too simplistic. However, Binney et al. (2014a) also found that a similar dynamical model fitted to data from the GCS (Nordström et al. 2004) could reproduce the RAVE hot dwarf kinematics, but did not fit the RAVE giants. Since the GCS has a selection function that is different from that of the RAVE dwarfs, this implies that taking into account a more complicated volume correction for the hot dwarfs will not be enough to completely reconcile them with the model of Piffl et al. (2014). Hence a more complex distribution function for the thick disc, as argued for by the authors, seems still necessary.

We also illustrate that the quantified RAVE selection function can be used to generate mock-RAVE surveys from stellar population synthesis models, and in combination with code frameworks like GALAXIA, it can serve as a powerful tool to test Galaxy models against the RAVE data. The two versions of the RAVE selection function produced by this study (field-by-field and by HEALPIX pixel) will be made publicly available on the RAVE web site (https://www.rave-survey.org).

Acknowledgements. JW thanks Ivan Minchev, Friedrich Anders, Else Starkenburg, Kris Youakim, and Alexey Mints for their comments and helpful discussions, which have improved the quality and clarity of the text. Funding for this work and for RAVE has been provided by: the Australian Astronomical Observatory; the Leibniz-Institut fuer Astrophysik Potsdam (AIP); the Australian National University; the Australian Research Council; the European Research Council under the European Union's Seventh Framework Programme (Grant Agreement 240271 and 321067); the French National Research Agency; the German Research Foundation (SPP 1177

and SFB 881); the Istituto Nazionale di Astrofisica at Padova; The Johns Hopkins University; the National Science Foundation of the USA (AST-0908326); the W. M. Keck foundation; the Macquarie University; the Netherlands Research School for Astronomy; the Natural Sciences and Engineering Research Council of Canada; the Slovenian Research Agency (research core funding No. P1-0188); the Swiss National Science Foundation; the Science & Technology Facilities Council of the UK; Opticon; Strasbourg Observatory; and the Universities of Groningen, Heidelberg and Sydney. The RAVE web site is at https://www.rave-survey.org.

4 Correlations between age, kinematics, and chemistry as seen by the RAVE survey

Jennifer Wojno, Georges Kordopatis, Paul McMillan, Matthias Steinmetz, and the RAVE collaboration

— Paper in preparation —

ABSTRACT

In this paper, we explore the connections between age, chemistry, and kinematics from $7.5 < R < 9.0$, using a sample of $\sim 10\,000$ intermediate-mass (FGK) stars observed with the RAVE survey. Kinematics of this sample are determined using radial velocity measurements from RAVE, proper motions from UCAC5, and parallax measurements from TGAS. In addition, ages for RAVE stars are determined using a Bayesian method, taking TGAS parallaxes as a prior to better constrain estimates. For a robust analysis, we divide our sample into young ($0 < \tau < 3$ Gyr) and old ($10 < \tau < 13$ Gyr) populations, and then consider different metallicity bins for each of these age groups. We find gradients in mean radial velocity as a function of Galactocentric radius ($\partial\langle V_{\rm R}\rangle/\partial R$) for both young and old stars, but this gradient is noticeably steeper for our young stars. In addition, we find that for young stars, this gradient flattens as a function of decreasing metallicity, from -22.8 ± 0.3 km s^{-1} kpc^{-1} for our young, metal-rich stars to -10.1 ± 0.2 km s^{-1} kpc^{-1} for metal-poor stars. This gradient is indicative of non-axisymmetries in the Galactic gravitational potential: the presence of spiral arms and the bar. We also find an offset in V_ϕ between young and old, metal-rich and metal-poor stars, which indicates a dynamical scenario consistent with previous findings. As we find significant differences in the kinematics of young and old populations in the solar neighbourhood, we attempt to reconcile them with known features of the local velocity field, and consider the effects of each of these features (i.e., the contribution of either the bar or spiral arms) on the trends we measure.

4.1 Introduction

With ongoing and upcoming large-scale spectroscopic surveys, the field of Galactic archeology stands poised to reveal the formation history of our own Galaxy from the perspective of individual stars. As low- and intermediate-mass stars are long-lived, they can act as time capsules, allowing us a window to the environment in which they were born (Freeman & Bland-Hawthorn 2002). A number of these surveys, such as RAVE (Steinmetz et al. 2006), SEGUE (Yanny et al. 2009), APOGEE (Majewski et al. 2015), Gaia-ESO (Gilmore et al. 2012), LAMOST (Zhao et al. 2012), and GALAH (De Silva et al. 2015), already provide a number of crucial parameters necessary for disentangling the formation history of the Galactic disc, such as stellar radial velocities, effective temperatures, surface gravities, and individual chemical abundances.

In order to better understand the source of the dynamic processes that shape the kinematic trends we see in stellar populations today, we turn to measurements of the local velocity field. It has been known for more than a century that the local velocity field is not uniform and contains a number of moving groups: predominantly the Hyades, Pleiades, and Hercules, although with more detailed measurements of stellar velocities, studies are finding ever finer structure in velocity space (e.g., Dehnen 2000; Famaey et al. 2008; Antoja et al. 2015, 2017; Kushniruk et al. 2017). These structures indicate deviations of the MW disc from an idealized axisymmetric model: the presence of the Galactic bar and spiral arms. The source and variation of these features as a function of Galactocentric radius has been explored in a number of simulations (e.g., Quillen et al. 2011; Antoja et al. 2011; McMillan 2013; Monari et al. 2014, 2017a).

In Siebert et al. (2011a), a shallow gradient in $\partial\langle V_{\rm R}\rangle / \partial R$ of -3 km s^{-1} kpc^{-1} was found using RAVE stars, and was fit to a model in Siebert et al. (2012), assuming that the effect was solely due to long-lived spiral arms. They found that they were able to reproduce the observational results with a two-armed model in the solar neighbourhood ($d < 1$ kpc), although they suggest that the bar may also affect these trends. Monari et al. (2014) also developed a model to characterize the contribution of the bar to these asymmetric trends in the velocity field of the solar neighbourhood. They show that if the Sun is close to the OLR, it is possible to reproduce the result of Williams et al. (2013), where they measure a slightly steeper value for $\partial V_{\rm R} / \partial R$, -8 km s^{-1} kpc^{-1}. In addition, Faure et al. (2014) developed a model that included both a bar and spiral arms, and conclude that both components are likely to play a role in producing the observed gradients. Monari et al. (2016) also characterized the effect of the spiral arms on local velocity gradients, showing that stars on the spiral arms move inward toward the centre of the Galaxy while stars in the interarm regions move towards the outer disc, and find a gradient of the order of -8 km s^{-1} kpc^{-1}.

Soon after the radial velocity gradient was found in RAVE stars, Widrow et al. (2012) discovered significant deviations in the vertical velocity component of stars as a function of height above the plane using SDSS. In Williams et al. (2013), they also investigate the 3D structure of the vertical velocities, and conclude these wave-like motions in the plane of the disc are a result of the motions of spiral arms in the

local vicinity. Carlin et al. (2013) also find this signature for a larger volume using LAMOST stars, and propose it is a result of some external perturbation of the disc, such as interactions with a nearby dwarf galaxy such as Sagittarius (Widrow et al. 2012; Purcell et al. 2011; Gómez et al. 2013). An updated version of this study, using a sample of RAVE-TGAS stars with improved distance estimates, is described in Carillo et al. (2017, in prep.).

Recently, Antoja et al. (2017) have explored this space using observational data from RAVE and GCS (Holmberg et al. 2007), with the added advantage of having stellar metallicities to investigate the metallicity dependence of these overdensities. Using a novel approach where they compare the metallicity of regions in velocity space with their symmetric counterparts, they find significant asymmetries in the local velocity field as a function of metallicity. Their findings agree with previous studies (e.g., Famaey et al. 2007), where it has been shown that moving groups in the solar neighbourhood have chemistry differing from the local ISM, but with a significant spread (i.e., they are unlikely to be dissolved open clusters).

Despite these discoveries, there still remains a significant barrier to uncovering the chemodynamical history of the solar neighbourhood: ages of field stars are notoriously difficult to determine. While it is possible to obtain precise age estimates for some specific classes of stars (Soderblom 2010), a “one-size-fits-all" methodology viable with current instruments remains elusive. As a result, while much progress has been made in the past decade with respect to uncovering asymmetries in the local velocity field, both as a function of Galactocentric radius (R) and height above the plane (Z), the relationship between these kinematic trends and the ages (and metallicities) of the constituent populations has not yet been fully explored. With the availability of accurate parallaxes via Gaia-TGAS (Gaia Collaboration et al. 2016; Lindegren et al. 2016) for a large volume of stars, it is now becoming possible to better constrain age estimates for large samples that have well-measured surface gravity, temperature, and metallicity estimates.

Using Gaia-TGAS to obtain accurate 6D phase space information, we can attempt to include age information in our understanding of the chemodynamical history of the Galactic disc. Gaia DR2 will provide an even more valuable resource to explore the kinematics of the solar neighbourhood, with 6D phase space information available for millions of stars to probe even finer substructure in the local velocity field. In addition, all RAVE stars will also be in Gaia DR2, and so detailed kinematics, chemistry, and age information will be available for more than twice the sample we consider for this study.

In this paper, we aim to explore local kinematic trends for different age and metallicity subsamples, in order to uncover possible correlations between these parameters. In Section 4.2 we present a short overview on the RAVE survey and describe the steps taken to select our sample, including a brief overview of the updated distance pipeline used to derive stellar distances (Section 4.2.2), and the process used to validate the age estimates which result as a by-product of the distance pipeline (Section 4.2.3). With our sample of stars in hand, we then explore kinematic trends, in particular $\partial\langle V_{\rm R}\rangle/\partial R$ for two selected age groups (young and old) in Section 4.3, as a function of Galactocentric radius (R). In Section 4.4 we present

a discussion and interpretation of our results, and draw our conclusions from this analysis in Section 4.5.

4.2 Sample selection

4.2.1 The RAVE survey

The RAVE survey collected over half a million medium-resolution ($R \approx 7500$) spectra of stars in the Southern hemisphere from 2003 until 2013, using the 6dF multi-object spectrograph on the 1.2-m UK Schmidt Telescope at the Siding Spring Observatory in Australia. Throughout the course of the survey, parameters derived from the spectra were made publicly available via a number of data releases, with DR5 as the latest data release (Kunder et al. 2017), providing 520 781 measurements for 457 588 individual stars. Centred on the Ca II-triplet region (8410 – 8795 Å) region, this spectral range was chosen specifically to coincide with the spectral range of Gaia's Radial Velocity Spectrometer (RVS) (Prusti 2012; Bailer-Jones et al. 2013; Recio-Blanco et al. 2016). Currently, Gaia DR1 (Gaia Collaboration et al. 2016) provides positions and magnitudes for over a billion stars, and DR2 (April 2018) will provide parallaxes, radial velocities and stellar parameter estimates derived from photometry. However, until spectrophotometric stellar parameters are available from Gaia, the RAVE survey offers one of the largest sample of stars with accurate 6D phase-space information in addition to stellar parameters derived from spectra.

In addition to radial velocities (typical uncertainties ~ 2 km s^{-1}), RAVE DR5 contains a number of other stellar parameters derived from spectra including effective temperature, surface gravity, metallicity ([M/H]), as well as individual abundances for six elements (Mg, Al, Si, Ti, Fe, Ni) (Boeche et al. 2011). To provide additional parameters such as apparent magnitudes and proper motions, RAVE DR5 was cross-matched with a number of other astrometric and photometric catalogues. In particular, RAVE has a significant overlap with stars available in the Tycho-Gaia astrometric solution (TGAS; Lindegren et al. 2016), with RAVE DR5 containing 215 590 unique TGAS stars.

4.2.2 Distance determinations

For this study, we use distances determined using an updated version of the pipeline described in Binney et al. (2014a), the full details of which are outlined in McMillan et al. (2017). The updated distance pipeline allows for TGAS parallaxes to be included as an input prior, in addition to stellar parameters such as temperature, surface gravity, and metallicity from RAVE, 2MASS and All-WISE photometry, and an underlying Galactic model. The default Galactic model (prior) used is the same as that used for the distance determinations available in DR4 and DR5 and includes some prior on stellar ages for a given disc component (see Eqs. 13-15 in McMillan et al. 2017). Full details of the available priors can be found in Section 6 of McMillan et al. (2017). From both internal tests and comparisons with external catalogues, McMillan et al. (2017) reports that the combined spectrophotometric distance estimates perform better than purely spectroscopic or astrometric estimates alone.

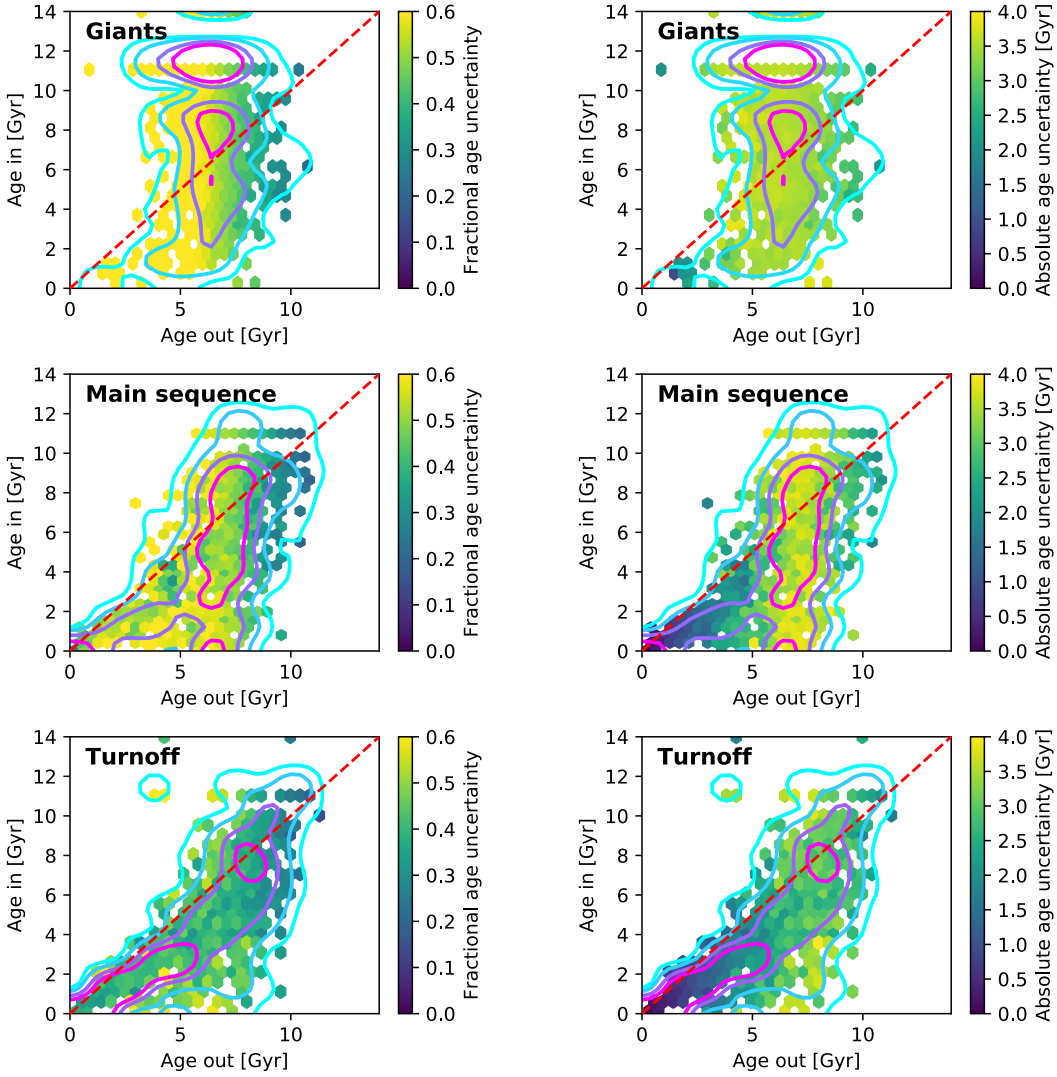

Figure 4.1 — Input age vs. output age, with bins coloured by fractional age uncertainty in the left column, and by absolute age uncertainty in the right column. Giants, main sequence stars, and turn off stars are shown as the top, middle, and bottom rows, respectively. Contours indicate 33, 67, 90, and 99 per cent of the sample.

In addition to distance estimates, the updated pipeline also produces estimates of stellar mass, metallicity, line of sight extinction, and age as byproducts. For this work we utilize a model where distances and ages have been derived using a flat prior on age, to avoid drawing biased conclusions on account of the model.

4.2.3 Age validation

To validate the age estimates coming from the pipeline described in McMillan et al. (2017), we generate a mock catalog of RAVE-like stars using the population synthesis code GALAXIA (Sharma et al. 2011). As GALAXIA produces stars with perfectly-known ages in addition to atmospheric parameters ($T_{\rm eff}$, log g, [M/H]), 2MASS photometry,

and distances, generated based on PARSEC (Bressan et al. 2012) isochrones, it offers a suitable test sample for assessing internal uncertainties on the output of the distance pipeline.

Mock catalogue generation

We generate a RAVE-like survey of Southern hemisphere stars with I-magnitude range $7 < \mathrm{I_{DENIS}} < 13$, to cover the whole magnitude range of RAVE, and remove all stars with Galactic latitudes $|b| < 5°$. We then resample the age distribution of our mock catalogue (primarily by reducing the number of young stars) to ensure we have enough stars for robust statistics across the entire range of stellar ages, and as a side-effect, roughly reproduce the age distribution of the extended solar neighbourhood.

Applying uncertainties to our mock catalogue

We then apply RAVE-like uncertainties to the output GALAXIA $T_{\rm eff}$, log g, and [M/H]. We first modify the output by drawing a value from a Gaussian centred at the true value, with a standard deviation generated by combining in quadrature the internal and external RAVE-like uncertainties for a given parameter. Both the internal and external uncertainties are determined as a function of the given parameter (for more details see Figure 5 of Wojno et al. 2017). Finally, we assign RAVE-like internal uncertainties to these modified values.

In addition to assigning the stellar parameters RAVE-like uncertainties, we also assign 2MASS-like uncertainties to the output apparent magnitudes (2MASS J, H, K_s), where the typical uncertainty is ~ 0.025 dex. Finally, we assign TGAS-like parallax uncertainties to the output parallaxes (0.3 mas, Gaia Collaboration et al. 2016; Lindegren et al. 2016).

Input versus output age comparison

After running our mock catalogue through the isochrone projection pipeline, we can compare the input (true) and output parameters. First, we check the input against output for stellar parameters ($T_{\rm eff}$, log g, [M/H]) and distances, and find they agree within the uncertainties given by the pipeline. Next, we consider the input and output age distributions. In Figure 4.1 we show comparisons between input and output ages, for different regions of the spectroscopic $T_{\rm eff}-\log g$ diagram. The top row shows the comparison for giant stars ($T_{\rm eff} < 5500$ K, $\log g < 3.5$), the middle row shows the same for main sequence stars ($\log g > 4.25$), and the bottom row shows turnoff stars ($T_{\rm eff} > 5500$ K, $3.5 < \log g < 4.25$. Panels in the left column are colour-coded by fractional age uncertainty, while panels on the right are colour-coded by absolute age uncertainty. The over plotted contours show the density distributions for 33, 67, 90, and 99 per cent of the sample.

From this comparison, we find that the giant and main sequence samples have much higher uncertainties overall compared to the turnoff sample, and are usually assigned intermediate ages, for any given input age. We find that for giant stars, their ages are extremely uncertain, in part due to large parallax uncertainties. While the main sequence sample performs slightly better, the effect is still too large to

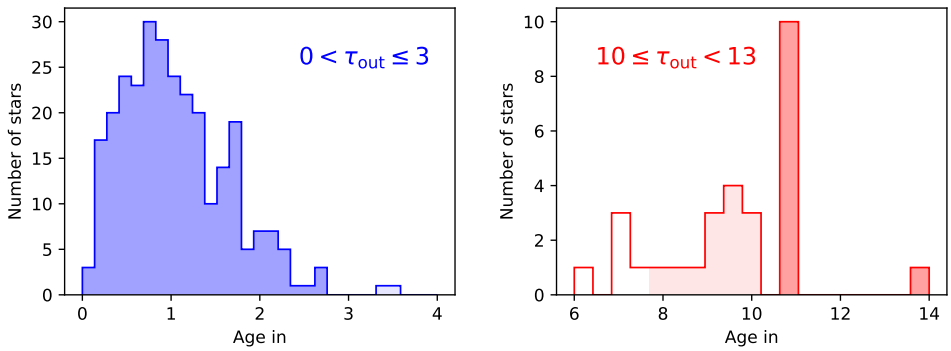

Figure 4.2 — Distribution of input ages for the stars with output ages given by the range indicated in the plot. The left panel shows the distribution for our 'young' sample, while the right panel shows the distribution for our 'old' sample. The darker shaded regions indicate stars with input ages that fall within the given bin, while the lighter shaded regions indicate stars with input ages that fall slightly outside of the given bin. A lack of shading indicates stars which are considered contaminants of that bin.

consider this sample for further analysis. These systematic trends in both the giant and main sequence samples also arise from the fact that the isochrones tend to be very close to each other in these regions, and with RAVE-like uncertainties, this leads to indeterminate age estimates. For turnoff stars, the isochrones are well separated (compared to the main-sequence and giant regions), and therefore stars in this region generally have smaller age uncertainties (see Figure 4.3).

In order to obtain a balanced sample with precise age estimates, for the analysis using the ages of RAVE stars we consider only two age bins: young ($0 < \tau < 3$ Gyr) and old ($10 < \tau < 13$ Gyr). We do not use intermediate age ($4 < \tau < 9$ Gyr) turnoff stars because we find a significant systematic offset for this age group. While this offset disappears if we only consider stars with output age uncertainties less than 20%, we find that this prunes the sample in a biased way. Intermediate age stars are more likely to have larger age uncertainties, simply due to the fact that their errors can span a much larger range, as stars on the edges of the isochrone grid (i.e., young or old stars) cannot have ages younger than $\tau = 0$ or older than $\tau = 13.8$.

Estimating contamination

Finally, although most stars in our young and old samples have fractional age uncertainties of ~ 40 per cent or less, it is necessary to also estimate the amount of contamination in these age bins. In Figure 4.2, we show the input age distributions for stars with output ages within either the young ($0 < \tau < 3$ Gyr) or old ($10 < \tau < 13$ Gyr) age bins. The dark shaded areas indicate where the input ages fall inside of the bin, and the lighter shaded regions indicate where the input ages fall outside of the bin, but could generally be considered 'young', or 'old' ($\tau \leq 4$ Gyr, and $\tau \geq 8$ Gyr, respectively). From this comparison, we estimate that our 'young' sample should have less than ~ 2 per cent contamination by stars older than 4 Gyr, and our 'old' sample should have less than ~ 20 per cent contamination by stars younger than 8 Gyr.

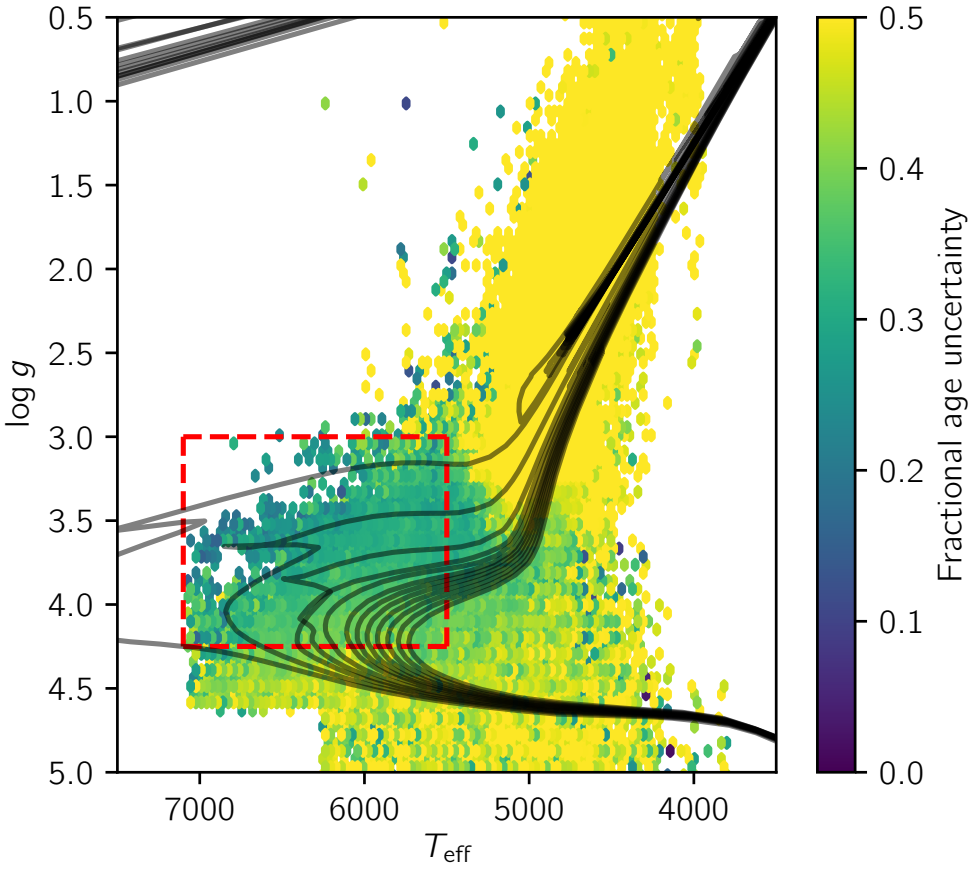

Figure 4.3 — Spectroscopic $T_{\rm eff}$–$\log g$ diagram of RAVE DR5 stars which satisfy the quality criteria listed in Sec. 4.2.5. The dashed red lines indicate the cuts made in the parameter space to select for only turnoff stars. The bins are colour-coded by the fractional age uncertainty.

4.2.4 Selection of our RAVE-TGAS sample

As a result of the comparison done with the mock sample (Figure 4.1), for the rest of our study we select only RAVE stars in the same turnoff region ($T_{\rm eff} < 5500$, $3.5 < \log g < 4.25$). This selection in $T_{\rm eff}$–$\log g$ space is shown in Figure 4.3 by the dashed red lines. Bins in Figure 4.3 are colour-coded by fractional age uncertainty, with solar-metallicity isochrones over plotted in black.

A histogram of the age uncertainties for this sample is shown in Figure 4.4. The majority of our sample (~ 60 per cent) has age uncertainties less than 2 Gyr, with a sizable fraction (~ 25 per cent) have age uncertainties less than 1 Gyr. This is an improvement over the whole RAVE-TGAS sample (dashed line in Figure 4.4), where half of the stars have age uncertainties greater than 3 Gyr. These large uncertainties are primarily due to two effects: (1) outside of the turnoff region, isochrones are stacked very closely together and therefore stars with RAVE-like uncertainties will

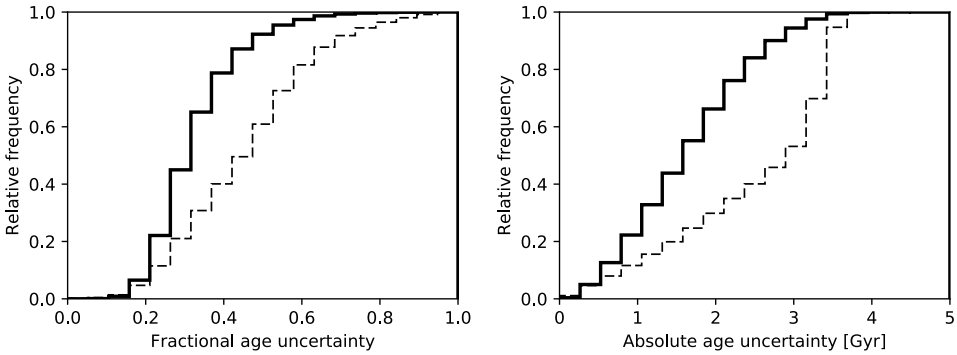

Figure 4.4 — Cumulative histogram of the fractional (left) and absolute (right) age uncertainties of our final selected sample of turnoff stars (solid line), and for the whole RAVE-TGAS sample (dashed line). The white plus indicates the position of the Sun.

therefore cross several isochrones, and (2) an increase in the parallax uncertainties, in particular for giant stars.

After making this selection in parameter space, our sample consists of 37 765 stars. The spatial distribution of our selected young and old populations is shown in Figure 4.5, with blue and red contours, respectively.

4.2.5 RAVE quality criteria

For this study, we apply the following quality criteria:

- `SNR_K` > 40
- `Algo_Conv_K` ≠ 1
- `CHISQ_c` < 2000
- `c1` = d, g, h, n, or o
- `c2` = d, g, h, n, o, or e
- `c3` = d, g, h, n, o, or e

These cuts ensure our stars in our sample have a high signal-to-noise ratio (`SNR_K`), their stellar parameters from the stellar parameter pipeline either converged, or oscillated between two values (`Algo_Conv_K`, Kordopatis et al. 2013a), and the fit from the chemical pipeline (Boeche et al. 2011) was reasonable. In addition, we remove peculiar stars flagged by the classification pipeline as having problems with their spectra (Matijevič et al. 2012).

After applying the quality criteria and dividing our RAVE sample into age bins, we are left with 31 976 stars, comprised of 6630 'young' stars, 1192 'old' stars, and 24 154 intermediate age stars, which we do not consider for any further analysis.

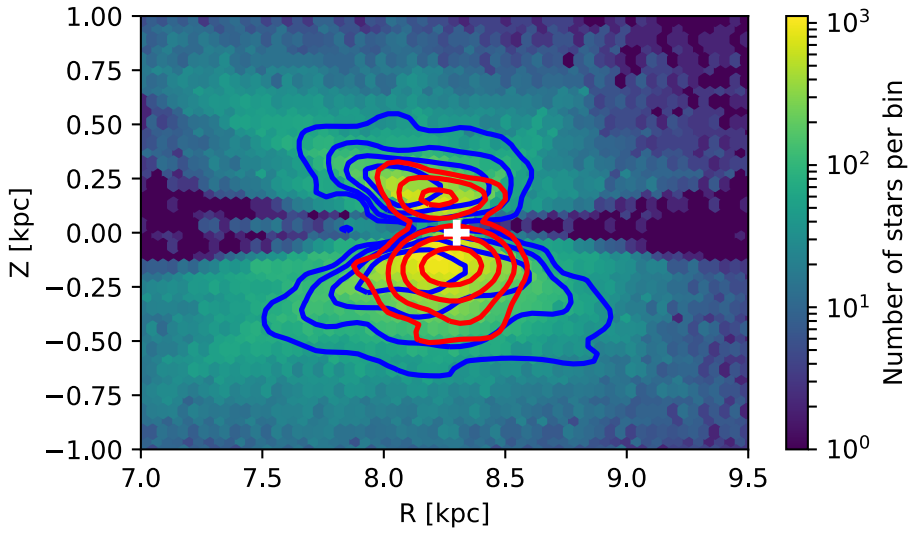

Figure 4.5 — Spatial extent of the selected young (blue contours) and old (red contours) turnoff stars. Contours indicate 33, 67, 90, and 99 per cent of each sample. The spatial extent and density of the entire sample is shown by the 2D histogram beneath.

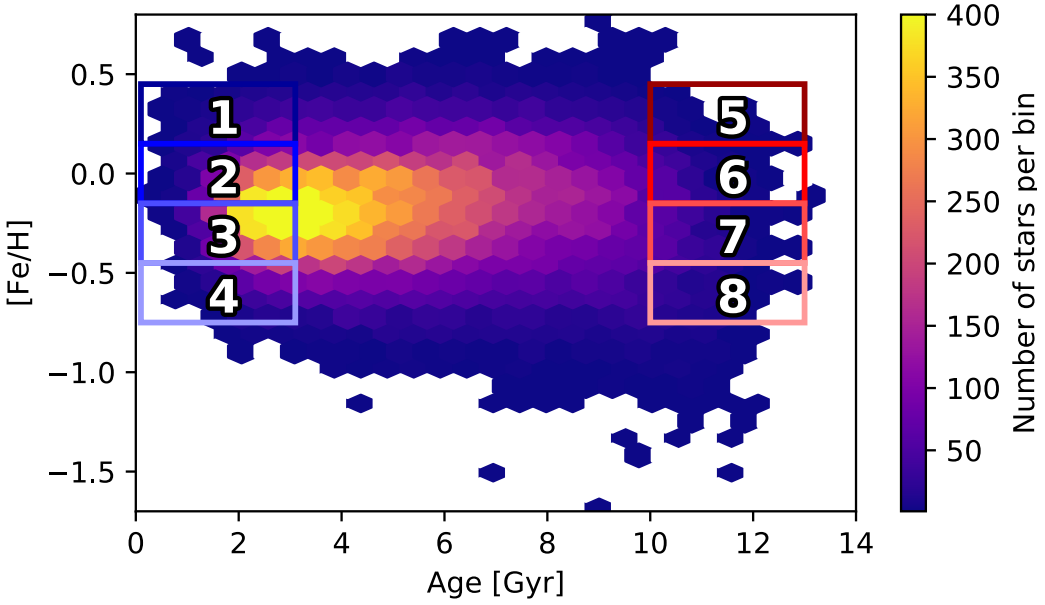

Figure 4.6 — Age v. [Fe/H] 2D histogram for our sample of turn off stars. We consider four metallicity bins for each age group, described in Section 4.3.

4.3 Kinematic trends as a function of age

To conduct our analysis, we divide each age group into four metallicity bins to explore differences between stellar populations arising from various epochs of the star formation history of the Galaxy, illustrated in Figure 4.6. Darker colours indicate more metal-rich bins, while lighter colours indicate more metal-poor bins. The bins are defined as follows:

- Bins 1 and 5: $0.15 \leq$ [Fe/H] < 0.45
- Bins 2 and 6: $-0.15 \leq$ [Fe/H] < 0.15
- Bins 3 and 7: $-0.45 \leq$ [Fe/H] < -0.15
- Bins 4 and 8: $-0.75 \leq$ [Fe/H] < -0.45

Throughout the rest of the text, we will refer to these bins by their number as shown in Figure 4.6.

4.3.1 Correcting by the selection function of RAVE

As RAVE is not a volume-complete survey, before we consider kinematic trends, we need to correct our sample by the selection function. The selection function of RAVE is summarized in Wojno et al. (2017) and references therein. However, our sample consists of only stars contained in both RAVE and TGAS, which had vastly different observing strategies and sky completeness, and therefore we reevaluate the selection function to take into account the overlap between RAVE and TGAS. To do this, we consider the selection function ($S_{\rm select}$) as a function of position on the sky in HEALPIX (Górski et al. 2005) pixels, $I_{\rm 2MASS}$ magnitude, and $(J-K_s)$ colour:

$$S_{\rm select}({\rm pixel}_{\alpha,\delta}) = \frac{\sum\sum {\rm N_{RAVE}}({\rm pixel}_{\alpha,\delta}, {\rm I}, {\rm J-K_s})}{\sum\sum {\rm N_{2MASS}}({\rm pixel}_{\alpha,\delta}, {\rm I}, {\rm J-K_s})}, \tag{4.1}$$

to obtain a completeness fraction for a given star in the combined RAVE-TGAS catalogue. This completeness fraction is then inverted to given a correction factor, which we apply when calculating velocity distributions and trends.

4.3.2 Velocity distributions

After dividing our sample according to the metallicity bins described in the previous section, we first look at the cylindrical velocity distributions in the solar neighbourhood (Figure 4.7). We determine Galactocentric space velocities in cylindrical coordinates following Appendix A of Williams et al. (2013), and note that we assume the position of the Sun to be $(R_0, Z_0) = (8.3, 0)$ kpc, and a local standard of rest (LSR) of $V_{\rm LSR} = 240$ km s^{-1}, following Schönrich (2012), with the solar peculiar velocity with respect to the LSR adopted from Schönrich et al. (2010), $({\rm U, V, W})_\odot = (11.10, 12.24, 7.25)$ km s^{-1}. For our analysis, we define our reference frame to have positive $V_{\rm R}$ away from the Galactic centre, positive V_ϕ is in the direction of Galactic rotation, and positive V_Z towards the north Galactic pole.

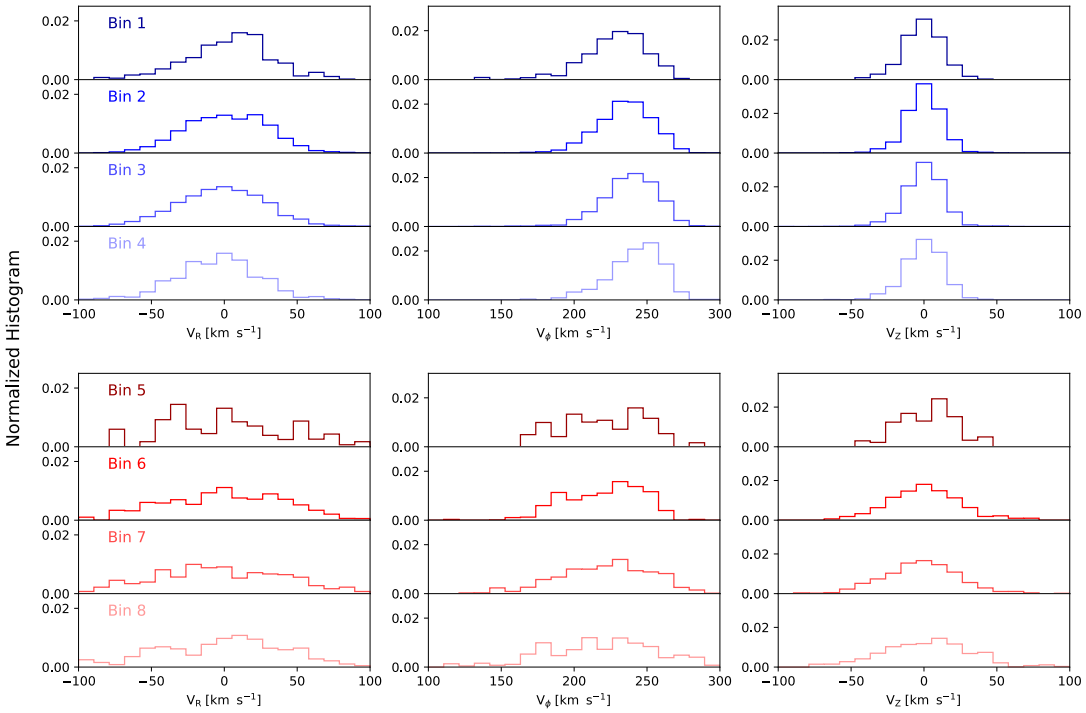

Figure 4.7 — Cylindrical velocity distributions (left to right: V_R, V_ϕ, V_Z) for our two age bins. Young stars are plotted in blue, old stars are plotted in red. More metal-rich bins are plotted with darker colours, with more metal-poor bins in lighter colours (metallicity bins 1, 2, 3, and 4 for young stars, and bins 5, 6, 7, and 8 for old stars).

Radial velocities are provided by RAVE DR5 (Kunder et al. 2017), and proper motions are taken from the UCAC5 catalogue (Zacharias et al. 2017), which offers considerable improvements over UCAC4 (Zacharias et al. 2013) and TGAS (Lindegren et al. 2016) proper motions by utilizing position data available from Gaia DR1 (Gaia Collaboration et al. 2016) for over 107 million stars.

In Figure 4.7, we show the distributions for both the young (blue, top row), and old (red, bottom row) stars, for each of the metallicity bins shown in Figure 4.6, for each component of the Galactocentric space velocity in cylindrical coordinates (V_R, V_ϕ, V_Z shown in the left, middle, and right columns, respectively). The parameters for each of these histograms are given in Table 4.1. Means and velocity dispersions are calculated as the weighted mean:

$$\overline{x}^* = \frac{\sum_{i=1}^{n} (x_i \times w_i)}{\sum_{i=1}^{n} w_i}, \tag{4.2}$$

and the weighted dispersion, where the unbiased, weighted variance is:

Table 4.1 — Mean and dispersion for each component of the Galactocentric cylindrical velocity, for both age groups and each metallicity bin within the age group.

Bin number	Metallicity range	N	$\langle V_R \rangle$	σ_R	$\langle V_\phi \rangle$	σ_ϕ	$\langle V_Z \rangle$	σ_Z
Young								
1	$0.15 \leq$ [Fe/H] < 0.45	386	0.5 ± 1.3	30.3 ± 1.1	229.3 ± 1.0	23.6 ± 0.8	-2.4 ± 0.5	12.8 ± 0.5
2	$-0.15 \leq$ [Fe/H] < 0.15	2534	2.1 ± 0.4	27.2 ± 0.4	234.0 ± 0.3	18.4 ± 0.3	-0.2 ± 0.2	12.9 ± 0.2
3	$-0.45 \leq$ [Fe/H] < -0.15	3141	-1.8 ± 0.4	30.1 ± 0.4	237.7 ± 0.3	18.6 ± 0.2	-0.3 ± 0.2	13.2 ± 0.2
4	$-0.75 \leq$ [Fe/H] < -0.45	542	-5.6 ± 1.0	29.2 ± 0.9	243.2 ± 0.6	18.0 ± 0.5	0.1 ± 0.5	12.6 ± 0.4
Old								
5	$0.15 \leq$ [Fe/H] < 0.45	71	3.6 ± 5.0	46.6 ± 3.9	219.2 ± 3.0	27.6 ± 2.3	1.8 ± 2.0	18.5 ± 1.5
6	$-0.15 \leq$ [Fe/H] < 0.15	339	0.9 ± 2.0	43.2 ± 1.7	220.8 ± 1.3	27.4 ± 1.0	0.9 ± 1.1	24.8 ± 1.0
7	$-0.45 \leq$ [Fe/H] < -0.15	439	-1.4 ± 1.9	46.7 ± 1.6	219.6 ± 1.3	32.7 ± 1.1	-2.3 ± 1.0	25.6 ± 0.8
8	$-0.75 \leq$ [Fe/H] < -0.45	260	-5.3 ± 2.6	50.9 ± 2.2	215.8 ± 1.9	38.1 ± 1.7	2.6 ± 1.6	31.7 ± 1.4

$$\sigma_x^{*2} = \frac{\sum_{i=1}^{n} w_i (x_i - \overline{x}^*)^2}{k \sum_{i=1}^{n} w_i}, \tag{4.3}$$

where $k = (N' - 1)/N'$, and N' is the number of non-zero weights.

We note that σ represents the velocity dispersion corrected for the observational uncertainties:

$$\sigma_{R,\phi,Z} = \sqrt{\sigma^{*2}_{R,\phi,Z} - \langle \mathrm{e}_{V_{R,\phi,Z}} \rangle^2}. \tag{4.4}$$

We find significant differences between our young and old populations, and between the different metallicity bins within each age group. In our sample of young stars, we see no significant differences for the mean radial (V_R) and vertical (V_Z) velocity distributions for different metallicity bins. However, we do find a shift in the mean azimuthal velocity (V_ϕ) distributions as a function of metallicity. We find that as metallicity increases, the average V_ϕ decreases, such that our young, metal-rich stars (bin 1) lag the LSR ($\langle \mathrm{V}_\phi \rangle = 229.3 \pm 1.0$ km s^{-1}) more than the stars in any other metallicity bin. A negative correlation between metallicity and V_ϕ for thin disc (young) stars has been found in a number of studies probing different volumes in the solar vicinity (e.g. Lee et al. 2011; Adibekyan et al. 2013; Recio-Blanco et al. 2014; Wojno et al. 2016; Kordopatis et al. 2017), with measurements ranging from $\partial V_\phi / \partial [\mathrm{M/H}] = -23$ km s^{-1}dex^{-1} to -11 km s^{-1}dex^{-1}.

For our sample, we measure $\partial V_\phi / \partial [\mathrm{M/H}] \approx -7$ km s^{-1}dex^{-1}, shallower than measurements from the literature, however, we note that we do not explicitly separate our sample into thin and thick disc stars, so some contamination is possible. We also find that the dispersion of the azimuthal velocity distribution decreases as metallicity decreases, with bin 1 having a dispersion $\sigma_\phi = 23.6 \pm 0.8$ km s^{-1}and bin 4 having $\sigma_\phi = 18.0 \pm 0.5$ km s^{-1}.

For old stars, we find much broader distributions compared to our young stars, which indicates that the older populations of stars in our sample are more kinematically hot, as expected (e.g., Nordström et al. 2004). When we consider the different metallicity bins, we find that for all velocity components, the dispersion of a distribution increases with decreasing metallicity. This difference in the dispersions agrees globally with e.g. Guiglion et al. (2015) (and in particular for the difference in dispersions between young and old populations), but with a slightly different scale. In addition, we find a correlation between metallicity and mean V_ϕ, such that the more metal-poor a sample is, the more it lags behind the LSR, in agreement with previous studies (e.g. Kordopatis et al. 2011; Adibekyan et al. 2013; Kordopatis et al. 2013b; Wojno et al. 2016; Kordopatis et al. 2017). However, we measure a relatively shallow gradient, $\partial V_\phi / \partial [\mathrm{M/H}] \approx 5$ km s^{-1}dex^{-1}, while measurements from the literature range from 42 km s^{-1}dex^{-1} to 51 km s^{-1}dex^{-1}. We interpret this disparity as a result of contamination of old thin disc stars, as we do not explicitly separate our sample according to their likelihood of belonging to either the thin or thick disc.

To investigate the kinematics of our two age groups further, we now consider velocity trends as a function of Galactocentric radius (R).

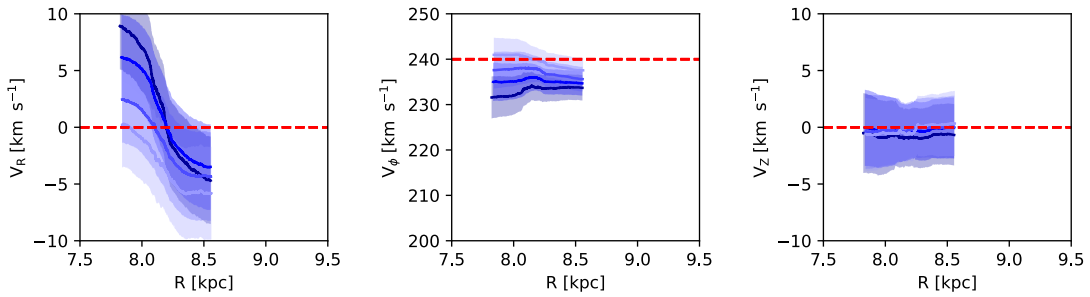

Figure 4.8 — Velocity trends as a function of Galactocentric radius (left to right: V_R, V_ϕ, V_Z) for our young stars. The most metal-rich bin is plotted in dark blue, and the most metal-poor bin light blue, as defined in Section 4.3.

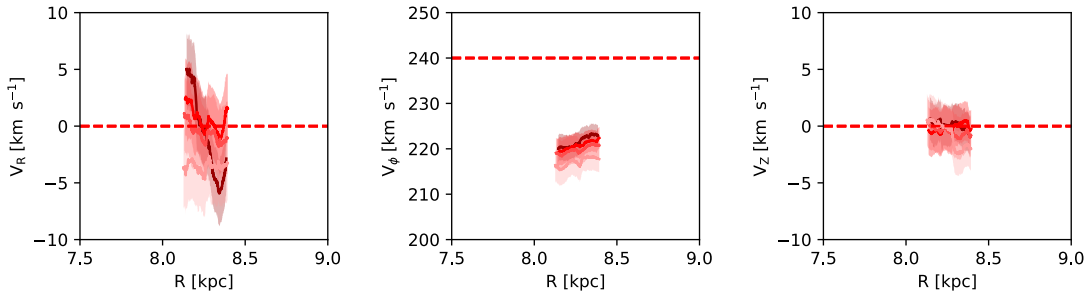

Figure 4.9 — Velocity trends as a function of Galactocentric radius (left to right: V_R, V_ϕ, V_Z) for our old stars. The most metal-rich bin is indicated with dark red, and more metal-poor bins with pink and light pink, respectively.

4.3.3 Velocity trends as a function of Galactocentric radius

In Figures 4.8 and 4.9, we show trends in V_R, V_ϕ, V_Z as a function of Galactocentric radius R. Trends are calculated as the rolling weighted mean, where the size of the rolling windows are determined as a function of number of stars in a given bin. More metal-rich bins are shown in darker blue, with metallicity decreasing in successively lighter blue.

Young stars

For our metal-rich young stars (bin 1), we find a significant negative gradient in $\langle V_R \rangle$ as a function of R, which we measure as -22.8 ± 0.3 km s^{-1} kpc^{-1}. Qualitatively, this trend shows stars in the inner Galaxy moving outwards towards the solar neighbourhood, and stars in the outer Galaxy moving inward. This trend smoothly flattens for successively more metal-poor bins, with the most metal-poor bin showing the least dependence as a function of R. For bins 1,2, and 3, the trends we find are steeper than those found in the literature (-3 km s^{-1} kpc^{-1} from Siebert et al. (2011a); -8 km s^{-1} kpc^{-1} from Williams et al. (2013); and -6.6 ± 0.7 km s^{-1} kpc^{-1} from Bovy (2017)), and we discuss the possible reasons for this difference in Section 4.5.

In the azimuthal velocity component (V_ϕ), the offset shown in Figure 4.7 is clearly represented here, with an offset between each metallicity bin at nearly all

Table 4.2 — Measured radial velocity gradients for each age group and metallicity bin.

Bin Number	$\partial\langle V_R\rangle/\partial R$ km s^{-1} kpc^{-1}
Young	
1	-22.8 ± 0.3
2	-16.9 ± 0.2
3	-12.0 ± 0.2
4	-10.1 ± 0.2
Old	
5	-14.0 ± 1.0
6	-1.7 ± 0.6
7	-0.6 ± 0.4
8	1.4 ± 0.7

Galactocentric radii. For bin 1, the most metal-rich bin, we find a slight increase in mean azimuthal velocity as a function of R, a trend which gradually reverses, such that the most metal-poor bin shows a slight negative trend in mean velocity as a function of R. These results are roughly consistent with those presented in Rojas-Arriagada et al. (2016, their Figure 8), where our young stars correspond to their thin disc, and old stars correspond to their thick disc.

Finally, for the vertical velocity component V_Z, we measure flat trends consistent with 0 km s^{-1}.

Old stars

Figure 4.9 shows the same as Figure 4.8, but now for our sample of old stars. We find that for $\partial\langle V_R\rangle/\partial R$, we find similar trends as in the young stars, such that the most metal-rich bin has a steeper gradient (bin 5, $\partial\langle V_R\rangle/\partial R = -14.0 \pm 1.0$ km s^{-1} kpc^{-1}, than the most metal-poor bin (bin 8, 1.4 ± 0.7 km s^{-1} kpc^{-1}). However, for our old stars, none of the metallicity bins have a gradient as steep as that found for young, metal-rich (bin 1) stars. When we consider the azimuthal velocity component of our old stars, we find that they all lag the LSR by $\sim$ 20 km s^{-1}. As with the young populations, we find generally flat trends for the vertical velocity component, consistent with 0 km s^{-1} within the error bars.

4.3.4 Orbital parameters

Orbits for our sample of stars are calculated using the GALPY (Bovy 2015) python package, and we choose the MWPotential2014 as our Galactic potential for orbital integration. As a result, we obtain estimates for the orbital eccentricity (e), guiding radii (R_G), and the maximum height above the plane ($Z_{\rm max}$) for each star. In Figure 4.10, we show the eccentricity distributions for our young (left panel) and old stars (right panel), divided into bins of metallicity.

Eccentricities

We find that the eccentricity distribution of our young stars peaks at $e = 0.12$ if we take the average of all metallicity bins, but we note that the mean does shift to smaller values with decreasing metallicity ($\overline{e} = 0.14$ for Bin 1, compared to $\overline{e} = 0.11$ for Bin 4). We also find that the dispersion of each distribution decreases slightly with decreasing metallicity.

For our old population, we find larger mean eccentricities compared to the young population for all metallicity bins, peaking at $e = 0.20$ if we take an average of all metallicity bins. In contrast to the young population, we find the mean eccentricity *increases* with decreasing metallicity, from $\overline{e} = 0.19$ for bin 5 to $\overline{e} = 0.23$ for bin 8. The eccentricity distributions for our old stars are also much broader than those of the young stars, with an average dispersion $\sigma_e = 0.11$ (typical of the thick disc, see Kordopatis et al. 2011) compared to $\sigma_e = 0.07$ (typical of the thin disc) for the young stars. In addition, we find that the dispersion of the eccentricity distribution increases with decreasing metallicity, in contrast to what we find for young stars, and in line with the kinematic trends found in the previous section.

Guiding radii

The distributions of guiding radii for our young and old samples, are shown in Figure 4.11. Young stars have mean guiding radii further closer to the solar neighbourhood compared to old stars, which have guiding radii towards the inner disc. The dispersion in radii is also larger for old stars. In addition, for young stars, we find an increase in guiding radii as a function of decreasing metallicity, corresponding to the results shown for V_ϕ in Figure 4.10. Combined with the velocity trends and eccentricities, we find that overall young stars have cooler kinematics, with the most metal-rich young stars originating from the inner disc on slightly more eccentric orbits. Young, metal- poor stars arrive to the solar neighbourhood primarily from the outer disc on more circular orbits. Old stars are more kinematically hot, with larger dispersions in all components of their velocities, more eccentric orbits, and come from a more centrally-concentrated region of the disc.

Maximum height above the plane

In Figure 4.12, we show the distributions of $Z_{\rm max}$ for our young and old stars. We find that our young stars are more confined to the plane, with all metallicity bins having similar means ($\overline{Z}_{\rm max} = 0.31 - 0.33$ kpc). In contrast, we find that the orbits of old stars extend to larger heights above the plane, with a signficant difference between the most metal-rich (bin 5, $\overline{Z}_{\rm max} = 0.3$ kpc), and the most metal-poor bin ($\overline{Z}_{\rm max} = 0.52$ kpc). In addition, the distributions are much more skewed with longer tails, having larger $\sigma_{Z_{\rm max}}$ compared to young stars.

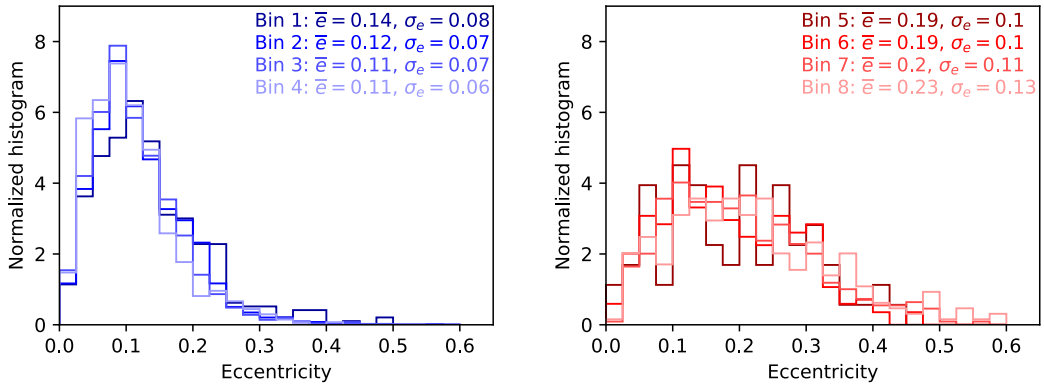

Figure 4.10 — Orbital eccentricities for our sample of young (left) and old (right) stars. Bins in metallicity are defined in Section 4.3.

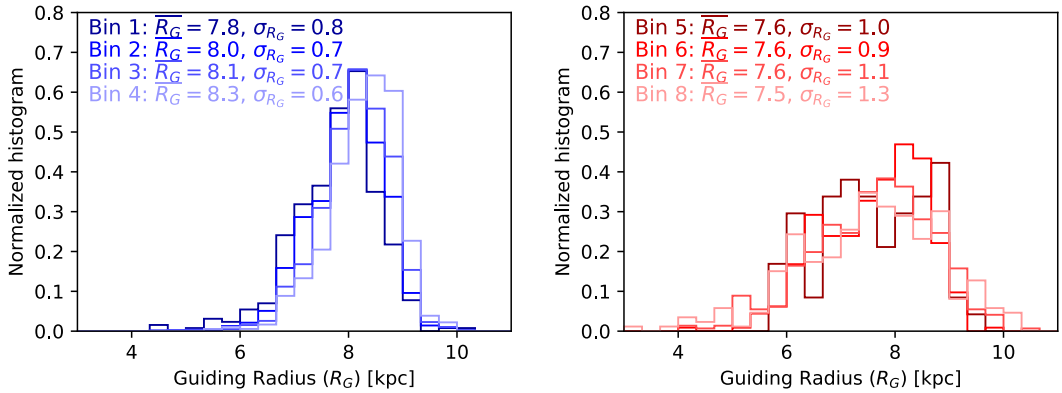

Figure 4.11 — Distributions of guiding radii for our sample of young (left) and old (right) stars. Bins in metallicity are defined in Section 4.3.

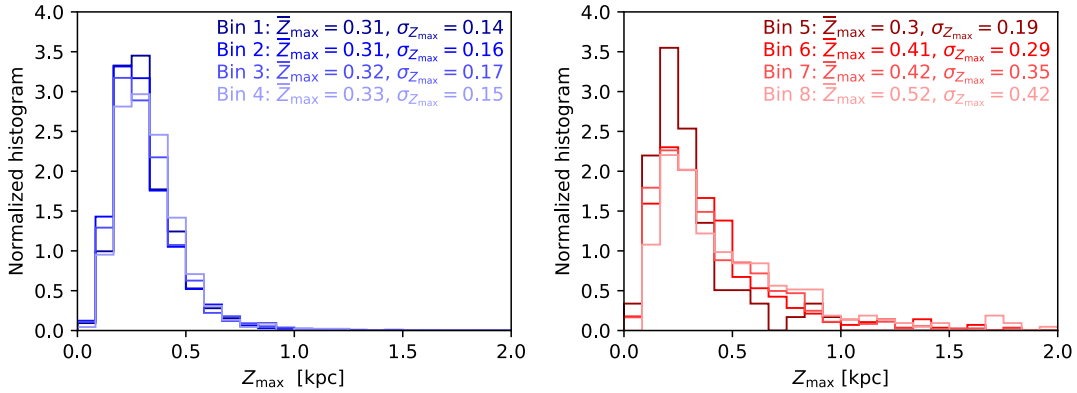

Figure 4.12 — Maximum height above the plane ($Z_{\rm max}$) for our sample of young (left) and old (right) stars. Bins in metallicity are defined in Section 4.3.

4.4 Discussion

4.4.1 Radial velocity gradient for young stars vs. old stars

We find significant differences in the kinematics of our young and old samples in our selection of RAVE-TGAS turnoff stars. When we consider the mean kinematics of these samples, in all components of the Galactocentric cylindrical velocity, we find that our younger sample is kinematically cooler than our old sample, and we find steeper velocity gradients in young stars compared to old stars. For both old and young stars, we find trends in radial velocity as a function of Galactocentric radius, $\partial\langle V_{\rm R}\rangle/\partial R$. Within each age group, we find that the most metal-rich stars have steeper gradients than more metal-poor stars, with smooth transitions between the bins. The gradient that we measure for the most metal-rich bins ($0.15 \leq$ [Fe/H] < 0.45, -22.8 ± 0.3 km s^{-1} kpc^{-1} for the young stars and -14.0 ± 1.0 km s^{-1} kpc^{-1} for the old stars, respectively) is significantly steeper than previous measurements in the literature.

A radial velocity gradient as a function of R was first discovered in Siebert et al. (2011a), where they measured a value of ~ -3 km s^{-1} kpc^{-1} for a sample of RAVE stars. Siebert et al. (2011a) conclude that this effect is a signature of non-axisymmetric components of the Galactic potential including the bar, spiral arms, warp of the disc, a triaxial dark matter halo, or some combination of these components. In Siebert et al. (2012), they explore the contribution of solely spiral arms, and find that the observed trends could be fit with a model with a pattern of two spiral arms.

This finding was verified by Williams et al. (2013), where they investigated asymmetries in the kinematics of the local disc using a sample of RAVE red clump stars. They find a gradient consistent with previous results, and measure a slightly steeper value for a subsample of stars below the plane ($-1 < Z < -0.5$ kpc): $\partial\langle V_{\rm R}\rangle/\partial R = -8$ km s^{-1} kpc^{-1}, with a very shallow or non-existent gradient above the plane. Carillo et al. (in prep.) conducted an updated version of this analysis using improved distance estimates, and measure a radial velocity gradient consistent with Williams et al. (2013), with a steeper gradient in the Northern hemisphere compared to the Southern hemisphere, but note that the value depends on proper motion catalogue used. They conclude that the radial gradient they find is a signature of the presence of spiral structure in the disc (e.g. Faure et al. 2014).

Bovy (2017), using distance and proper motion data from nearby (within ~ 230 pc) Gaia-TGAS main sequence stars, measured $\partial V_{\rm R} \,/\, \partial R = -6.6 \pm 0.7$ km s^{-1} kpc^{-1}, consistent with results from Williams et al. (2013), but note the fact that their gradient measurement eliminates models with a triaxial bulge or halo having closed, elliptical orbits. Specifically, $\partial V_{\rm R} \,/\, \partial R = K + C$, where K and C are Oort constants related to the shape of the Galactic potential (Oort 1927b,a). The value of K is related to the local divergence of the velocity field, and C represents the radial shear (Olling & Dehnen 2003). With $\partial V_{\rm R} \,/\, \partial R = -6.6 \pm 0.7$, K and C are both negative (Bovy 2017), which is inconsistent with certain triaxial bulge and halo models (Kuijken & Tremaine 1994; Bovy 2015). In addition, they find that kinematically colder populations are more affected by disc asymmetries.

Monari et al. (2014) compared observational results to a model, with the aim of characterizing the contribution of the bar on the local velocity field. They find that if the Sun is located near the outer Lindblad resonance (OLR, Dehnen 1998; Antoja et al. 2014; Monari et al. 2017b), stars with guiding radii (R_G) close to $R_{\rm OLR}$ have their orbits stretched, with the strength of the effect growing as a function of proximity to $R_{\rm OLR}$. They show that due to our position in the disc ($R_0 > R_{\rm OLR}$, $\phi < 0$), we measure a negative gradient in $V_{\rm R}$. They reproduce the result found by Williams et al. (2013), and measure a steeper gradient than those produced by the models. Faure et al. (2014) also attempt to explain the observed gradient with a focus on determining if the spiral arms greatly affect the local velocity field, by using a model that includes contributions from both the bar and spiral arms. They find non-zero mean radial velocities, indicating net velocity flows due to the presence of the spiral arms. In particular, within corotation, they find stars within the arms move radially towards the Galactic Centre, and between the arms, stars move towards the anticentre. This trend is reversed outside of corotation. These trends are consistent with the model presented in Monari et al. (2016), where they show that a spiral potential produces variations in radial velocity of the order of the radial velocity gradient observed in the solar neighbourhood.

While our results for the most metal-rich samples in our selection of turnoff stars are in contention with the results from the literature ($-3\,{\rm km\,s^{-1}\,kpc^{-1}}$ from Siebert et al. (2011a), $-8\,{\rm km\,s^{-1}\,kpc^{-1}}$ from Williams et al. (2013), and $-6.6 \pm 0.7\,{\rm km\,s^{-1}\,kpc^{-1}}$ from Bovy (2017)), we do reproduce similar results if we perform our analysis on red clump or main sequence stars only. This raises the question: why should the kinematics of local turnoff stars differ from main sequence or giant stars?

One possible reason may be due to our age selection. On the main sequence and in the giant branch, it is difficult to determine accurate ages from isochrone fitting. Therefore, for the previous results in the literature, we would consider their samples to have stars with ages spanning a large range. Indeed, red clump stars are known to span a large range of intermediate ($\sim 2-9$ Gyr) ages, although they are more biased towards young ages (Girardi 2016). Therefore, we suggest that considering the age of a sample is crucial when attempting to investigate kinematic trends in the solar neighbourhood. By selecting samples of strictly young (typically kinematically cold) or old (kinematically hot) stars, we probe the strength of the effect of asymmetric disc components on populations that are the result of different star formation histories at different epochs, as they are linked through the age-velocity dispersion relation (Wielen 1977; Holmberg et al. 2007; Casagrande et al. 2011, e.g.). Indeed, we find signatures of the Hercules stream (associated with the bar) in both the young and old stars, but the Hyades (associated with the spiral arms) affects only young stars (see Section 4.4.2 and Figure 4.13).

4.4.2 Radial velocity gradient as a function of metallicity

In addition to confirming the presence of this radial velocity gradient, we find a significant difference in the $\partial\langle V_{\rm R}\rangle/\partial R$ gradient between our most metal-rich (bin1, $0.15 \leq$ [Fe/H] < 0.45, $\partial\langle V_{\rm R}\rangle\ /\ \partial R = -22.8 \pm 0.3\,{\rm km\,s^{-1}\,kpc^{-1}}$), and most metal-

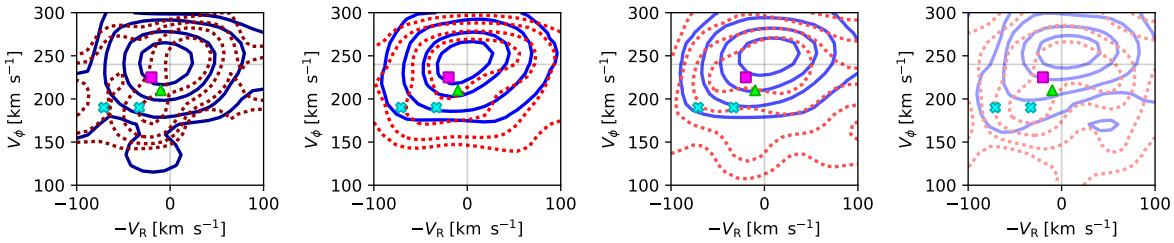

Figure 4.13 — $V_R - V_\phi$ space for our sample of young (blue, solid) stars and old (red, dashed), split into the four metallicity bins shown in Figure 4.6. Contours show the density distributions for 33, 67, 90, and 99 per cent of the sample for each bin.

poor bin (bin 4, $-0.75 \leq$ [Fe/H] < -0.45, $\partial\langle V_R\rangle/\partial R = -10.1 \pm 0.2$ km s^{-1} kpc^{-1}), for both young and old stars. To explore the source of this difference, we examine overdensities in $V_R - V_\phi$ space, shown in Figure 4.13. Contours are shown for both young (blue, solid) and old (red, dashed) age groups, with the most metal-rich bin shown on the left, and the most metal-poor bin on the right. Literature values for the Hercules (cyan cross), Hyades (magenta square), and Pleiades (green triangle) moving groups are overplotted (Dehnen 2000; Binney & Tremaine 2008). We find that stars in our most metal-rich bin have a greater contribution from stars potentially associated with a low velocity mode (Hercules stream), which is typically explained as a signature of a bar that affects the orbits of stars near the OLR (Dehnen 2000; Fux 2001), and is dominated by metal-rich thin disc stars (Ramya et al. 2016; Antoja et al. 2017), due to the metallicity gradient in the disc.

In addition to the contribution from the Hercules moving group, which is found in all metallicity bins, we find that our metal-rich bins have a peak in $V_R - V_\phi$ space near the position of the Hyades moving group. The Hyades are metal-rich, and are typically associated with spiral structure (Quillen & Minchev 2005; Famaey et al. 2008; Antoja et al. 2017). We note that for our young stars, as we move to more metal-poor subsamples, the position of the peak in $V_R - V_\phi$ space moves farther away from Hercules, indicating less of a contribution from this moving group. As the Hercules and Hyades streams have been found to be metal-rich (e.g. Famaey et al. 2008; Ramya et al. 2016), we expect to see them most prominently in the metal-rich bins of our sample, and the flattening of the radial velocity gradient as a function of decreasing metallicity is due to the decreasing contribution from the Hercules stream. Furthermore, with the observed radial metallicity gradient in the disc (∂[Fe/H]/∂R~ -0.06 dex kpc^{-1}, e.g. Genovali et al. 2014; Anders et al. 2017), we can roughly correlate metallicity with guiding radius (Antoja et al. 2017). Our findings are then roughly consistent with the model of Monari et al. (2017a), which reproduces features of the local velocity field using a model of the Galactic potential with a fast bar, and shows that the location of these features shifts as a function of Galactocentric radius (see their Figure 4). Moving further from the OLR decreases the contribution of the Hercules stream, similar to what we find for our more metal-poor stars.

To further explore this hypothesis, in Figure 4.14 we show the V_ϕ distributions of both young and old samples in our four metallicity bins, at different Galactocentric

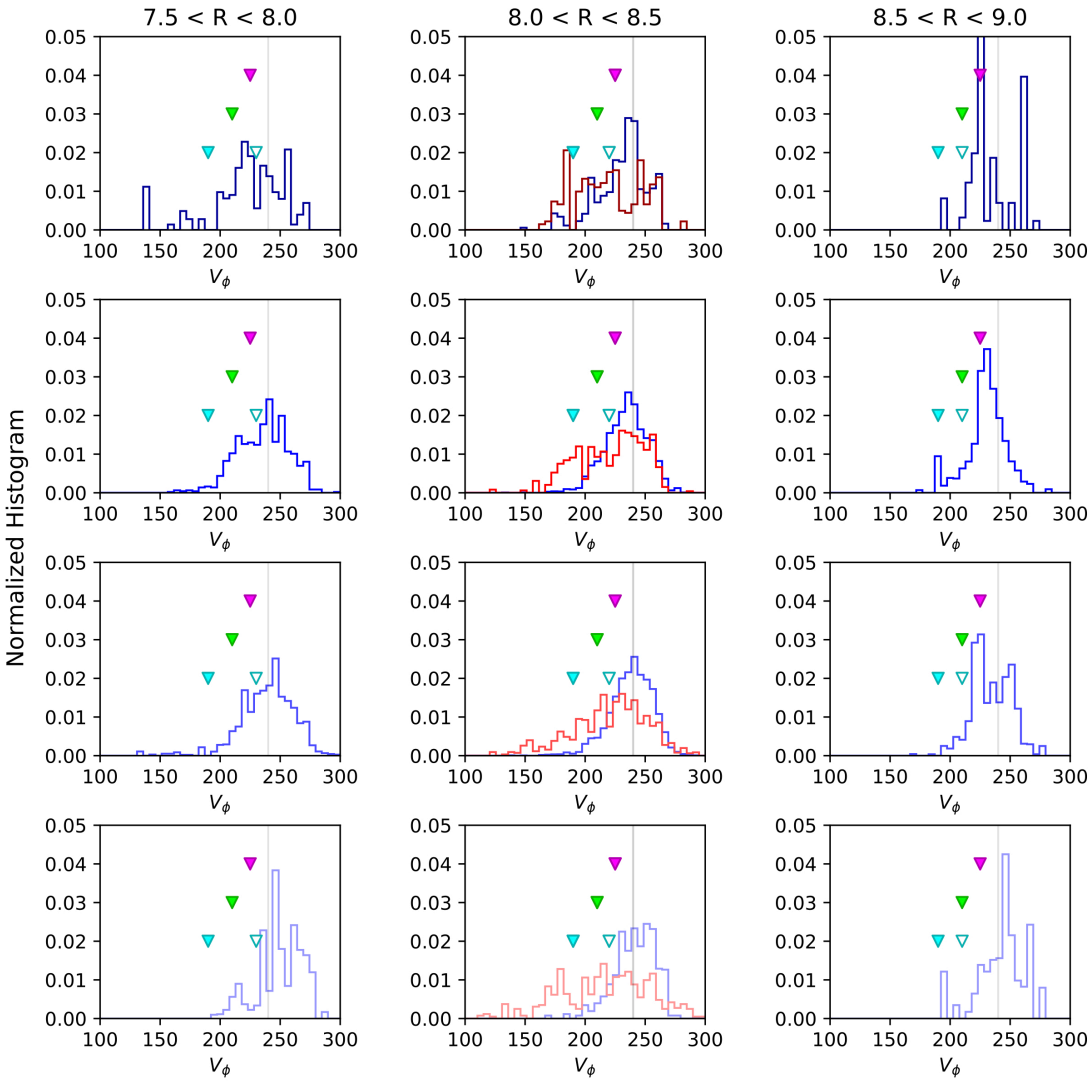

Figure 4.14 — V_ϕ distributions for our sample of young (blue) and old (red) stars, split into the four metallicity bins shown in Figure 4.6. The most metal-rich bin is shown on the top row, and the most metal-poor bin on the bottom row. Each column represents a different bin in Galactocentric radius. The positions of the three moving groups we consider are shown as filled triangles (cyan, green, and magenta for Hercules, Pleiades, and Hyades, respectively.) The unfilled triangles indicate the approximate position of the gap in velocity space due to the Hercules stream, from Antoja et al. (2014).

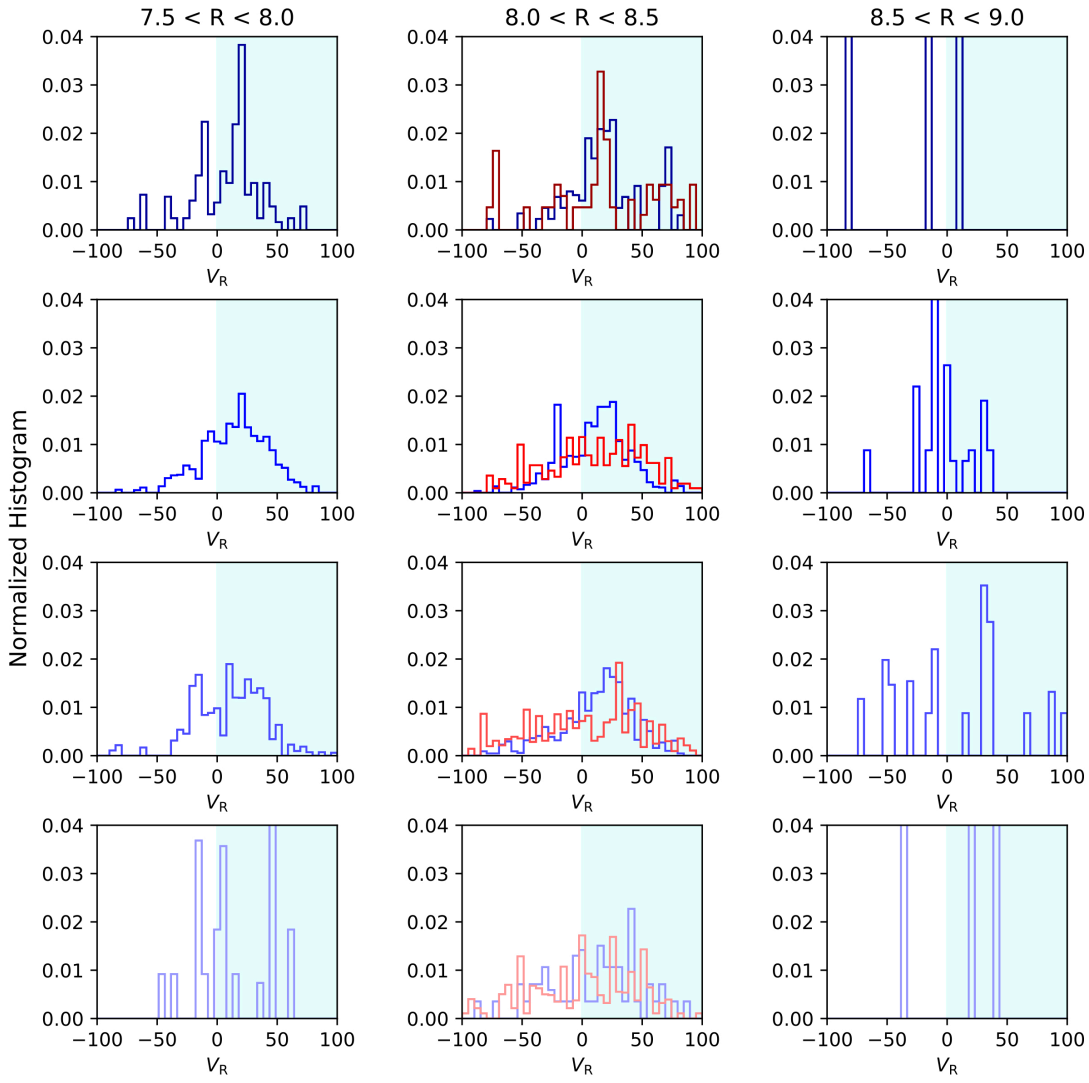

Figure 4.15 — V_R distributions for our sample of young (blue) and old (red) stars that we associate with the Hercules stream for a given Galactocentric radius (see Figure 4.14), split into the four metallicity bins shown in Figure 4.6. The most metal-rich bin is shown on the top row, and the most metal-poor bin on the bottom row. Shaded cyan regions indicate where we would expect the most contribution from Hercules stream stars.

radii. Young stars are plotted in blue, old stars in red, with the leftmost column showing stars inward of the solar neighbourhood (7.5 < R < 8.0), the middle column centred on the solar neighbourhood (8.0 < R < 8.5), and the rightmost column showing stars towards the outer disc (8.5 < R < 9.0). We recall that the older stars span a smaller volume than young stars, due to the fact that older stars are always less luminous than young stars for a given temperature in the turnoff region, and therefore cannot be seen to the same distances as bright, young stars. We also mark the mean V_ϕ positions of the Hercules, Pleiades, and Hyades moving groups (cyan, green, and magenta filled triangles, respectively). The unfilled triangle represents the approximate position of the gap in velocity space due to the Hercules moving

group from Antoja et al. (2014, see their Figure 5), which varies as a function of Galactocentric radius.

In Figure 4.15 we plot the V_R distributions for only stars associated with the Hercules stream (V_ϕ less than that of the gap due to the Hercules steam for a given Galactocentric radii). The cyan shaded regions indicate where we would assume the greatest contributions from the Hercules stream. Indeed, we find that for our most metal-rich bins, the majority of the stars we would associate with Hercules from their V_ϕ velocities also have V_R velocities consistent with the Hercules moving group. This contribution decreases as the metallicity decreases, but some indication of Hercules stream stars is found for all metallicity bins. When we consider different bins in Galactocentric radii, we notice that the effect is weaker for the middle and right columns, although we avoid drawing strong conclusions from this finding due to small number statistics for stars outside of the solar neighbourhood.

4.4.3 V_ϕ vs. R trends

In addition to the impact of the bar and spiral on the velocity trends we find, we recall that when we consider the mean azimuthal velocity as a function of Galactocentric radius ($\partial\langle V_\phi\rangle/\partial R$), we find that for our young sample, metal-rich stars (bin 1) lag the LSR more than metal-poor stars. This trend is usually attributed to the presence of stars born in the inner Galaxy visiting the solar neighbourhood (e.g. Lee et al. 2011; Adibekyan et al. 2013; Recio-Blanco et al. 2014; Allende Prieto et al. 2016; Wojno et al. 2016). If the radial metallicity gradient of the disc is steep (e.g. Haywood et al. 2013; Halle et al. 2015), this trend may be explained simply as the effect of blurring– stars reaching the solar neighbourhood are more likely to be close to the apocentre of the epicyclic orbits, and therefore have slower azimuthal velocities compared to the LSR.

However, this trend is not as strong as what we would expect from blurring alone– some stars present in the solar neighbourhood have had their orbits altered by churning, which increases their guiding radii with no change in angular momentum (Sellwood & Binney 2002; Kordopatis et al. 2015a). Indeed, when we consider their eccentricities and guiding radii, we find they have slightly more eccentric orbits than more metal- poor stars, with guiding radii inward of the solar radius. This provides an indication that some of these stars have experienced blurring, but a large fraction have orbits that are still circular, and therefore must have been affected by churning to bring them to the solar neighbourhood. This picture is consistent with that presented in Antoja et al. (2017), where they find a positive gradient in V_ϕ as a function of metallicity, for stars moving both towards and away from the solar neighbourhood. They propose that these stars are migrators from the inner disc with circular velocities close to the LSR.

4.5 Conclusions

From our study of the kinematics of distinct age groups in the solar neighbourhood as a function of metallicity and Galactocentric radius R, we reach the following conclusions:

- Overall, we find negative radial velocity gradients as a function of Galactocentric radii, and measure steeper gradients than those found before for RAVE red clump stars (Siebert et al. 2011a; Williams et al. 2013). The source of the negative gradient in $\partial\langle V_R\rangle/\partial R$ is typically attributed to non-axisymmetries in the disc (i.e., the bar and/or spiral arms, Siebert et al. 2011a, 2012).

- If we split each age group into bins of metallicity, we show, for the first time, the dependence of this gradient as a function of metallicity. We find that $\partial\langle V_R\rangle/\partial R$ is the most negative for metal-rich bins, gradually and flattens with decreasing metallicity. While a signature of this trend is found in both the young and old stars, it is much more pronounced for young stars.

- We interpret this behavior in the local velocity field as the result of contributions from both the Hercules and Hyades moving groups, associated with the bar and spiral arms, respectively. These streams have both been found to be metal-rich (Famaey et al. 2008; Ramya et al. 2016), and so as we move to more metal-poor bins, their contribution decreases (especially for the Hercules stream), leading to the decrease in the gradient that we find.

- We also find, in agreement with previous studies, that old ('thick disc') stars are kinematically hotter than young ('thin disc') stars. As expected, our old stars lag the LSR significantly due to asymmetric drift. However, we also find our most metal-rich stars also lag the LSR. When we explore the orbital parameters of these stars, we find that while some have eccentric orbits, the majority have circular orbits. The presence of these stars in the solar neighbourhood, along with their orbital dynamics, points to a scenario where both blurring (epicyclic motions) and radial migration (churning) mechanisms play a role in bringing them to the solar neighbourhood.

Acknowledgements. Funding for this work and for RAVE has been provided by: the Australian Astronomical Observatory; the Leibniz-Institut für Astrophysik Potsdam (AIP); the Australian National University; the Australian Research Council; the European Research Council under the European Union's Seventh Framework Programme (Grant Agreement 240271 and 321067); the French National Research Agency; the German Research Foundation (SPP 1177 and SFB 881); the Istituto Nazionale di Astrofisica at Padova; The Johns Hopkins University; the National Science Foundation of the USA (AST-0908326); the W. M. Keck foundation; the Macquarie University; the Netherlands Research School for Astronomy; the Natural Sciences and Engineering Research Council of Canada; the Slovenian Research Agency; the Swiss National Science Foundation; the Science & Technology Facilities Council of the UK; Opticon; Strasbourg Observatory; and the Universities of Groningen, Heidelberg and Sydney. The RAVE web site is at https://www.rave-survey.org. This work has made use of data from the European Space Agency (ESA) mission *Gaia* (`https://www.cosmos.esa.int/gaia`), processed by the *Gaia* Data Processing and Analysis Consortium (DPAC, `https://www.cosmos.esa.int/web/gaia/dpac/consortium`). Funding for the DPAC has been provided by national

institutions, in particular the institutions participating in the *Gaia* Multilateral Agreement.

5 Conclusions & Outlook

This thesis has presented a number of studies utilizing primarily RAVE data to investigate the interplay between kinematics, chemistry, and age for stellar populations found in the solar neighbourhood (distance $\lesssim 1$ kpc). These correlations provide insight into many unresolved questions regarding the secular evolution of the Milky Way disc, including the formation of the thick disc, the effect of internal dynamical mechanisms such as radial migration, and the impact of asymmetric perturbations in the disc (such as the bar and spiral arms).

5.1 Conclusions

In paper I, we identified the two distinct chemical disc components (α-low and α-high) using a probabilistic approach, the first study of its kind using RAVE data. We propose that, in future studies, this method can be applied to other data sets where the α-low and -high sequences cannot be clearly distinguished *a priori*. When exploring kinematic trends in each chemical disc component, we found clear differences between the α-low and -high populations. In particular, trends in mean azimuthal velocity as a function of metallicity exhibit markedly distinct behaviors, with stars belonging to the α-low stars having a negative gradient and α-high sequence having a positive gradient. We also consider trends in the mean velocity dispersion as a function of metallicity, and find that α-low stars exhibit cooler kinematics than the α-high sequence. For the α-high component, these trends are consistent with asymmetric drift. This result supports a disc formation scenario where the thick disc gradually became kinematically cooler, with a break in star formation before resuming in the thin disc (e.g. Haywood et al. 2013, 2016). In the α-low component, we find that our most metal-rich stars lag the LSR, and from their metallicities, it is likely they were not born locally. For a metallicity gradient in the disc of -0.06 dex kpc^{-1}, this corresponds to a birth radius for these super metal-rich stars of ~ 3 kpc (Kordopatis et al. 2015a). In this sense, their presence provides constraints on the efficiency of mechanisms to bring them to the solar neighbourhood, namely through epicyclic excursions or through radial migration.

We conclude that it is likely that a combination of both mechanisms is responsible for bringing these stars from the inner Galaxy, although it is difficult to determine which effect dominates.

To ensure that conclusions derived from RAVE data are robust, in paper II we described in detail the selection function of the RAVE survey, and tested the effect of the RAVE selection function on the kinematic and chemical distributions for different stellar populations. Within the relevant stellar parameter space covered by RAVE, we find that RAVE is kinematically and chemically unbiased. The completeness fraction was evaluated as a function of position, magnitude, and colour, and is now available via the RAVE website. The aim of this work was to help facilitate broad applications of RAVE, as well as allow for the possibility to accurately supplement RAVE data products with those from other large-scale spectroscopic surveys.

Turning back to science questions, in paper III we explored the local velocity field with a sample of RAVE-TGAS stars, as a function of both metallicity and age. While the presence of a radial velocity gradient as a function of Galactocentric radius had been previously identified in the solar neighbourhood using RAVE data (Siebert et al. 2011a; Williams et al. 2013), in this work we show for the first time the dependence of this gradient as a function of metallicity and age. We find that young, metal-rich stars have the steepest gradient, which becomes more shallow for successively metal-poor populations. This gradient has been established as an indicator of non-axisymmetries in the disc: the bar and spiral arms. Coming from the inner Galaxy, our young, metal-rich population is more affected by contributions from both the bar and spiral arms, while more metal-poor populations see less of a contribution from the bar. Understanding these features of the local velocity field is conducive to better constraining Galactic models, and in particular parameters relating to the bar and spiral arms.

5.2 Outlook and perspectives

Gaia has already undoubtedly brought about a new era to the field of Galactic archaeology, and will continue to do so through its final data release, projected for 2022. The next data release of Gaia, DR2, will be available in April 2018, and will provide astrometry and photometry for approximately 1.1 billion stars down to $G \sim 20.7$, and radial velocity measurements for a few million stars brighter than $G \sim 12$. These astrometric measurements will have systematic uncertainties less than 0.1 mas, with typical parallax precision of 0.03 mas for bright ($G \lesssim 15$) stars. While this data will sharpen our view of dynamical structures in the solar neighbourhood and beyond with incredible precision (transverse velocity uncertainties of the order of $\sim 100\ \mathrm{m\,s^{-1}}$ for nearby, bright stars), high-resolution follow-up will be necessary to obtain full stellar parameters and detailed abundance patterns.

There are a number of completed or ongoing surveys that overlap with Gaia, such as RAVE (Steinmetz et al. 2006), APOGEE (Majewski et al. 2015), GALAH (De Silva et al. 2015), Gaia-ESO (Gilmore et al. 2012), and LAMOST (Zhao et al. 2012). Of these, RAVE DR5 (Kunder et al. 2017) currently has the largest overlap of stars in Gaia-TGAS, providing radial velocities, stellar parameters, and chemical

abundances from medium-resolution spectra for a sample of ~ 215 000 stars with exquisite parallaxes and proper motions from Gaia-TGAS. Soon after the second Gaia data release, the final data release of RAVE (DR6) will be made available, with improved pipelines providing updated chemistry and kinematics. Moving to ongoing surveys, LAMOST has obtained low-resolution ($R \sim 2000$) for nearly 4 million stars, with over 1 million of those having spectra with SNR $\gtrsim 100$. These stars probe primarily the outer disc and halo, and aim to provide mean [α/Fe] measurements with uncertainties of the order of ~ 0.08 dex.

While low-resolution surveys currently dominate in terms of sheer numbers, high-resolution surveys offer the advantage of mapping out the chemistry of the solar neighbourhood with finer detail. Using the intermediate- and high-resolution ($R \sim 20\,000 - 47\,000$) FLAMES (GIRAFFE + UVES) spectrographs on the Very Large Telescope (VLT), the Gaia-ESO survey explores the full chemodynamical phase space of ~ 100 000 stars across the Milky Way disc, bulge, and halo, with a focus on star forming regions (Gilmore et al. 2012). Gaia-ESO is able to provide individual abundances for up to 12 elements, down to $V \sim 15$ and radial velocities with uncertainties of $0.1 - 5$ km s^{-1}, and has already contributed to a number of illuminating studies of trends in chemical space in the solar neighbourhood (e.g. Recio-Blanco et al. 2014; Kordopatis et al. 2015b). APOGEE, operating as part of SDSS, provides high-resolution ($R \sim 22\,500$) infrared spectra for primarily red giants in the disc, delivering precise radial velocities with uncertainties of ~ 100 m s^{-1} (Nidever et al. 2015), detailed stellar parameters, and individual abundances (uncertainties ~ 0.1 dex) for up to 15 elements. With a sample size now of ~ 150 000 stars, studies utilizing APOGEE data have demonstrated its power to probe chemodynamical structures to large distances in the Galactic disc, bulge, and halo (e.g. Anders et al. 2014; Hayden et al. 2014; Nidever et al. 2014; Martell et al. 2016). Finally, with a goal of observing ~ 1 million bright disc stars to ($V < 14$), GALAH aims to obtain high-resolution ($R \sim 28\,000$) spectra using the HERMES spectrograph on the Anglo-Australian Telescope (AAT). Deriving stellar parameters, individual abundances for up to ~ 30 elements with ~ 0.04 dex uncertainties and radial velocities with uncertainties of ~ 100 m s^{-1}, GALAH offers an ideal sample of stars for chemical tagging (Freeman & Bland-Hawthorn 2002) studies, where stars which formed in similar environments at the same epoch can be identified by their similar patterns in multidimensional chemical abundance space(e.g. De Silva et al. 2015; Martell et al. 2017).

Two ground-based large-scale spectroscopic facilities, WEAVE (Dalton et al. 2012) and 4MOST (de Jong 2011), are currently planned, and are projected to begin operations within the 5 years. WEAVE's Galactic Archaeology survey aims to provide radial velocities and elemental abundances for stars too faint for accurate measurements with Gaia spectra, $V \gtrsim 15.5$ and $V \gtrsim 12$, respectively. Located in the Northern hemisphere, WEAVE will survey the Galactic anticentre, targeting the outer disc and halo. The low-resolution mode has two general science goals: to constrain fundamental parameters of the disc and its non-axisymmetries, and to map out substructure in the outer disc and halo, with giants out to ~ 100 kpc and main sequence stars to ~ 30 kpc from the Galactic centre. The high-resolution mode of WEAVE will provide detailed chemical abundances for over a million stars in the

volume where distances and ages from Gaia will be the most accurate, down to $V \sim 16$ (line-of-sight distances to ~ 2 kpc), with a primary science goal of disentangling the assembly history of the Milky Way disc and halo. WEAVE is projected to begin operations on the William Herschel Telescope in 2018, although it will be some time before this data is made publicly available.

In the Southern hemisphere, 4MOST will provide a complementary view of the Galaxy, using the VISTA telescope to observe in the direction of the Galactic centre. With a similar spectral resolution and science goals as WEAVE, 4MOST will obtain ~ 20 million low-resolution and ~ 4 million high-resolution spectra in the disc, bulge, and halo. The low-resolution survey, with a broad focus on the formation and history of chemodynamical substructures in the disc and bulge, will provide radial velocities with typical uncertainties of ~ 2 km s^{-1} and abundance uncertainties of ~ 0.2 dex. The high-resolution survey will aim to deliver individual abundances for ~ 15 elements with uncertainties of ~ 0.03 dex. Currently, 4MOST is scheduled to begin operations in 2022. Both 4MOST and WEAVE coverage will augment and expand on the volume probed by Gaia, providing full 6D kinematics and detailed chemical abundance patterns for stellar populations beyond the solar neighbourhood. The synergy between Gaia, WEAVE, and 4MOST will produce robust data sets capable of addressing a number of critical science questions in Galactic archaeology for the Milky Way disc and beyond– including the nature of the interface between the disc and bulge, the formation of the thick disc and its connection to the thin disc, and the merger history of the Milky Way.

With both ongoing and planned large-scale spectroscopic surveys, the Milky Way offers the unique opportunity for detailed studies of its assembly history, to a degree which is currently not possible for any other galaxy. However, the Milky Way is only one galaxy among trillions (e.g. Conselice et al. 2016). To what extent is our understanding of the history of the Milky Way comparable to that of external galaxies? Are models of the formation and evolution of the Milky Way generally applicable to other galaxies? To help address these questions, significant efforts are currently being made to expand the field of galactic archaeology to other nearby spiral galaxies, and in particular our nearest neighbor, M31. Photometric and spectroscopic surveys such as PAndAS (McConnachie et al. 2009), PHAT (Dalcanton et al. 2012), and SPLASH (Gilbert et al. 2006) offer external, but complementary, perspectives on galaxy formation and evolution. Such studies of M31 allow for a more comprehensive view of the galaxy as a whole, including the entire disc and halo structure. Although this external perspective is accompanied by the drawback of lower resolution spectra and less detailed kinematic information, recent studies (e.g. Vargas et al. 2014) have shown it is possible to derive individual abundances for the brightest stars in the halo of M31. My future work will focus on expanding these samples in an effort to identify α-low and -high sequences in both the halo and the disc of M31, which can then be compared to the chemical abundance patterns in the Milky Way and its satellites, bridging the gap between these two distinct approaches to reconstructing the assembly history of massive, late-type galaxies.

While many crucial questions regarding the formation and evolution of galaxies remain far from solved, the rate of growth of Galactic archaeology within the past decade is incredibly encouraging for future prospects. Advances are being

made in almost every conceivable aspect of the field, from instrumentation to target selection, data analysis techniques, and comparisons with cosmological simulations. With these improvements to not just the quantity, but also quality of available multidimensional data, the field of Galactic archaeology is set to continue to revolutionize our understanding of the history of our Galaxy and its place in the universe as a whole.

Bibliography

Abadi, M. G., Navarro, J. F., Steinmetz, M., & Eke, V. R. 2003, ApJ, 591, 499
Adibekyan, V. Z., Figueira, P., Santos, N. C., et al. 2013, A&A, 554, A44
Allende Prieto, C., Beers, T. C., Wilhelm, R., et al. 2006, ApJ, 636, 804
Allende Prieto, C., Fernández-Alvar, E., Schlesinger, K. J., et al. 2014, A&A, 568, A7
Allende Prieto, C., Kawata, D., & Cropper, M. 2016, A&A, 596, A98
Anders, F., Chiappini, C., Minchev, I., et al. 2017, A&A, 600, A70
Anders, F., Chiappini, C., Santiago, B. X., et al. 2014, A&A, 564, A115
Antoja, T., Figueras, F., Romero-Gómez, M., et al. 2011, MNRAS, 418, 1423
Antoja, T., Helmi, A., Dehnen, W., et al. 2014, A&A, 563, A60
Antoja, T., Kordopatis, G., Helmi, A., et al. 2017, A&A, 601, A59
Antoja, T., Monari, G., Helmi, A., et al. 2015, ApJ, 800, L32
Arnett, D. 1996, Supernovae and nucleosynthesis. an investigation of the history of matter, from the Big Bang to the present
Athanassoula, E. 2005, MNRAS, 358, 1477
Athanassoula, E. 2008, ArXiv e-prints
Aumer, M., Binney, J., & Schönrich, R. 2016, MNRAS
Aumer, M. & Binney, J. J. 2009, MNRAS, 397, 1286
Bahcall, J. N., Pinsonneault, M. H., & Wasserburg, G. J. 1995, Reviews of Modern Physics, 67, 781
Bailer-Jones, C. A. L., Andrae, R., Arcay, B., et al. 2013, A&A, 559, A74
Barnes, J. E. 1992, ApJ, 393, 484
Beaulieu, S. F., Freeman, K. C., Kalnajs, A. J., Saha, P., & Zhao, H. 2000, AJ, 120, 855
Beers, T. C., Carollo, D., Ivezić, Ž., et al. 2012, ApJ, 746, 34
Bell, E. F., Zucker, D. B., Belokurov, V., et al. 2008, ApJ, 680, 295
Belokurov, V., Zucker, D. B., Evans, N. W., et al. 2006, ApJ, 642, L137
Bensby, T., Alves-Brito, A., Oey, M. S., Yong, D., & Meléndez, J. 2011, ApJ, 735, L46
Bensby, T., Feltzing, S., Gould, A., et al. 2017, ArXiv e-prints
Bensby, T., Feltzing, S., & Lundström, I. 2003, A&A, 410, 527
Bensby, T., Feltzing, S., Lundström, I., & Ilyin, I. 2005, A&A, 433, 185
Bensby, T., Feltzing, S., & Oey, M. S. 2014, A&A, 562, A71
Bensby, T., Zenn, A. R., Oey, M. S., & Feltzing, S. 2007, ApJ, 663, L13
Bergemann, M., Ruchti, G. R., Serenelli, A., et al. 2014, A&A, 565, A89
Bertelli, G., Girardi, L., Marigo, P., & Nasi, E. 2008, A&A, 484, 815
Bessell, M. S., Collet, R., Keller, S. C., et al. 2015, ApJ, 806, L16
Bienaymé, O., Famaey, B., Siebert, A., et al. 2014, A&A, 571, A92
Binney, J. 2004, in IAU Symposium, Vol. 220, Dark Matter in Galaxies, ed. S. Ryder, D. Pisano, M. Walker, & K. Freeman, 3
Binney, J. 2011, Pramana, 77, 39
Binney, J. 2013, New Astron. Rev., 57, 29
Binney, J., Burnett, B., Kordopatis, G., et al. 2014a, MNRAS, 437, 351
Binney, J., Burnett, B., Kordopatis, G., et al. 2014b, MNRAS, 439, 1231
Binney, J. & Piffl, T. 2015, MNRAS, 454, 3653
Binney, J. & Tremaine, S. 2008, Galactic Dynamics: Second Edition (Princeton University Press)

Bird, J. C., Kazantzidis, S., Weinberg, D. H., et al. 2013, ApJ, 773, 43
Bissantz, N., Englmaier, P., & Gerhard, O. 2003, MNRAS, 340, 949
Bland-Hawthorn, J. & Gerhard, O. 2016, ArXiv e-prints
Blanton, M. R., Bershady, M. A., Abolfathi, B., et al. 2017, AJ, 154, 28
Boeche, C., Siebert, A., Piffl, T., et al. 2013, A&A, 559, A59
Boeche, C., Siebert, A., Williams, M., et al. 2011, AJ, 142, 193
Bonanno, A., Schlattl, H., & Paternò, L. 2002, A&A, 390, 1115
Boss, L. J. 1908, AJ, 26, 31
Bournaud, F., Elmegreen, B. G., & Elmegreen, D. M. 2007, ApJ, 670, 237
Bournaud, F., Elmegreen, B. G., & Martig, M. 2009, ApJ, 707, L1
Bovy, J. 2015, ApJS, 216, 29
Bovy, J. 2017, MNRAS, 468, L63
Bovy, J., Allende Prieto, C., Beers, T. C., et al. 2012a, ApJ, 759, 131
Bovy, J., Bird, J. C., García Pérez, A. E., et al. 2015, ApJ, 800, 83
Bovy, J. & Rix, H.-W. 2013, ApJ, 779, 115
Bovy, J., Rix, H.-W., & Hogg, D. W. 2012b, ApJ, 751, 131
Bovy, J., Rix, H.-W., Liu, C., et al. 2012c, ApJ, 753, 148
Breddels, M. A., Smith, M. C., Helmi, A., et al. 2010, A&A, 511, A90
Bressan, A., Marigo, P., Girardi, L., et al. 2012, MNRAS, 427, 127
Brook, C., Richard, S., Kawata, D., Martel, H., & Gibson, B. K. 2007, ApJ, 658, 60
Brook, C. B., Gibson, B. K., Martel, H., & Kawata, D. 2005, ApJ, 630, 298
Brook, C. B., Kawata, D., Gibson, B. K., & Freeman, K. C. 2004, ApJ, 612, 894
Brook, C. B., Stinson, G., Gibson, B. K., Wadsley, J., & Quinn, T. 2012, MNRAS, 424, 1275
Bullock, J. S. & Boylan-Kolchin, M. 2017, ArXiv e-prints
Bullock, J. S. & Johnston, K. V. 2005, ApJ, 635, 931
Burnett, B. & Binney, J. 2010, MNRAS, 407, 339
Carlin, J. L., DeLaunay, J., Newberg, H. J., et al. 2013, ApJ, 777, L5
Carney, B. W., Laird, J. B., Latham, D. W., & Aguilar, L. A. 1996, AJ, 112, 668
Carney, B. W., Latham, D. W., & Laird, J. B. 1989, AJ, 97, 423
Carollo, D., Beers, T. C., Chiba, M., et al. 2010, ApJ, 712, 692
Carollo, D., Beers, T. C., Lee, Y. S., et al. 2007, Nature, 450, 1020
Carretta, E., Gratton, R. G., & Sneden, C. 2000, A&A, 356, 238
Cartledge, S. I. B., Lauroesch, J. T., Meyer, D. M., & Sofia, U. J. 2006, ApJ, 641, 327
Casagrande, L., Schönrich, R., Asplund, M., et al. 2011, A&A, 530, A138
Chaplin, W. J. & Miglio, A. 2013, ARA&A, 51, 353
Chen, B., Stoughton, C., Smith, J. A., et al. 2001, ApJ, 553, 184
Chen, Y. Q., Nissen, P. E., Zhao, G., Zhang, H. W., & Benoni, T. 2000, A&AS, 141, 491
Chiappini, C., Anders, F., Rodrigues, T. S., et al. 2015, A&A, 576, L12
Chiappini, C., Matteucci, F., & Gratton, R. 1997, ApJ, 477, 765
Chiba, M. & Beers, T. C. 2000, AJ, 119, 2843
Chiosi, C. 1980, A&A, 83, 206
Chou, M.-Y., Majewski, S. R., Cunha, K., et al. 2007, ApJ, 670, 346
Conselice, C. J., Wilkinson, A., Duncan, K., & Mortlock, A. 2016, ApJ, 830, 83
Cutri, R. M., Skrutskie, M. F., van Dyk, S., et al. 2003, VizieR Online Data Catalog, 2246
Dalcanton, J. J., Williams, B. F., Lang, D., et al. 2012, ApJS, 200, 18
Dalton, G., Trager, S. C., Abrams, D. C., et al. 2012, in Proc. SPIE, Vol. 8446, Ground-based and Airborne Instrumentation for Astronomy IV, 84460P
Davies, G. R. & Miglio, A. 2016, Astronomische Nachrichten, 337, 774
de Jong, R. 2011, The Messenger, 145, 14

De Silva, G. M., Freeman, K. C., Bland-Hawthorn, J., et al. 2015, MNRAS, 449, 2604
Dehnen, W. 1998, AJ, 115, 2384
Dehnen, W. 2000, AJ, 119, 800
DENIS Consortium. 2005, VizieR Online Data Catalog, 2263
Di Matteo, P., Lehnert, M. D., Qu, Y., & van Driel, W. 2011, A&A, 525, L3
Drlica-Wagner, A., Bechtol, K., Rykoff, E. S., et al. 2015, ApJ, 813, 109
Dutra, C. M., Santiago, B. X., & Bica, E. 2002, A&A, 381, 219
Dwek, E., Arendt, R. G., Hauser, M. G., et al. 1995, ApJ, 445, 716
Edvardsson, B., Andersen, J., Gustafsson, B., et al. 1993, A&A, 275, 101
Eggen, O. J. 1958, MNRAS, 118, 65
Eggen, O. J., Lynden-Bell, D., & Sandage, A. R. 1962, ApJ, 136, 748
Elmegreen, B. G. & Elmegreen, D. M. 2006, ApJ, 650, 644
Epchtein, N., Deul, E., Derriere, S., et al. 1999, A&A, 349, 236
Famaey, B., Pont, F., Luri, X., et al. 2007, A&A, 461, 957
Famaey, B., Siebert, A., & Jorissen, A. 2008, A&A, 483, 453
Faure, C., Siebert, A., & Famaey, B. 2014, MNRAS, 440, 2564
Feltzing, S. & Chiba, M. 2013, New Astron. Rev., 57, 80
Fisher, D. B. & Drory, N. 2011, ApJ, 733, L47
Flynn, C., Holmberg, J., Portinari, L., Fuchs, B., & Jahreiß, H. 2006, MNRAS, 372, 1149
Forbes, J., Krumholz, M., & Burkert, A. 2012, ApJ, 754, 48
Freeman, K. & Bland-Hawthorn, J. 2002, ARA&A, 40, 487
Frenk, C. S. & White, S. D. M. 2012, Annalen der Physik, 524, 507
Fuhrmann, K. 1998, A&A, 338, 161
Fuhrmann, K. 2004, Astronomische Nachrichten, 325, 3
Fuhrmann, K. 2008, MNRAS, 384, 173
Fuhrmann, K. 2011, MNRAS, 414, 2893
Fuhrmann, K., Chini, R., Kaderhandt, L., & Chen, Z. 2017, MNRAS, 464, 2610
Fux, R. 2001, A&A, 373, 511
Gaia Collaboration, Prusti, T., de Bruijne, J. H. J., et al. 2016, A&A, 595, A1
Gazzano, J.-C., Kordopatis, G., Deleuil, M., et al. 2013, A&A, 550, A125
Geisler, D., Smith, V. V., Wallerstein, G., Gonzalez, G., & Charbonnel, C. 2005, AJ, 129, 1428
Genovali, K., Lemasle, B., Bono, G., et al. 2014, A&A, 566, A37
Gerhard, O. 2002, Space Sci. Rev., 100, 129
Gibson, B. K., Pilkington, K., Brook, C. B., Stinson, G. S., & Bailin, J. 2013, A&A, 554, A47
Gilbert, K. M., Guhathakurta, P., Kalirai, J. S., et al. 2006, ApJ, 652, 1188
Gilmore, G., Randich, S., Asplund, M., et al. 2012, The Messenger, 147, 25
Gilmore, G. & Reid, N. 1983, MNRAS, 202, 1025
Gilmore, G., Wyse, R. F. G., & Jones, J. B. 1995, AJ, 109, 1095
Gilmore, G., Wyse, R. F. G., & Kuijken, K. 1989, ARA&A, 27, 555
Gilmore, G., Wyse, R. F. G., & Norris, J. E. 2002, ApJ, 574, L39
Girardi, L. 2016, ARA&A, 54, 95
Golubov, O., Just, A., Bienaymé, O., et al. 2013, A&A, 557, A92
Gómez, F. A., Minchev, I., O'Shea, B. W., et al. 2013, MNRAS, 429, 159
Gonzalez, O. A., Rejkuba, M., Zoccali, M., et al. 2013, A&A, 552, A110
Górski, K. M., Hivon, E., Banday, A. J., et al. 2005, ApJ, 622, 759
Grenon, M. 1972, in IAU Colloq. 17: Age des Etoiles, ed. G. Cayrel de Strobel & A. M. Delplace, 55
Guiglion, G., Recio-Blanco, A., de Laverny, P., et al. 2015, A&A, 583, A91
Halle, A., Di Matteo, P., Haywood, M., & Combes, F. 2015, A&A, 578, A58

Hambly, N. C., MacGillivray, H. T., Read, M. A., et al. 2001, MNRAS, 326, 1279
Hayden, M. R., Bovy, J., Holtzman, J. A., et al. 2015, ApJ, 808, 132
Hayden, M. R., Holtzman, J. A., Bovy, J., et al. 2014, AJ, 147, 116
Haywood, M. 2008, MNRAS, 388, 1175
Haywood, M., Di Matteo, P., Lehnert, M. D., Katz, D., & Gómez, A. 2013, A&A, 560, A109
Haywood, M., Lehnert, M. D., Di Matteo, P., et al. 2016, ArXiv e-prints
Helmi, A. 2008, A&ARv, 15, 145
Helmi, A., Veljanoski, J., Breddels, M. A., Tian, H., & Sales, L. V. 2017, A&A, 598, A58
Helmi, A. & White, S. D. M. 1999, MNRAS, 307, 495
Høg, E., Fabricius, C., Makarov, V. V., et al. 2000, A&A, 355, L27
Holmberg, J., Nordström, B., & Andersen, J. 2007, A&A, 475, 519
Homma, D., Chiba, M., Okamoto, S., et al. 2016, ApJ, 832, 21
Hopkins, P. F., Quataert, E., & Murray, N. 2012, MNRAS, 421, 3522
Howes, L. M., Casey, A. R., Asplund, M., et al. 2015, Nature, 527, 484
Ibata, R. A., Gilmore, G., & Irwin, M. J. 1994, Nature, 370, 194
Israelian, G. & Meynet, G., eds. 2008, The Metal-Rich Universe (Cambridge University Press), cambridge Books Online
Ivezić, Ž., Beers, T. C., & Jurić, M. 2012, ARA&A, 50, 251
Ivezić, Ž., Sesar, B., Jurić, M., et al. 2008, ApJ, 684, 287
Jofré, P., Heiter, U., Soubiran, C., et al. 2014, A&A, 564, A133
Jørgensen, B. R. & Lindegren, L. 2005, A&A, 436, 127
Jurić, M., Ivezić, Ž., Brooks, A., et al. 2008, ApJ, 673, 864
Just, A. & Jahreiß, H. 2010, MNRAS, 402, 461
Kalirai, J. S. 2012, Nature, 486, 90
Kalnajs, A. J. 1991, in Dynamics of Disc Galaxies, ed. B. Sundelius, 323
Kauffmann, G., White, S. D. M., & Guiderdoni, B. 1993, MNRAS, 264, 201
Keller, S. C., Bessell, M. S., Frebel, A., et al. 2014, Nature, 506, 463
Kennicutt, Jr., R. C. 1998, ApJ, 498, 541
Kent, S. M., Dame, T. M., & Fazio, G. 1991, ApJ, 378, 131
Kilic, M., Munn, J. A., Harris, H. C., et al. 2017, ApJ, 837, 162
Klypin, A., Kravtsov, A. V., Valenzuela, O., & Prada, F. 1999, ApJ, 522, 82
Koch, A., Grebel, E. K., Gilmore, G. F., et al. 2008, AJ, 135, 1580
Koposov, S. E., Belokurov, V., Torrealba, G., & Evans, N. W. 2015, ApJ, 805, 130
Kordopatis, G. 2015, IAU General Assembly, 22, 2252182
Kordopatis, G., Binney, J., Gilmore, G., et al. 2015a, MNRAS, 447, 3526
Kordopatis, G., Gilmore, G., Steinmetz, M., et al. 2013a, AJ, 146, 134
Kordopatis, G., Gilmore, G., Wyse, R. F. G., et al. 2013b, MNRAS, 436, 3231
Kordopatis, G., Recio-Blanco, A., de Laverny, P., et al. 2011, A&A, 535, A107
Kordopatis, G., Wyse, R. F. G., Chiappini, C., et al. 2017, MNRAS, 467, 469
Kordopatis, G., Wyse, R. F. G., Gilmore, G., et al. 2015b, A&A, 582, A122
Kormendy, J., Drory, N., Bender, R., & Cornell, M. E. 2010, ApJ, 723, 54
Kuijken, K. & Tremaine, S. 1994, ApJ, 421, 178
Kunder, A., Koch, A., Rich, R. M., et al. 2012, AJ, 143, 57
Kunder, A., Kordopatis, G., Steinmetz, M., et al. 2017, AJ, 153, 75
Kunder, A., Rich, R. M., Koch, A., et al. 2016, ApJ, 821, L25
Kushniruk, I., Schirmer, T., & Bensby, T. 2017, ArXiv e-prints
Larson, R. B. 1974, MNRAS, 166, 585
Lee, Y. S., Beers, T. C., An, D., et al. 2011, ApJ, 738, 187
Letarte, B. 2007, PhD thesis, University of Groningen

Lewis, I. J., Cannon, R. D., Taylor, K., et al. 2002, MNRAS, 333, 279
Lindegren, L. & Feltzing, S. 2013, A&A, 553, A94
Lindegren, L., Lammers, U., Bastian, U., et al. 2016, A&A, 595, A4
Loebman, S. R., Roškar, R., Debattista, V. P., et al. 2011, ApJ, 737, 8
Lynden-Bell, D. & Lynden-Bell, R. M. 1995, MNRAS, 275, 429
Madau, P. & Dickinson, M. 2014, ARA&A, 52, 415
Majewski, S. R., Schiavon, R. P., Frinchaboy, P. M., et al. 2015, ArXiv e-prints
Martell, S. L., Sharma, S., Buder, S., et al. 2017, MNRAS, 465, 3203
Martell, S. L., Shetrone, M. D., Lucatello, S., et al. 2016, ApJ, 825, 146
Martig, M., Rix, H.-W., Silva Aguirre, V., et al. 2015, MNRAS, 451, 2230
Masseron, T. & Gilmore, G. 2015, MNRAS, 453, 1855
Matijevič, G., Zwitter, T., Bienaymé, O., et al. 2012, ApJS, 200, 14
Matteucci, F., ed. 2001, Astrophysics and Space Science Library, Vol. 253, The chemical evolution of the Galaxy
Matteucci, F. & Francois, P. 1989, MNRAS, 239, 885
McConnachie, A. W., Irwin, M. J., Ibata, R. A., et al. 2009, Nature, 461, 66
McMillan, P. J. 2011, MNRAS, 414, 2446
McMillan, P. J. 2013, MNRAS, 430, 3276
McMillan, P. J. 2017, MNRAS, 465, 76
McMillan, P. J. & Binney, J. J. 2008, MNRAS, 390, 429
McMillan, P. J., Kordopatis, G., Kunder, A., et al. 2017, ArXiv e-prints
McWilliam, A. & Smecker-Hane, T. A. 2005, in Astronomical Society of the Pacific Conference Series, Vol. 336, Cosmic Abundances as Records of Stellar Evolution and Nucleosynthesis, ed. T. G. Barnes, III & F. N. Bash, 221
Meza, A., Navarro, J. F., Abadi, M. G., & Steinmetz, M. 2005, MNRAS, 359, 93
Michalik, D., Lindegren, L., & Hobbs, D. 2015, A&A, 574, A115
Minchev, I., Chiappini, C., & Martig, M. 2013, A&A, 558, A9
Minchev, I., Chiappini, C., & Martig, M. 2014a, A&A, 572, A92
Minchev, I., Chiappini, C., Martig, M., et al. 2014b, ApJ, 781, L20
Minchev, I., Famaey, B., Quillen, A. C., et al. 2012, A&A, 548, A127
Minchev, I. & Quillen, A. C. 2007, MNRAS, 377, 1163
Miranda, M. S., Pilkington, K., Gibson, B. K., et al. 2015, ArXiv e-prints
Monaco, L., Bellazzini, M., Bonifacio, P., et al. 2005, A&A, 441, 141
Monari, G., Famaey, B., Fouvry, J.-B., & Binney, J. 2017a, ArXiv e-prints
Monari, G., Famaey, B., & Siebert, A. 2016, MNRAS, 457, 2569
Monari, G., Helmi, A., Antoja, T., & Steinmetz, M. 2014, A&A, 569, A69
Monari, G., Kawata, D., Hunt, J. A. S., & Famaey, B. 2017b, MNRAS, 466, L113
Munari, U., Henden, A., Frigo, A., et al. 2014, AJ, 148, 81
Nath, B. B. & Silk, J. 2009, MNRAS, 396, L90
Navarro, J. F., Abadi, M. G., Venn, K. A., Freeman, K. C., & Anguiano, B. 2011, MNRAS, 412, 1203
Navarro, J. F., Helmi, A., & Freeman, K. C. 2004, ApJ, 601, L43
Ness, M., Freeman, K., Athanassoula, E., et al. 2013, MNRAS, 432, 2092
Nidever, D. L., Bovy, J., Bird, J. C., et al. 2014, ApJ, 796, 38
Nidever, D. L., Holtzman, J. A., Allende Prieto, C., et al. 2015, AJ, 150, 173
Nissen, P. E., Gustafsson, B., Edvardsson, B., & Gilmore, G. 1994, A&A, 285, 440
Nissen, P. E. & Schuster, W. J. 2010, A&A, 511, L10
Noguchi, M. 1998, Nature, 392, 253
Nomoto, K., Iwamoto, K., Nakasato, N., et al. 1997, Nuclear Physics A, 621, 467
Nomoto, K., Kobayashi, C., & Tominaga, N. 2013, ARA&A, 51, 457

Nordlander, T., Amarsi, A. M., Lind, K., et al. 2017, A&A, 597, A6
Nordström, B., Mayor, M., Andersen, J., et al. 2004, A&A, 418, 989
Obreja, A., Domínguez-Tenreiro, R., Brook, C., et al. 2013, ApJ, 763, 26
Ojha, D. K., Bienayme, O., Robin, A. C., Creze, M., & Mohan, V. 1996, A&A, 311, 456
Olling, R. P. & Dehnen, W. 2003, ApJ, 599, 275
Oort, J. H. 1927a, Bull. Astron. Inst. Netherlands, 4, 79
Oort, J. H. 1927b, Bull. Astron. Inst. Netherlands, 3, 275
Ortolani, S., Renzini, A., Gilmozzi, R., et al. 1995, Nature, 377, 701
Pasetto, S., Grebel, E. K., Zwitter, T., et al. 2012, A&A, 547, A71
Patsis, P. A., Skokos, C., & Athanassoula, E. 2003, MNRAS, 342, 69
Peebles, P. J. E. 2012, ARA&A, 50, 1
Perryman, M. A. C., Lindegren, L., Kovalevsky, J., et al. 1997, A&A, 323, L49
Piffl, T., Scannapieco, C., Binney, J., et al. 2014, A&A, 562, A91
Planck Collaboration, Ade, P. A. R., Aghanim, N., et al. 2016, A&A, 594, A13
Pont, F. & Eyer, L. 2004, MNRAS, 351, 487
Portail, M., Wegg, C., Gerhard, O., & Martinez-Valpuesta, I. 2015, MNRAS, 448, 713
Pouliasis, E., Di Matteo, P., & Haywood, M. 2017, A&A, 598, A66
Prusti, T. 2012, Astronomische Nachrichten, 333, 453
Purcell, C. W., Bullock, J. S., Tollerud, E. J., Rocha, M., & Chakrabarti, S. 2011, Nature, 477, 301
Quillen, A. C., Dougherty, J., Bagley, M. B., Minchev, I., & Comparetta, J. 2011, MNRAS, 417, 762
Quillen, A. C. & Garnett, D. R. 2001, in Astronomical Society of the Pacific Conference Series, Vol. 230, Galaxy Disks and Disk Galaxies, ed. J. G. Funes & E. M. Corsini, 87–88
Quillen, A. C. & Minchev, I. 2005, AJ, 130, 576
Quinn, P. J., Hernquist, L., & Fullagar, D. P. 1993, ApJ, 403, 74
Ramya, P., Reddy, B. E., Lambert, D. L., & Musthafa, M. M. 2016, MNRAS, 460, 1356
Rattenbury, N. J., Mao, S., Sumi, T., & Smith, M. C. 2007, MNRAS, 378, 1064
Recio-Blanco, A., de Laverny, P., Allende Prieto, C., et al. 2016, A&A, 585, A93
Recio-Blanco, A., de Laverny, P., Kordopatis, G., et al. 2014, A&A, 567, A5
Reddy, B. E., Lambert, D. L., & Allende Prieto, C. 2006, MNRAS, 367, 1329
Reddy, B. E., Tomkin, J., Lambert, D. L., & Allende Prieto, C. 2003, MNRAS, 340, 304
Reid, I. N. 2005, ARA&A, 43, 247
Reid, M. J., Menten, K. M., Brunthaler, A., et al. 2014, ApJ, 783, 130
Reylé, C. & Robin, A. C. 2001, A&A, 373, 886
Rich, R. M. 1988, AJ, 95, 828
Richter, P. 2006, in Reviews in Modern Astronomy, ed. S. Roeser, Vol. 19, 31
Richter, P., Sembach, K. R., Wakker, B. P., et al. 2001, ApJ, 559, 318
Rix, H.-W. & Bovy, J. 2013, A&ARv, 21, 61
Robin, A. C., Reylé, C., Derrière, S., & Picaud, S. 2003, A&A, 409, 523
Roeser, S., Demleitner, M., & Schilbach, E. 2010, AJ, 139, 2440
Rojas-Arriagada, A., Recio-Blanco, A., de Laverny, P., et al. 2016, A&A, 586, A39
Roškar, R., Debattista, V. P., Quinn, T. R., Stinson, G. S., & Wadsley, J. 2008, ApJ, 684, L79
Ryan, S. G. & Norris, J. E. 1991, AJ, 101, 1865
Sanders, J. L. & Binney, J. 2015, MNRAS, 449, 3479
Sbordone, L., Bonifacio, P., Buonanno, R., et al. 2007, A&A, 465, 815
Scannapieco, C., Wadepuhl, M., Parry, O. H., et al. 2012, MNRAS, 423, 1726
Scannapieco, C., White, S. D. M., Springel, V., & Tissera, P. B. 2009, MNRAS, 396, 696
Schlesinger, K. J., Johnson, J. A., Rockosi, C. M., et al. 2014, ApJ, 791, 112

Schönrich, R. 2012, MNRAS, 427, 274
Schönrich, R., Asplund, M., & Casagrande, L. 2011, MNRAS, 415, 3807
Schönrich, R. & Binney, J. 2009a, MNRAS, 396, 203
Schönrich, R. & Binney, J. 2009b, MNRAS, 399, 1145
Schönrich, R., Binney, J., & Dehnen, W. 2010, MNRAS, 403, 1829
Schönrich, R. & McMillan, P. J. 2017, MNRAS, 467, 1154
Schörck, T., Christlieb, N., Cohen, J. G., et al. 2009, A&A, 507, 817
Searle, L. & Zinn, R. 1978, ApJ, 225, 357
Sellwood, J. A. & Binney, J. J. 2002, MNRAS, 336, 785
Sharma, S., Bland-Hawthorn, J., Binney, J., et al. 2014, ApJ, 793, 51
Sharma, S., Bland-Hawthorn, J., Johnston, K. V., & Binney, J. 2011, ApJ, 730, 3
Shen, J., Rich, R. M., Kormendy, J., et al. 2010, ApJ, 720, L72
Shetrone, M., Venn, K. A., Tolstoy, E., et al. 2003, AJ, 125, 684
Siebert, A., Bienaymé, O., Binney, J., et al. 2008, MNRAS, 391, 793
Siebert, A., Famaey, B., Binney, J., et al. 2012, MNRAS, 425, 2335
Siebert, A., Famaey, B., Minchev, I., et al. 2011a, MNRAS, 412, 2026
Siebert, A., Williams, M. E. K., Siviero, A., et al. 2011b, AJ, 141, 187
Skrutskie, M. F., Cutri, R. M., Stiening, R., et al. 2006, AJ, 131, 1163
Smecker-Hane, T. A. & Wyse, R. F. G. 1992, AJ, 103, 1621
Snaith, O., Haywood, M., Di Matteo, P., et al. 2015, A&A, 578, A87
Snaith, O. N., Haywood, M., Di Matteo, P., et al. 2014, ApJ, 781, L31
Soderblom, D. R. 2010, ARA&A, 48, 581
Sormani, M. C., Binney, J., & Magorrian, J. 2015, MNRAS, 454, 1818
Soubiran, C., Bienaymé, O., & Siebert, A. 2003, A&A, 398, 141
Springel, V., Frenk, C. S., & White, S. D. M. 2006, Nature, 440, 1137
Stanek, K. Z., Mateo, M., Udalski, A., et al. 1994, ApJ, 429, L73
Stanek, K. Z., Udalski, A., SzymaŃski, M., et al. 1997, ApJ, 477, 163
Steinmetz, M., Zwitter, T., Siebert, A., et al. 2006, AJ, 132, 1645
Stonkutė, E., Koposov, S. E., Howes, L. M., et al. 2016, MNRAS, 460, 1131
Tolstoy, E., Hill, V., & Tosi, M. 2009, ARA&A, 47, 371
Tonry, J. & Davis, M. 1979, AJ, 84, 1511
Trick, W. H., Bovy, J., & Rix, H.-W. 2016, ApJ, 830, 97
Žerjal, M., Zwitter, T., Matijevič, G., et al. 2013, ApJ, 776, 127
Valenti, E., Zoccali, M., Gonzalez, O. A., et al. 2016, A&A, 587, L6
Vargas, L. C., Gilbert, K. M., Geha, M., et al. 2014, ApJ, 797, L2
Veltz, L., Bienaymé, O., Freeman, K. C., et al. 2008, A&A, 480, 753
Venn, K. A., Irwin, M., Shetrone, M. D., et al. 2004, AJ, 128, 1177
Vickers, J. J., Roeser, S., & Grebel, E. K. 2016, ArXiv e-prints
Villalobos, Á. & Helmi, A. 2008, MNRAS, 391, 1806
Wakker, B. P. 2001, ApJS, 136, 463
Walker, I. R., Mihos, J. C., & Hernquist, L. 1996, ApJ, 460, 121
Wegg, C., Gerhard, O., & Portail, M. 2015, MNRAS, 450, 4050
Weiland, J. L., Arendt, R. G., Berriman, G. B., et al. 1994, ApJ, 425, L81
Wheeler, J. C., Sneden, C., & Truran, Jr., J. W. 1989, ARA&A, 27, 279
Widrow, L. M., Gardner, S., Yanny, B., Dodelson, S., & Chen, H.-Y. 2012, ApJ, 750, L41
Wielen, R. 1977, A&A, 60, 263
Williams, M. E. K., Steinmetz, M., Binney, J., et al. 2013, MNRAS, 436, 101
Wojno, J., Kordopatis, G., Piffl, T., et al. 2017, MNRAS, 468, 3368
Wojno, J., Kordopatis, G., Steinmetz, M., et al. 2016, ArXiv e-prints

Wright, E. L., Eisenhardt, P. R. M., Mainzer, A. K., et al. 2010, AJ, 140, 1868
Wyse, R. F. G. 2016, in Astronomical Society of the Pacific Conference Series, Vol. 507, Multi-Object Spectroscopy in the Next Decade: Big Questions, Large Surveys, and Wide Fields, ed. I. Skillen, M. Barcells, & S. Trager, 13
Yanny, B., Rockosi, C., Newberg, H. J., et al. 2009, AJ, 137, 4377
Zacharias, N., Finch, C., & Frouard, J. 2017, AJ, 153, 166
Zacharias, N., Finch, C. T., Girard, T. M., et al. 2013, AJ, 145, 44
Zhao, G., Zhao, Y.-H., Chu, Y.-Q., Jing, Y.-P., & Deng, L.-C. 2012, Research in Astronomy and Astrophysics, 12, 723
Zhao, H. 1996, MNRAS, 283, 149
Zhao, H., Spergel, D. N., & Rich, R. M. 1994, AJ, 108, 2154
Zoccali, M., Gonzalez, O. A., Vasquez, S., et al. 2014, A&A, 562, A66
Zoccali, M., Hill, V., Lecureur, A., et al. 2008, A&A, 486, 177
Zoccali, M., Renzini, A., Ortolani, S., et al. 2003, A&A, 399, 931
Zuckerman, B., Song, I., & Bessell, M. S. 2004, ApJ, 613, L65
Zwitter, T., Matijevič, G., Breddels, M. A., et al. 2010, A&A, 522, A54
Zwitter, T., Siebert, A., Munari, U., et al. 2008, AJ, 136, 421

Publications

Refereed publications

1. *Identification of Globular Cluster Stars in RAVE data II: Extended tidal debris around NGC 3201*
   Anguiano B., De Silva G. M., Freeman K., Da Costa G. S., Zwitter T., Quillen A. C., Zucker D. B., Navarro J. F., Kunder A., Siebert A., Wyse R. F. G., Grebel E. K., Kordopatis G., Gibson B. K., Seabroke G., Sharma S., **Wojno J.**, Bland-Hawthorn J., Parker Q. A., Steinmetz M., Boeche C., Gilmore G., Bienaymé O., Reid W., Watson F.
   MNRAS (2016), 457, 2078

2. *Chemical separation of disc components using RAVE*
   Wojno J., Kordopatis G., Steinmetz M., McMillan P., Matijevič G., Binney J., Wyse R. F. G., Boeche C., Just A., Grebel E. K., Siebert A., Bienaymé O., Gibson B. K., Zwitter T., Bland-Hawthorn J., Navarro J. F., Parker Q. A., Reid W., Seabroke G., Watson F.
   MNRAS (2016), 461, 4246

3. *The Radial Velocity Experiment (RAVE): Fifth Data Release*
   Kunder A., Kordopatis G., Steinmetz M., Zwitter T., McMillan P., Casagrande L., Enke H., **Wojno J.**, Valentini M., Chiappini C., Matijevic G., Siviero A., de Laverny P., Recio-Blanco A., Bijaoui A., Wyse R. F. G., Binney J., Grebel E. K., Helmi A., Jofre P., Antoja T., Gilmore G., Siebert A., Famaey B., Bienayme O., Gibson B. K., Freeman K. C., Navarro J. F., Munari U., Seabroke G., Anguiano B., Zerjal M., Minchev I., Reid W., Bland-Hawthorn J., Kos J., Sharma S., Watson F., Parker Q. A., Scholz R.-D., Burton D., Cass P., Hartley M., Fiegert K., Stupar M., Ritter A., Hawkins K., Gerhard O., Chaplin W. J., Davies G. R., Elsworth Y. P., Lund M. N., Miglio A., Mosser B.
   AJ, (2017), 153, 75

4. *Chromospherically active stars in the RAVE survey. II. Young dwarfs in the solar neighborhood*
   Zerjal M., Zwitter T., Matijevic G., Grebel E., Kordopatis G., Munari U., Seabroke G., Steinmetz M., **Wojno J.**, Bienaymé O., Bland-Hawthorn J., Conrad C., Freeman K. C., Gibson B. K., Gilmore G., Kunder A., Navarro J., Parker Q. A., Reid W., Siviero A., Watson F. G., Wyse R. F. G.
   ApJ (2017), 835, 61

5. *The selection function of the RAVE survey*
   Wojno J., Kordopatis G., Piffl T., Binney J., Steinmetz M., Matijevič G., Bland-Hawthorn J., Sharma S., McMillan P., Watson F., Reid W., Kunder A., Enke H.,

Grebel E. K., Seabroke G., Wyse R. F. G., Zwitter T., Bienaymé O., Freeman K. C., Gibson B. K., Gilmore G., Helmi A., Munari U., Navarro J. F., Parker Q. A., Siebert A.
MNRAS (2017), 468, 3368

6. *Spectroscopic confirmation of the low-latitude object FSR 1716 as an old globular cluster*
Koch A., Kunder A., **Wojno J.**
A&A (2017), 605, A128

Submitted articles and articles in preparation

7. *Improved distances to stars common to TGAS and RAVE*
McMillan P. J., Kordopatis G., Kunder A., Binney J., **Wojno, J.**, Zwitter T., Steinmetz M., Bland-Hawthorn J., Gibson B. K., Gilmore G., Grebel E. K., Helmi A., Munari U., Navarro J. F.; Parker Q. A., Seabroke, G., Wyse, R. F. G.
(2017), arXiv:1707.04554, submitted

8. *Correlations between age, kinematics, and chemistry as seen by the RAVE survey*
Wojno J., Kordopatis G., McMillan P. J., Famaey B., Steinmetz M., and the RAVE collaboration
(2017), in preparation

Conference Proceedings

9. *Age-metallicity-velocity relation of stars as seen by RAVE*
Wojno J., Kordopatis G., Steinmetz M., Matijevič G., McMillan P. J.
The General Assembly of Galaxy Halos: Structure, Origin and Evolution (2016), 317, 367

10. *The age-metallicity relation with RAVE and TGAS*
Wojno J., Kordopatis G., Steinmetz M., McMillan P. J., and the RAVE collaboration
Astrometry and Astrophysics in the Gaia sky (2017), 330

11. *Kinematic trends in young and old stars*
Wojno J., Kordopatis G., Steinmetz M., McMillan P. J., and the RAVE collaboration
Rediscovering our Galaxy (2017), 334

Acknowledgements

First and foremost, I'd like to thank my supervisor, Georges Kordopatis, for his guidance over the past three years. Without his advice, persistence, and extensive knowledge, this thesis would not have been possible.

I would also like to extend my deepest thanks to Matthias Steinmetz, for not only providing me the opportunity to work and study at AIP, but also for the many words of encouragement and helpful suggestions over the course of my time here.

I'd also like to express my gratitude to the other members of the thesis committee: Lutz Wisotzki, Philipp Richter, and a special thanks to my external referees Rosemary Wyse and Sofia Feltzing.

To all of the postdocs and faculty at AIP that I had the pleasure of interacting with: Gal, Else, Maria-Rosa, Ivan, Cristina, Marica, Roelof, Petra, Noam, your support and assistance made a world of difference over the course of my PhD. I'd like to particularly thank Andrea Kunder for allowing me the opportunity to gain valuable experience conducting observations at AAO.

To my fellow PhD students: Josie, Omar, Sabine, Friedrich, Anke, thanks for all the chats over coffee, tea, and kuchen. My time here at AIP was made so much brighter by your companionship. Kris– thanks for being there with me through the tongue piercing, concerts, mosh pits, parties, after-parties, and the broken nose. It's been a wild ride. Georges, if you're reading this part, that was all just a joke. Absolutely no fun was had after my first year.

A special shout out to the Gleis 6 gang: Omar, Hauke, Sam, and Trey. Thanks for all the beers, burgers, bad German, and good times!

I'd like to thank Alexey Mints, Saskia Hekker, and the rest of the SAGE group for an interesting and productive visit to MPS in Göttingen.

I would also like to thank Paul McMillan, Louise Howes, and everyone I interacted with at the Lund Observatory for their hospitality during my visit there. In addition to the insightful conversations over many coffee breaks, I greatly appreciated the opportunity to present and discuss my work with your group.

I am deeply indebted to all of my co-authors and other members of the RAVE collaboration. Your comments and suggestions were invaluable, and served to greatly improve the manuscripts that comprise the majority of this thesis.

I'm especially grateful for the tremendous and unwavering support from my family and friends back in the US– thanks Mom, Dad, Grandma, Grandpa, Mama, Julie, Elle, Brielle, and Hayner.

Finally, Zach, thank you for your limitless patience throughout these past five years. Whether the distance between us was 1000 km or 8000 km, you always found a way to love and support me. You're the best friend and partner anyone could hope for.

We have calcium in our bones,
iron in our veins,
carbon in our souls,
and nitrogen in our brains.
93 percent stardust,
with souls made of flames,
we are all just stars
that have people names.

Nikita Gill, “93 Percent Stardust”